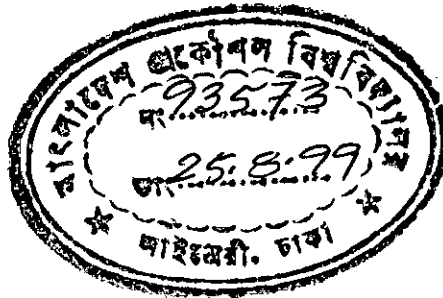


# FLOW IN A SWIRL COMBUSTOR

By  
Syed Mohammed Shiblee Noman

A Thesis

Submitted to the Department of Mechanical Engineering in partial fulfillment of the requirements for the degree of Master of Science in Mechanical Engineering



Bangladesh University of Engineering & Technology,  
Dhaka-1000  
Bangladesh

August, 1999



#93573#

## RECOMMENDATION OF THE BOARD OF EXAMINARS

This Board of Examiners hereby recommends to the Department of Mechanical Engineering, BUET, Dhaka, acceptance of the thesis. "**FLOW IN A SWIRL COMBUSTOR**", submitted by Syed Mohammed Shiblee Noman (Roll No. 9510053P) in partial fulfillment of the requirements for the degree of Master of Science in Mechanical Engineering.

Chairman (Supervisor)



---

Dr. Showkat Jahan Chowdhury  
Professor  
Department of Mechanical Engineering  
BUET, Dhaka

Member (Ex-officio)



---

Dr. Md. Abdur Razzaq Akhanda  
Professor and Head  
Department of Mechanical Engineering  
BUET, Dhaka

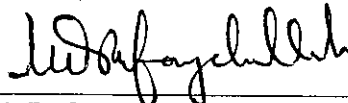
Member



---

Dr. Md. Quamrul Islam  
Professor  
Department of Mechanical Engineering  
BUET, Dhaka

Member (External)



---

Dr. Md. Refayet Ullah  
Professor  
Department of Naval Architecture and Marine  
Engineering  
BUET, Dhaka

12<sup>th</sup> August, 1999

## DECLARATION OF THE CANDIDATE

It is hereby declared that neither this thesis nor any part thereof has been submitted or is being concurrently submitted anywhere for the award of any degree or diploma.

---

Candidate

## CERTIFICATE OF RESEARCH

This is to certify that the work presented in this thesis is the outcome of the investigations carried out by the candidate under the supervision of Dr. Showkat Jahan Chowdhury, Professor, Department of Mechanical Engineering, Bangladesh University of Engineering and Technology, Dhaka, Bangladesh.

---

Supervisor

---

Candidate

## ABSTRACT

This thesis presents the numerical study of fluid properties for confined swirling turbulent flow in a swirl combustor. Different types of swirlers are considered for the gas combustor with cooling airflow around the swirling annular flow. Such a complex flow possesses several distinctly different flow regimes, either one or two recirculation regions of extremely high level of turbulence. Due to the expansion geometry, substantially higher mixing rates are produced. The elevated mixing rates are due to very high level of turbulence kinetic energy generated by shearing as the core flow experiences sudden expansion. Adding swirl to the flow field having expansion causes further increase in turbulence kinetic energy and consequently speeds up the mixing process in the combustion chamber. The type of rotational motion, solid body or free-vortex type also has different effects on the stresses and turbulence energy. Hence detail knowledge of the properties are required before manufacturing the equipment encountering these types of flows. As experimental investigations are quite expensive, therefore the problem is numerically investigated with different flow parameters.

The governing differential equations using the  $k-\epsilon$  turbulence model closure are solved by a control-volume based iterative finite difference technique. A non-uniform staggered grid is used. The discretized equations with boundary condition modifications are solved utilizing the SIMPLE algorithm with TDMA. Computations are done for the cases having solid body rotation type and constant swirl vane angle type swirl generation at inlet. Different swirl numbers up to 1.5 are considered. The effect is studied for the mean axial and tangential velocities, streamline plots, turbulence kinetic energy and turbulence dissipation rate. With the increase of swirl strength, secondary on-axis recirculation is observed with the decrease of the primary corner recirculation. Swirl produces larger turbulence kinetic energy and enhances mixing rate, thus require shorter combustor length. Swirl generation by a constant vane angle swirl generator is found to have higher turbulence kinetic energy generation and consequently better mixing compared to that with solid body rotation swirl generation. The computational model is used to analyze the flow of the swirl combustor in which there is an inner swirling flow and a outer non-swirling flow. This non-swirling flow supplies cooling air to protect the wall material from burnout. The effect of the cooling air is also observed by changing the swirling and non-swirling flow rate ratios. The capability of the computational code for predicting swirling flows is also justified by comparing the code generated simulation results with the available experimental data.

## ACKNOWLEDGEMENT

The work was carried out under the guidance and supervision of Dr. Showkat Jahan Chowdhury, Professor, Department of Mechanical Engineering, Bangladesh University of Engineering and Technology (BUET) Dhaka. The author would like to express his profound gratitude and indebtedness to his supervisor for his careful supervision, encouragement and invaluable support during the course of this research work.

The author is thankful to the board of examiners, Dr. Md. Abdur Razzaq Akhanda, Dr. Md. Quamrul Islam and Dr. Md. Refayet Ullah for their suggestions and kind co-operation.

The author also thanks all others whom, directly or indirectly helped him during the research work.

# CONTENTS

Title	Page No.	
TITLE PAGE		
RECOMNDATION OF THE BOARD OF EXAMINERS	i	
DECLARATION OF THE CANDIDATE	ii	
CERTIFICATE OF RESEARCH	iii	
ABSTRACT	iv	
ACKNOWLEDGEMENT	v	
CONTENTS	vi	
LIST OF FIGURES	viii	
LIST OF SYMBOLS	xi	
CHAPTER 1	INTRODUCTION	
1.1	Background	1
1.2	Motivation of the Present Investigation	2
1.3	Literature Review	3
	1.3.1 History of Turbulence	3
	1.3.2 Previous Work	11
	1.3.3 Present Work	12
1.4	Objective of this Study	15
1.5	Outline of the Thesis	15
CHAPTER 2	METHODOLOGY OF SOLUTION	
2.1	Scope	17
2.2	Governing Equations	17
2.3	Solution Technique	21
2.4	Boundary Conditions	23
2.5	Solution Procedure	24
2.6	Closure	25
CHAPTER 3	RESULTS AND DISCUSSIONS	
3.1	Scope	26
3.2	Problem Statement	26
3.3	Comparison with Available Experimental Data	28
3.4	Effect of Constant Vane Angle Swirl Generation	29
	3.4.1 Effect on Swirling Turbulent Flow Pattern	30
	3.4.2 Effect on Mean Axial Velocity Profiles	31
	3.4.3 Effect on Mean Tangential Velocity Profiles	34
	3.4.4 Effect on Turbulence Kinetic Energy	36
	3.4.5 Effect on Turbulence Dissipation Rate	37
3.5	Effect of Solid Body Rotation Swirl Generation	37

	3.5.1 Effect on Swirling Turbulent Flow Pattern	38
	3.5.2 Effect on Mean Axial Velocity Profiles	40
	3.5.3 Effect on Mean Tangential Velocity Profiles	41
	3.5.4 Effect on Turbulence Kinetic Energy	43
	3.5.5 Effect on Turbulence Dissipation Rate	45
3.6	Closure	45

## CHAPTER 4 CONCLUSION

4.1	Summary of Main Findings	46
4.2	Suggestions for Future Work	48

<i>REFERENCES</i>	49
-------------------	----

<i>FIGURES</i>	54
----------------	----

## APPENDIX COMPUTER PROGRAMME FLOW CHART

104



# LIST OF FIGURES

FIGURES	Page No.
1. Geometry of confined swirling jet experimental setup for Brum and Samulsen.	54
2. Non-Uniform staggered grid.	55
3. Three control volumes associated with points of the three grids.	56
4. Nonuniform grid system employed to fit the flow domain.	56
5. Comparison of computed dimensionless mean axial velocity profiles with experimental data.	57
6. Comparison of computed dimensionless mean tangential velocity profiles with experimental data.	58
7. Comparison of computed dimensionless turbulence kinetic energy profiles with experimental data.	59
8. Streamline plots for constant vane angle swirl generator at inlet for Case-I.	60
9. Comparison of vector Diagram for combined axial and radial velocities at inlet for Constant vane angle swirl generator for Case-I.	61
10. Comparison of vector Diagram for combined axial and tangential velocities at inlet for constant vane angle swirl generator for Case-I.	62
11a. Comparison of dimensionless mean axial velocity profiles having constant vane angle swirl generator at inlet for Case-I.	63
11b. Comparison of dimensionless mean axial velocity profiles having constant vane angle swirl generator at inlet for Case-I.	64
12a. Comparison of dimensionless mean tangential velocity profiles having constant vane angle swirl generator at inlet for Case-I.	65
12b. Comparison of dimensionless mean tangential velocity profiles having constant vane angle swirl generator at inlet for Case-I.	66
13a. Comparison of dimensionless turbulence kinetic energy profiles having constant vane angle swirl generator at inlet for Case-I.	67
13b. Comparison of dimensionless turbulence kinetic energy profiles having constant vane angle swirl generator at inlet for Case-I.	68
14a. Comparison of dimensionless turbulence dissipation rate profiles having constant vane angle swirl generator at inlet for Case-I.	69
14b. Comparison of dimensionless turbulence dissipation rate profiles having constant vane angle swirl generator at inlet for Case-I.	70
15. Streamline plots for constant vane angle swirl generator at inlet for Case-II.	71
16. Comparison of vector Diagram for combined axial and radial velocities at inlet for constant vane angle swirl generator for Case-II.	72
17. Comparison of vector Diagram for combined axial and tangential	73

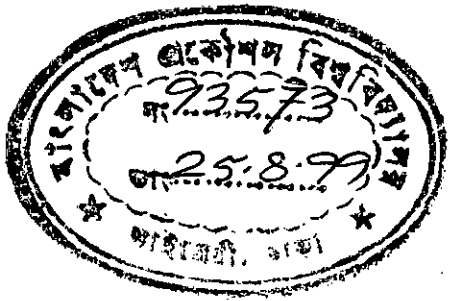
	velocities at inlet for constant vane angle swirl generator for Case-II.	
18a.	Comparison of dimensionless mean axial velocity profiles having constant vane angle swirl generator at inlet for Case-II.	74
18b.	Comparison of dimensionless mean axial velocity profiles having constant vane angle swirl generator at inlet for Case-II.	75
19a.	Comparison of dimensionless mean tangential velocity profiles having constant vane angle swirl generator at inlet for Case-II.	76
19b.	Comparison of dimensionless mean tangential velocity profiles having constant vane angle swirl generator at inlet for Case-II.	77
20a.	Comparison of dimensionless turbulence kinetic energy profiles having constant vane angle swirl generator at inlet for Case-II.	78
20b.	Comparison of dimensionless turbulence kinetic energy profiles having constant vane angle swirl generator at inlet for Case-II.	79
21a.	Comparison of dimensionless turbulence dissipation rate profiles having constant vane angle swirl generator at inlet for Case-II.	80
21b.	Comparison of dimensionless turbulence dissipation rate profiles having constant vane angle swirl generator at inlet for Case-II.	81
22.	Streamline plots for solid body swirl generator at inlet for Case-I.	82
23.	Comparison of vector Diagram for combined axial and radial velocities at inlet for solid body swirl generator for Case-I.	83
24.	Comparison of vector Diagram for combined axial and tangential velocities at inlet for solid body swirl generator for Case-I.	84
25a.	Comparison of dimensionless mean axial velocity profiles having solid body swirl generator at inlet for Case-I.	85
25b.	Comparison of dimensionless mean axial velocity profiles having solid body swirl generator at inlet for Case-I.	86
26a.	Comparison of dimensionless mean tangential velocity profiles having solid body swirl generator at inlet for Case-I.	87
26b.	Comparison of dimensionless mean tangential velocity profiles having solid body swirl generator at inlet for Case-I.	88
27a.	Comparison of dimensionless turbulence kinetic energy profiles having solid body swirl generator at inlet for Case-I.	89
27b.	Comparison of dimensionless turbulence kinetic energy profiles having constant solid body swirl generator at inlet for Case-I.	90
28a.	Comparison of dimensionless turbulence dissipation rate profiles having solid body swirl generator at inlet for Case-I.	91
28b.	Comparison of dimensionless turbulence dissipation rate profiles having solid body swirl generator at inlet for Case-I.	92
29.	Streamline plots for solid body swirl generator at inlet for Case-II.	93
30.	Comparison of vector Diagram for combined axial and radial velocities at inlet for solid body swirl generator for Case-II.	94
31.	Comparison of vector Diagram for combined axial and tangential velocities at inlet for solid body swirl generator for Case-II.	95
32a.	Comparison of dimensionless mean axial velocity profiles having solid body swirl generator at inlet for Case-II.	96
32b.	Comparison of dimensionless mean axial velocity profiles having solid body swirl generator at inlet for Case-II.	97
33a.	Comparison of dimensionless mean tangential velocity profiles having solid body swirl generator at inlet for Case-II.	98
33b.	Comparison of dimensionless mean tangential velocity profiles having solid body swirl generator at inlet for Case-II.	99

34a.	Comparison of dimensionless turbulence kinetic energy profiles having solid body angle swirl generator at inlet for Case-II.	100
34b.	Comparison of dimensionless turbulence kinetic energy profiles having solid body angle swirl generator at inlet for Case-II.	101
35a.	Comparison of dimensionless turbulence dissipation rate profiles having solid body swirl generator at inlet for Case-II.	102
35b.	Comparison of dimensionless turbulence dissipation rate profiles having solid body swirl generator at inlet for Case-II.	103

## LIST OF SYMBOLS

Symbol	Meaning
$C_1$	Turbulence model constant
$C_2$	Turbulence model constant
$C_D$	Turbulence model constant
$C_\mu$	Turbulence model constant
$k$	Turbulence kinetic energy
$k_{in}$	Inlet turbulence kinetic energy
$l$	Characteristic length scale
$p$	Mean pressure
$p'$	Fluctuating pressure
$r$	Radial distance
$R_1$	Radius of upstream tube
$R$	Radius of larger tube after expansion
$Re$	Reynolds number
$S_\varphi$	Source term for variable $\varphi$
$u$	Mean axial velocity
$U_{in}$	Inlet axial velocity
$U_0$	Reference velocity
$v$	Mean radial velocity
$v_i$	Instantaneous velocity in $i$ direction
$V_i$	Mean velocity in $i$ direction
$v_i'$	Fluctuating velocity
$w$	Mean tangential velocity
$x$	Axial coordinate
$S$	Swirl number

Greek Symbol	Meaning
$\varepsilon$	Dissipation rate of turbulence kinetic energy
$\nu$	Kinematic viscosity
$\nu_T$	Turbulent (Eddy) kinematic viscosity
$\mu$	Dynamic viscosity
$\mu_l$	Laminar dynamic viscosity
$\mu_T$	Turbulent dynamic viscosity
$\rho$	Constant mass density
$\sigma_\varphi$	Prandtl number for variable $\varphi$
$\omega_i'$	Turbulent fluctuating vorticity
$\delta_{ij}$	Kronecker delta (=1 when $i = j$ and =0 when $i \neq j$ )
$\alpha$	Expansion angle
$\theta$	Constant vane angle



# Chapter -1

## INTRODUCTON

### 1.1 BACKGROUND

Turbulent flow is very common in engineering application. As turbulent nature is not that orderly so it requires more attention. Turbulence is an irregular motion. It appears in fluids, gases or liquids when they flow past solid surfaces or even when neighboring stream of the fluid flow past one another. Hence the study of turbulence clearly is an interdisciplinary activity, which has a very wide range of application. The irregularity or randomness of turbulent flows, makes a deterministic approach to turbulence problems impossible, instead one relies on statistical methods. There are two types of turbulence (a) Turbulence generated by the viscous effect due to the presence of a solid wall is designated by wall turbulence (b) Turbulence in the absence of a wall generated by the flow of layers of fluids at different velocities is called free turbulence. Reynolds investigated many flow problems by Reynolds stress transport model (RSTM) and described the region of flow patterns as laminar, transition and turbulent which depend upon a characteristic dimensionless number called Reynolds number. At low Reynolds number flow is laminar and at high Reynolds number flow is turbulent. If there is any disturbance in the flow then the flow will be turbulent even in case of low Reynolds number. In turbulent flows, due to irregularities and random variation of flow quantities, high level of turbulence kinetic energy is generated and this causes rapid mixing and increases rates of momentum, heat and mass transfer as in combustion chamber of many appliances.

In high Turbulent Flow such as flows entering furnaces, jet engine combustors, boilers, etc. swirl is commonly imparted to all this kinds of flow. In order to

enhance flame stability and mixing for complete combustion. Swirl produces an adverse pressure gradient in the direction of motion that either increases recirculation, if this is already present due to a baffle, or provokes it, if swirl is sufficiently strong in the absence of such baffle. Flow separation and hence recirculation may also occur if there is sufficient change in the guiding wall geometry. Due to this recirculation, the desired mixing rate increases considerably, which in terms increases the combustion efficiency.

Turbulent swirling flow through an axisymmetric expansion has been studied earlier. But the literature review reveals that sufficient data are not available on the study of the flow properties for the swirling turbulent flow in combustion chambers with dilution or cooling air. The types of rotational motion, solid body or free vortex also have different effects on the stresses and turbulent energy. Hence detail knowledge of the flow properties are required before manufacturing the equipment encountering these types of flows.

For designing and developing of combustion chambers for gas turbines, jet engines Combustors, industrial furnaces, boilers etc., designers usually depend on experiments. But as a supplement to them, economical design, and operation can be greatly facilitated by the availability of prior predictions of the flow-field. These may be obtained by use of a mathematical model incorporating a numerical finite difference prediction procedure. A mathematical solution of the flow field of interest should provide results more cheaply and quickly than possible by experiments on real-life systems or models.

## 1.2 MOTIVATION OF THE PRESENT INVESTIGATION

The effect of swirling was numerically investigated for different swirling angles. But in real situation in a gas combustor some amount of cooling air is also supplied for dilution. Thus the effect is different and is commonly imparted to

enhance flame stability and mixing for complete combustion. Swirl produces an adverse pressure gradient in the direction of motion that either increases recirculation, if this is already present due to a baffle, or provokes it, if swirl is sufficiently strong in the absence of such baffle. Flow separation and hence recirculation may also occur if there is sufficient change in the guiding wall geometry. Due to this recirculation, the desired mixing rate increases considerably, which in terms increases the combustion efficiency.

Turbulent swirling flow through an axisymmetric expansion has been studied earlier. But the literature review reveals that sufficient data are not available on the study of the flow properties for the swirling turbulent flow in combustion chambers with dilution or cooling air. The types of rotational motion, solid body or free vortex also have different effects on the stresses and turbulent energy. Hence detail knowledge of the flow properties are required before manufacturing the equipment encountering these types of flows.

For designing and developing of combustion chambers for gas turbines, jet engines Combustors, industrial furnaces, boilers etc., designers usually depend on experiments. But as a supplement to them, economical design, and operation can be greatly facilitated by the availability of prior predictions of the flow-field. These may be obtained by use of a mathematical model incorporating a numerical finite difference prediction procedure. A mathematical solution of the flow field of interest should provide results more cheaply and quickly than possible by experiments on real-life systems or models.

## 1.2 MOTIVATION OF THE PRESENT INVESTIGATION

The effect of swirling was numerically investigated for different swirling angles. But in real situation in a gas combustor some amount of cooling air is also supplied for dilution. Thus the effect is different and is commonly imparted to



that man has been more than casually intrigued by it for nearly 500 years. The modern study of turbulence is usually dated from Osborne Reynolds (1842-1912). By this reckoning for more than 100 years researchers have been applying every tool and technique available to the problem. As the Reynolds number of the flow increases, the range of length and time scales required for solving the instantaneous turbulent motions by direct simulation increases rapidly exceeding the storage capacity of the largest computers in the future even for simple flow. On the other hand, most industrially important flows are quite complex and requires only knowledge of the averaged quantities.

Historical and recent developments in turbulence modeling were provided by Launder and Spalding [1972], Donaldson [1972], Reynolds [1976], Lumley [1978, 1983, 1992], Bradshaw, Cebeci and Whitelaw [1981], Zeman [1981], Rodi [1982], Hogg and Leschziner [1989], Panchapakesan and Lumley [1993] and Sanghi and Aubry [1993]. And recently by Tsao JM, Lin CA [1999], Paschereit, Gutmark, Weisenstein [1998]. A brief review of the fundamental assumptions is given in this section.

Reynolds upon time-averaging modified the Navier-Stokes equation as

$$\frac{\partial V_i}{\partial t} + \frac{\partial (V_i V_j)}{\partial x_j} = -\frac{1}{\rho} \frac{\partial p}{\partial x_i} + \frac{\partial}{\partial x_j} \left[ \nu \left( \frac{\partial V_i}{\partial x_j} + \frac{\partial V_j}{\partial x_i} \right) - \overline{v'_i v'_j} \right] \quad [1.1]$$

It is seen that the second term on the right hand side represent the viscous stresses in terms of the mean velocity gradient. The last term represents the Reynolds stresses or the apparent turbulent stresses due to the exchange of momentum in the turbulent mixing process. Here the number of unknowns are greater than the number of equations and hence closure assumptions are needed. This process is known as modeling .

The existing turbulence models can be categorized in several ways. According to the number of differential equations solved in addition to the mean flow equation

that man has been more than casually intrigued by it for nearly 500 years. The modern study of turbulence is usually dated from Osborne Reynolds (1842-1912). By this reckoning for more than 100 years researchers have been applying every tool and technique available to the problem. As the Reynolds number of the flow increases, the range of length and time scales required for solving the instantaneous turbulent motions by direct simulation increases rapidly exceeding the storage capacity of the largest computers in the future even for simple flow. On the other hand, most industrially important flows are quite complex and requires only knowledge of the averaged quantities.

Historical and recent developments in turbulence modeling were provided by Launder and Spalding [1972], Donaldson [1972], Reynolds [1976], Lumley [1978, 1983, 1992], Bradshaw, Cebeci and Whitelaw [1981], Zeman [1981], Rodi [1982], Hogg and Leschziner [1989], Panchapakesan and Lumley [1993] and Sanghi and Aubry [1993]. And recently by Tsao JM, Lin CA [1999], Paschereit, Gutmark, Weisenstein [1998]. A brief review of the fundamental assumptions is given in this section.

Reynolds upon time-averaging modified the Navier-Stokes equation as

$$\frac{\partial V_i}{\partial t} + \frac{\partial(V_i V_j)}{\partial x_j} = -\frac{1}{\rho} \frac{\partial p}{\partial x_i} + \frac{\partial}{\partial x_j} \left[ \nu \left( \frac{\partial V_i}{\partial x_j} + \frac{\partial V_j}{\partial x_i} \right) - \overline{v'_i v'_j} \right] \quad [1.1]$$

It is seen that the second term on the right hand side represent the viscous stresses in terms of the mean velocity gradient. The last term represents the Reynolds stresses or the apparent turbulent stresses due to the exchange of momentum in the turbulent mixing process. Here the number of unknowns are greater than the number of equations and hence closure assumptions are needed. This process is known as modeling .

The existing turbulence models can be categorized in several ways. According to the number of differential equations solved in addition to the mean flow equation

$$\frac{\partial V_i}{\partial t} + \frac{\partial(V_i V_j)}{\partial x_j} = -\frac{1}{\rho} \frac{\partial p}{\partial x_i} + \frac{\partial}{\partial x_j} \left[ (\nu + \nu_T) \left( \frac{\partial V_i}{\partial x_j} + \frac{\partial V_j}{\partial x_i} \right) \right] \quad [1.3]$$

$$\nu + \nu_T = \nu_{\text{eff}}$$

Prandtl [1925] introduced a concept for describing turbulent flow phenomena and proposed an algebraic equation, which is known as Prandtl's Mixing length Hypothesis. For nearly two dimensional boundary layer flows, particularly those developing over rigid boundaries, the mixing length hypothesis combines a good mixture of the attributes. Prandtl's suggestion for turbulent viscosity is

$$\nu_T = l_m^2 \left| \frac{\partial U}{\partial y} \right| \quad [1.4]$$

Where,  $l_m$  = mixing length ( $l_m = \kappa y$  where  $\kappa = 0.417$  in case of thin 2D boundary layer flows) i.e., turbulent viscosity is equal to the local product of the magnitude of mean rate of strain and the square of a characteristic length scale of the turbulent motion. Though the mixing length model has been successfully applied to a large number of thin shear layer flows [Spalding, 1982], it has several serious shortcomings. One of these is that it assumes local equilibrium condition, i.e., at any point of the flow turbulence production is balanced by the dissipation rate, and diffusion and convection are neglected. So, this model faces difficulties when diffusion or convection is important. The model also erroneously leads to zero value for turbulent viscosity and turbulent heat and mass diffusivities whenever the mean velocity gradient is zero. Furthermore, the effects due to buoyancy, rotation or streamline curvature on turbulence can only be introduced in an entirely empirical way, and hence generally applicable expressions are hard to formulate. Moreover, for complex flows, such as separated flows, empirical specification of the mixing length becomes impossible. Recent generation of turbulence modelings are essentially motivated by the so called Kolmogorov-Prandtl [Kolmogorov 1968, Prandtl 1945] hypothesis.

$$\mu_T = \rho V^* l^* \quad [1.5]$$

Where  $\mu_T$  is the turbulent (eddy) viscosity,  $V^*$  is a characteristic turbulent velocity scale and  $l^*$  is a characteristic turbulent length scale. While most existing models make use of this hypothesis, the methods for obtaining the relevant scales differ.

In one-equation models, a transport equation for a suitable turbulent velocity scale is used to account for the transport and history effects of turbulence. The kinematic eddy viscosity based on the Kolmogorov-Prandtl hypothesis is given by  $\nu_T = C_\mu k^{1/2} l$ , where  $k$  is the kinetic energy of turbulent motion. Usually,  $k^{1/2}$  acts as an appropriate velocity scale, as  $k = \frac{1}{2} \overline{v'_i v'_i}$ . The transport equation for  $k$  is derived by taking the cross moment of the Navier-Stokes equation [Launder and Spalding 1972].

The exact transport equation for turbulent kinetic energy.

$$\frac{\partial k}{\partial t} + V_j \frac{\partial k}{\partial x_j} = \overline{v'_i v'_i} \frac{\partial V_i}{\partial x_i} + \frac{\partial}{\partial x_j} \left( \nu \frac{\partial k}{\partial x_j} - k \overline{v'_j} - \frac{\overline{p' v'_j}}{\rho} \partial_j - \nu \frac{\partial v'_i v'_j}{\rho} \right) - \nu \frac{\partial v'_i}{\partial x_j} \left( \frac{\partial v'_i}{\partial x_j} + \frac{\partial v'_j}{\partial x_i} \right) \quad [1.6]$$

Equation [1.6] is changed with,

$$-\overline{v'_i v'_j} = \nu_T \left( \frac{\partial V_i}{\partial x_j} + \frac{\partial V_j}{\partial x_i} \right)$$

$$-k \overline{v'_j} = \frac{\nu_T}{\sigma_k} \frac{\partial k}{\partial x_j} ; \text{ Where } \sigma_k = \text{Prandtl number for } k = 1$$

$$-\nu \frac{\partial \overline{v'_i v'_j}}{\rho} \text{ And } \frac{\overline{p' v'_j}}{\rho} \partial_j \text{ are neglected.}$$

$$v \frac{\partial v'_i}{\partial x_j} \left( \frac{\partial v'_i}{\partial x_j} + \frac{\partial v'_j}{\partial x_i} \right) = \text{Dissipation rate } \varepsilon.$$

So, the k transport equation becomes,

$$\frac{\partial k}{\partial t} + V_j \frac{\partial k}{\partial x_j} = v_T \left( \frac{\partial V_i}{\partial x_j} + \frac{\partial V_j}{\partial x_i} \right) \left( \frac{\partial V_i}{\partial x_k} \right) + \frac{\partial}{\partial x_j} \left[ (v + v_T) \frac{\partial k}{\partial x_j} \right] - \varepsilon \quad [1.7]$$

Putting  $v_T \left( \frac{\partial V_i}{\partial x_j} + \frac{\partial V_j}{\partial x_i} \right) \left( \frac{\partial V_i}{\partial x_k} \right) = G$  (generation term).

Finally transport equation for k becomes,

$$\frac{\partial k}{\partial t} + V_j \frac{\partial k}{\partial x_j} = G + \frac{\partial}{\partial x_j} \left[ (v + v_T) \frac{\partial k}{\partial x_j} \right] - \varepsilon \quad [1.8]$$

In these models, the length scale is still specified by an algebraic equation. So, shortcomings still exist, as an algebraic expression is too restrictive. Since algebraic expression can not have convection and diffusion, transport of length scale is not considered. Moreover, for complex flows with separation, streamline curvature or rotation, the empirical specification of the length scale faces a number of difficulties. As a result, though the one-equation model has convection and diffusion of the velocity scale, yet due to significant limitations of algebraic expressions for length scale, they offer little improvement over the zero equation models.

In order to overcome the shortcomings of the one-equation models, came the two-equation models which have transport equations for both turbulent velocity scale and turbulent length scale. The use of transport equation for the length scale

l, accounts for the evolution of the spatial scale of turbulence throughout the flow regions. In this length scale transport equation, the dependent variable can be any combination of l and k. various combination of two equation models have been proposed. Launder and Spalding [1972, 1974] and Jones and Launder [1972, 1973] used an equation for the dissipation rate as  $\varepsilon = C_D k^{3/2} / l$ , which is the transport equation for  $\varepsilon$ . Here,  $C_D$  is a constant. So, the model is also called k- $\varepsilon$  model.

Modifying Equation [1.8] slightly and introducing c in places of k, the transport equation for dissipation rate c can be written as,

$$\frac{\partial \varepsilon}{\partial t} + V_i \frac{\partial \varepsilon}{\partial x_i} = C_1 \frac{G\varepsilon}{k} + \frac{\partial}{\partial x_i} \left[ (v + \nu_T) \frac{\partial k}{\partial x_i} \right] - \frac{C_2 \varepsilon \varepsilon}{k} \quad [1.9]$$

Where,  $C_1, C_2$  are constants and  $\sigma_\varepsilon = 1.3$

This model has been widely used in most industrial applications. One reason for the popularity of the two-equation models is that it can be conveniently accommodated in the computer codes for solving the Navier-Stokes equation. It also offers considerable saving in computational time when compared to the more sophisticated stress transport models. However, the standard k- $\varepsilon$  model also has some limitations. Here, the eddy viscosity and diffusivity are assumed to be isotropic. These may not be equal in all three directions, so the model becomes incapable of predicting the observed secondary flows in rectangular ducts. The effects of curvature, rotation and buoyancy forces have to be modeled separately. In addition, k-equation accounts only for transport of normal stresses. So convection and diffusion of the shear stresses are neglected.

In the stress-transport model, to account for the evolution of the individual stress components, transport equations for each component of  $\overline{v'_i v'_j}$  have been introduced. Exact equations for the  $\overline{v'_i v'_j}$  can be obtained directly from the

Navier-Stokes equation. However, these transport equations contain unknown higher order correlation, which have to be approximated by closure assumptions. In exact Reynolds stress equation, however, terms accounting for buoyancy, rotation, and other effects are introduced automatically. In modeling, turbulence processes are assumed to be characterized by a single time-scale,  $k/\epsilon$ , where  $k$  is the kinetic energy of turbulence fluctuating motion. In addition, local isotropy for dissipation is assumed to prevail so that the dissipation is same for all three normal components. The modeled Reynolds stress transport equations along with that for energy dissipation rate  $\epsilon$ , have to be solved simultaneously. Here, 11 equations have to be solved for 11 unknowns. Thus considerable computational effort is needed for solving practical engineering problems. Daley and Harlow [1970], Hanjalic and Launder [1972, 1976] also developed elaborate stress transport models, Lumley and Khajeh-Nouri [1974], Launder, Recce and Rodi [1975] and Newman, Launder and Lumley [1981].

In the stress transport models, one has to solve a large number of differential equations for each component of turbulent stresses and Influxes, which requires extensive computational effort. To reduce the computational work, algebraic stress models have been developed by Rodi [1976], Yoshizawa [1984, 1985], Speziale [1987], Chowdhury [1990] and Ahmadi and Chowdhury [1991].

In spite of the extensive research effort to develop more accurate turbulence models, the  $k$ - $\epsilon$  model of turbulence is still widely used in industries for solving practical flow problems. One main reason the required computational effort for application of stress transport models to industrial fluid engineering problems is quite extensive, since the transport equations for each component of the Reynolds stress tensor have to be solved. Furthermore, in order to close the exact transport equations for the Reynolds stresses, closure approximations for the higher order turbulence correlations such as pressure-strain terms are required which are difficult to achieve. Many turbulence researchers [Speziale 1987] believe that the above mentioned shortcomings outweigh the main advantages of second order closures in practical applications. The other reason for the popularity of the  $k$ - $\epsilon$

model is that it has been accommodated into many commercially available computer codes.

### 1.3.2 Previous Work:

Some aspects of turbulence and combustion modeling of swirl- stabilized LPP combustion and Heat transfer in counters-whirled coaxial jet mixing were studied numerically and experimentally by Smirnov [1998], Dellenback PA [1998]. Before them Moon and Rudinger [1977], Yang and Yu [1983], Gould, Stevenson and Thompson [1983], Stevenson, Thompson and Gould [1983] and Amano [1983] worked on axial flow through a sudden axisymmetric expansion, but the swirling effect was not considered. Chaturvedi used a hot-wire anemometer to measure the turbulence quantities. Freeman used a Laser Doppler Anemometer (LDA) to measure axial mean velocity and turbulence intensity, Stevenson used k- $\epsilon$  models for Reynolds stresses. Amano studied the turbulent flow downstream of an abrupt pipe expansion. In this paper, a numerical investigation is reported of heat transfer in the separated flow region created by an abrupt pipe expansion. Hybrid differencing, a combination of central and upwind finite differencing, has been applied in the computations to solve the Navier-Stokes equation with the k- $\epsilon$  turbulence model.

Gutmark, Paschereit studied control of combustion instabilities and emissions in a gas-turbine combustor using unstable thermoacoustic modes controlled in an experimental low-emission swirl stabilized combustor, in which the acoustic boundary conditions were modified to obtain combustion instability. Computation of highly swirling confined flow with a Reynolds stress turbulence model was performed by Hogg and Leschziner [1989], these paper addresses the problem of computing a strongly swirling confined turbulent flow akin to that encountered in combustors.



Axisymmetric expansion with swirl was also studied by Jackson and Lilley [1983], Rhode, Lilley and McLaughlin [1983], Sultanian [1984] and Abujelala, Jackson and Lilley [1984]. They investigated swirling turbulent flows through sudden expansions but all have used intrusive probes, even though it is known that such probes can significantly alter flow fields with recirculation. In fact, these studies are concerned primarily with the development of measurement techniques using five-hole pitot tubes and hot wire anemometer for application in multidimensional complex flows. Their presentations might be considered work in progress on the development of measurement techniques rather than a collection of results available for comparison purposes.

Measurements in turbulent swirling flow through abrupt axisymmetric expansion was performed by Dellenback, Metzger and Nietzel [1988]. Experimental data are presented for both axial and tangential velocity components in turbulent swirling flow downstream of an abrupt 1:2 expansion. Measurements of mean and rms velocities were performed in a water flow with a Laser Doppler Anemometer.

This thesis, therefore, analyses numerically the effects of swirling turbulent flow on various fluid properties for different types of swirling with cooling air flow and uses the hybrid differencing scheme and  $k-\epsilon$  turbulence model in the computer code of Chowdhury [1990].

### 1.3.2 Present Work:

Reynolds stress modelling of jet and swirl interaction inside a gas turbine combustor is studied by Tsao JM, Lin CA [1999]. Influence of the inlet swirl levels on the interaction between the dilution air jets and the swirling cross-flow

to the interior flow field inside a gas turbine combustor were investigated numerically by Reynolds stress transport model (RSTM). Due to the intense swirl and jet interaction, a high level of swirl momentum is transported to the centreline and hence, an intense vortex core is formed. The strength of the centreline vortex core was found to depend on the inlet swirl levels. For the higher swirling inlet, the decay of the swirling motion causes strong streamline variation of pressure; and consequently leads to an elevated level of deceleration of its axial velocity. Predictions contrasted with measurements indicate that the stress model reproduces the flow correctly. Results of application of the maximum flowrate principle to correct the kappa-epsilon turbulence model in swirling flow situations are presented by Smirnov A, Lipatnikov A, Chomiak J [1998]. They used Non-reacting swirling flows with and without heat transport as well as reacting swirl flows. A Combustion of A-jet fuel in stoichiometric and lean regimes is simulated. Velocity measurements and turbulence statistics of a confined isothermal swirling flow was studied by Ahmed SA [1998]. A free vortex swirler was used to stir the flow at the inlet of the combustor. Measurements of mean velocities, Reynolds normal and shear stresses, and triple products were carried out at axial distances ranging from 0.38 H (step height) to 18 H downstream of the swirler. Experimental data are provided to help in the understanding of the behavior of swirling, recirculating, axisymmetric, and turbulent flows inside dump combustors. A balance of the turbulence energy equation has been performed in order to get a insight into the turbulent shear layer behavior.

Simulation of pulverized coal test furnace performance was done by Lockwood FC, Mahmud T, Yehia MA [1998]. A non-intrusive, two-component laser Doppler velocimeter was employed to measure the flow properties of a confined, isothermal, swirling flowfield in an axisymmetric sudden expansion research combustor. Ahmed SA [1998] used a non-intrusive, two-component laser Doppler velocimeter to measure the flow properties of a confined, isothermal, swirling flowfield in an axisymmetric sudden expansion research combustor. Numerical simulations of coal-fired swirl rectangular combustor were done by Su

A. Chang JH, Ho WC [1998] for this a CFD solver CFX is used to simulate combustion behavior inside a wall-fired rectangular coal combustor. Sanger JL, Dellenback PA [1998] worked on convective heat transfer for the mixing of two counters-whirled coaxial jets confined by a constant diameter tube. Local heat transfer coefficients were found to be a strong function of streamwise position and annular swirl number at low values of MFR, yet at high values of MFR, there is minimal streamwise variation in heat transfer coefficient as the mean flow largely dictates heat transfer rates.

In 1997 Park TW, Roquemore WM, Katta VR, Aggarwal SK investigated a two-phase flow field in a simplified swirl cup combustor numerically, the effects of the swirl mode and temperature of the primary and secondary air on the gas-phase flow field and the effect of droplet injection characteristics in terms of velocity and location on the droplet transport and vaporization behavior were studied. Calculation of a premixed swirl combustor using the PDF method was done by Hsu AT, Anand MS, Razdan MK [1997]. With this method, the chemical reaction rates are treated without approximation. In contrast, the conventional Reynolds-average methods need to model the mean reaction rates in turbulent flame calculations. In addition, conventional methods require special models for premixed flames that are developed under restrictive assumptions and rely on ad hoc expressions for the rate of reaction progress. The present work demonstrates the capability of the PDF method in realistic combustor design calculations. A lean premixed flame swirl combustor is simulated using the scalar PDF method, and the results are compared with experimental data. It is shown that the PDF method can correctly predict the turbulent flame speed and location of the flame. Xia JL, Smith BL, Benim AC, Schmidli J, Yadigaroglu G [1997] studied the effects of inlet and outlet boundary conditions on swirling flows. Numerical simulations are conducted for both three-dimensional, turbulent flow in a multichannel swirler and axisymmetric, isothermal, turbulent flow in combustion chambers using the standard kappa-epsilon turbulence model.

## 1.4 OBJECTIVE OF THIS STUDY

The objective of this thesis is to study numerically the effect of swirling flow with cooling air on different flow characteristics. A modified version of the TEACH computer program, capable of handling swirling turbulent flow, will be used for the present study. This fast and reliable computer program was adopted from Chowdhury [1990], for solving the governing finite difference equations for given boundary conditions. The velocity components, turbulence kinetic energy, dissipation rate, etc., are to be calculated at different section of the mixing chamber (combustion chamber) for different angles of expansion with different swirl generators and swirl numbers. The specific objectives of this research are:

1. To study the flow properties with various level of swirl in the combustor.
2. To study the comparative effects of swirling between constant vane angle swirl generator and solid body swirl generator at the inlet.
3. To study the effects of swirl strength on the flow properties.
4. To study the effect of non-swirling cooling air jet around the swirling flow.
5. To verify the exactness of predicted (generated) flow properties with the model.

## 1.5 OUTLINE OF THE THESIS

The main purpose of this thesis is to analyze numerically the effects of various swirling flow and its effects on fluid properties. The governing equations required

for this numerical study, along with the solution techniques and boundary conditions are briefly given in Chapter 2 of this thesis.

Chapter 3 contains the results and discussion. In this chapter, the predicted results are first compared with the available experimental data to ensure the capability of the program. Then the effects of different swirl generators and swirl strengths on different flow properties were studied for two cases. Case-I is for 15.4 m/s non-swirling inlet jet and Case-II is for 7.7 m/s non-swirling inlet jet.

The summary of the main findings of this thesis and the suggestions for future work are presented in Chapter 4.

References and Figures are given at the end of this thesis.

# Chapter – 2

## METHODOLOGY OF SOLUTION

### 2.1 SCOPE

The method of the numerical simulation is briefly described. In comparison to other sophisticated models, considering the economic point of view, k-ε model is used to solve this axisymmetric, steady, swirling turbulent flow. The governing equations are first summarized. The solution technique is then briefly outlined. Boundary conditions are also described in short. Finally, the line-by-line solution method along with underrelaxation principle is briefly discussed. Closing remarks are also given.

### 2.2 GOVERNING EQUATIONS

The equations which govern the flow of an incompressible fluid are:

$$\text{Continuity equation, } \frac{\partial v_i}{\partial x_i} = 0 \quad [2.1]$$

$$\text{Momentum equation, } \rho \left( \frac{\partial v_i}{\partial t} + v_j \frac{\partial v_i}{\partial x_j} \right) = - \frac{\partial p}{\partial x_i} + \mu \frac{\partial^2 v_i}{\partial x_j \partial x_j} \quad [2.2]$$

Actually in a state of turbulent motion, the field quantities become random functions of space and time. The instantaneous motions will still satisfy Equations 2.1 and 2.2, but will become too complex and mathematically untraceable. The usual approach is to use an averaging technique and to deal with the rather smooth variation of the mean flow field. In turbulence modeling, the complex motion of a simple (Newtonian) fluid is replaced by a simple motion of a complex mean field fluid.

During turbulent motions, the flow parameters may be decomposed into mean and fluctuating parts, i.e.,

$$v_i = V_i + v_i' \quad [2.3]$$

Where,  $V_i$  is the mean (expected value) and  $v_i'$  is the fluctuating part of the instantaneous variable  $v_i$ .

By time averaging we get,

$$\overline{v_i} = 0, \text{ and } \overline{V_i} = V_i, \text{ hence } \overline{v_i} = V_i \quad [2.4]$$

Now, substituting the instantaneous variables by their mean and fluctuating components, time-averaging and rearranging, the continuity and momentum equations become,

$$\frac{\partial V_i}{\partial x_i} = 0 \quad [2.5]$$

$$\left( \frac{\partial V_i}{\partial t} + V_j \frac{\partial V_i}{\partial x_j} \right) = \frac{1}{\rho} \frac{\partial p}{\partial x_i} + \nu \frac{\partial^2 v_i}{\partial x_j \partial x_j} - \frac{\partial}{\partial x_j} (\overline{v_j' v_i'})$$

[2.6]

Equation [2.6] is known as the Reynolds Equation for turbulent flow,

where  $-\overline{v'_i v'_j}$  is the turbulent stress tensor.

Here the numbers of unknowns are more than the number of equations and hence closure assumptions are required. These are the functions of turbulence. In this thesis, the k-ε turbulence model of Launder and Spalding [1974] is used. In this model, there are also two transport equations for kinetic energy of turbulence, k and dissipation rate, ε. The turbulent energy and its dissipation rate are defined as,

$$k = \frac{1}{2} \overline{v'_i v'_i} \quad \& \quad [2.7]$$

$$\varepsilon = 2\nu \overline{\omega'_i \omega'_i}$$

where  $v'_i$  is the fluctuating velocity and  $\omega'_i$  is the fluctuating vorticity of turbulence. The turbulent stress tensor is defined as,

$$-\overline{v'_i v'_j} = \nu_T \left( \frac{\partial V_i}{\partial x_j} + \frac{\partial V_j}{\partial x_i} \right) - \frac{2}{3} k \delta_{ij} \quad [2.8]$$

According to this model the transport equations for k and ε are given by,

$$\frac{dk}{dt} = \frac{\partial}{\partial x_j} \left( \frac{\nu_T}{\sigma_k} \frac{\partial k}{\partial x_j} \right) + \nu_T \left( \frac{\partial V_i}{\partial x_j} + \frac{\partial V_j}{\partial x_i} \right) \frac{\partial V_i}{\partial x_j} - \varepsilon \quad [2.9]$$

$$\frac{d\varepsilon}{dt} = \frac{\partial}{\partial x_j} \left( \frac{\nu_T}{\sigma_\varepsilon} \frac{\partial \varepsilon}{\partial x_j} \right) + C_1 \nu_T \frac{\varepsilon}{k} \left( \frac{\partial V_i}{\partial x_j} + \frac{\partial V_j}{\partial x_i} \right) \frac{\partial V_i}{\partial x_j} - C_2 \frac{\varepsilon^2}{k} \quad [2.10]$$

$$\nu_T = C_\mu \frac{\varepsilon^2}{k} \quad [2.11]$$

where  $C_1$  and  $C_2$  are two constants,  $\sigma_k$  and  $\sigma_\varepsilon$ , are the Prandtl numbers for k



and  $\varepsilon$ .

Jones and Launder [1973] proposed the constants to be as,

$$C_{\mu} = 0.09, C_1 = 1.45, C_2 = 1.9, \sigma_k = 1.0 \text{ and } \sigma_{\varepsilon} = 1.3. \quad [2.12]$$

The resulting governing equations for turbulent fluid flow are all similar and hence can be put in the common form:

$$\frac{1}{r} \left[ \frac{\partial}{\partial x} (\rho u \phi) + \frac{\partial}{\partial r} (\rho v r \phi) - \frac{\partial}{\partial x} \left( r \Gamma_{\phi} \frac{\partial \phi}{\partial x} \right) - \frac{\partial}{\partial r} \left( r \Gamma_{\phi} \frac{\partial \phi}{\partial r} \right) \right] = S_{\phi} \quad [2.13]$$

In Equation 2.13 the first two terms are the convection terms, third and fourth terms are the diffusion terms and  $S_{\phi}$  is the source term which contains terms describing the generation (creation) and consumption (dissipation) of variable  $\phi$ . The forms for the source term  $S_{\phi}$  are given in Table 2.1. For pseudo two-dimensional case the change in azimuthal direction ( $\partial/\partial\theta$ ) is assumed to be zero.

**Table 2.1: Source Terms for the General Equation (Equation 2.13).**

Values of $\phi$	Name of Equation	Source Term, $S_{\phi}$
1	Continuity	0
u	u-momentum (axial)	$-\frac{\partial p}{\partial x} + S''$
v	v-momentum (radial)	$-\frac{\partial p}{\partial r} + \frac{\rho w^2}{r} - \frac{1}{r^2} \frac{\partial}{\partial r} (r \mu v) + S''$
w	w-momentum (tangential)	$-\frac{\rho v w}{r} - \frac{w}{r^2} \frac{\partial}{\partial r} (r \mu)$
k	k-equation	$G - C_D \rho \varepsilon$
$\varepsilon$	$\varepsilon$ -equation	$C_1 \varepsilon G - C_2 \rho \varepsilon^2 / k$

Here,

$$S^{ii} = \frac{\partial}{\partial x} \left( \mu \frac{\partial u}{\partial x} \right) + \frac{1}{r} \frac{\partial}{\partial r} \left( r \mu \frac{\partial v}{\partial x} \right) \quad [2.14]$$

$$S^v = \frac{\partial}{\partial x} \left( \mu \frac{\partial u}{\partial x} \right) + \frac{1}{r} \frac{\partial}{\partial r} \left( r \mu \frac{\partial v}{\partial x} \right) \quad [2.15]$$

$$G = \mu \left[ 2 \left\{ \left( \frac{\partial u}{\partial x} \right)^2 + \left( \frac{\partial v}{\partial r} \right)^2 + \left( \frac{v}{r} \right)^2 \right\} + \left( \frac{\partial u}{\partial r} + \frac{\partial v}{\partial x} \right)^2 + \left\{ r \frac{\partial}{\partial r} \left( \frac{w}{r} \right) \right\}^2 + \left( \frac{\partial w}{\partial x} \right)^2 \right] \quad [2.16]$$

$$\mu = C_\mu \rho k^2 / \varepsilon + \mu_1 \quad \text{and} \quad \Gamma_\phi = \mu / \sigma_\phi \quad [2.17]$$

For continuity equation  $\Gamma_\phi = 0$  and for the momentum equations  $\sigma_\phi = 1$ . The above equations have to be solved for the time mean pressure  $p$ , velocity component  $u$ ,  $v$  and  $w$ , turbulence energy  $k$  and dissipation rate  $\varepsilon$ .

## 2.3 SOLUTION TECHNIQUE

The basic TEACH computer program using SIMPLE (Semi-Implicit Method for Pressure Linked Equations) with TDMA (tri-diagonal matrix algorithm) provides the starting point upon which the computer code is based. The solution technique incorporates displaced grids for the axial and radial velocities  $u$  and  $v$ , which are placed between the nodes where pressure  $p$  and other variables are stored. An implicit line-by-line relaxation technique is employed in the solution procedure (requiring a tridiagonal matrix to be inverted in order to update a variable at all points along a column), using the TDMA. The incorporation of these enhances the accuracy and rapidity of convergence of the computer program.

The differential equations presented in the previous section are in their exact form. In order to solve these equations, the exact differential equations are first to be converted into approximate finite difference equations. The finite difference equations are solved on a complex mesh illustrated in Figure 2. The intersection, the point P for example, of the solid lines mark the grid nodes where all variables except u and v velocity components are stored. The letters are stored at points which are denoted by arrows (and labeled w and s respectively) located midway between the grid intersections, and the boomerang-shaped envelope encloses a triad of points with reference location P at (I,J). This is the well-known staggered grid system. Details of the special merits of this staggered grid system have been reported by Patankar [1980]. The different control volumes C, U, and V which are appropriate for the P, w and s locations respectively are given in Fig. 3.

The finite difference equations for each  $\phi$  are obtained by integrating Equation [2.13] over the appropriate control volume (centered about the location of  $\phi$ ) and expressing the result in terms of neighbouring grid point values. Here, a hybrid scheme which is a combination of the so-called central and upwind finite differencing have been employed to discretize the equations. The advantages of this hybrid-differencing scheme over central-difference and upwind scheme have been described in detail by Patankar [1980]. The discretized equations can finally be written in a general form as:

$$a_p \phi_p = \sum_j a_j \phi_j + S_u \quad [2.18]$$

where,

$$a_p = \sum_j a_j - S_p$$

$\sum_j$  = sum over N, S, E and W neighbors thus linking each ( $\phi$ -value at a point P with its four neighboring values.

## 2.4 BOUNDARY CONDITIONS

The flow-field under consideration is covered with a non uniform grid system as shown in Fig. 4. Typically the boundary of the solution domain falls halfway between its immediate nearby parallel grid lines. Clearly, specification of the  $x$  and  $r$  coordinates of the grid lines, together with specification of  $JMAX(I)$  for each  $I$  is sufficient to determine the flow field of interest. Upto this point the application of boundary conditions has not yet been considered, and the formulation has been concerned with regular internal mesh points. The finite difference formulation requires amendment for the near boundary points through insertion of correct boundary conditions. The boundary conditions for the present flow field are briefly discussed below.

### i. Inlet Boundary:

At the inlet, the axial velocity ( $u$ -velocity) is specified and the radial velocity is considered to be zero. The tangential velocity at inlet depends on the type of swirl generation. For the case of solid body rotation swirl generator at inlet, solid body rotation profile is used for the tangential velocity, i.e.  $w$ -velocity changes linearly with radius. For the case of constant swirl vane angle at inlet, the tangential velocity is calculated from  $W = U \tan\theta$ , where  $\theta$  is the vane angle. The turbulence kinetic energy  $k$  and dissipation rate  $\epsilon$  are also specified at the inlet through the following relation,

$$k_{in} = \lambda_1 U_{in}^2 \quad \epsilon_{in} = \frac{k_{in}^{3/2}}{\lambda_2 R} \quad [2.19]$$

When  $U_{in}$  is the mean inlet velocity, and  $\lambda_1$ , and  $\lambda_2$  are some constants.

**ii Outlet Boundary:**

The axial velocities at the outlet are deduced from their immediate upstream values. Zero normal gradient is specified for all other variables at the outlet.

**iii Top Side Wall:**

At the top and side solid wall, no slip boundary conditions are applied. Near wall tangential velocities are connected with their zero wall values by ways of the tangential shear stress wall functions.

**iv Symmetry Axis:**

At this axis of symmetry, zero normal gradients are specified for all the variables except the radial velocity. The radial velocity is given zero values at this symmetry axis.

## 2.5 SOLUTION PROCEDURE

The finite difference equations and boundary conditions constitute a system of strongly coupled simultaneous algebraic equations. They form a set of nonlinear equations. As already mentioned, a modified version of the TEACH Computer program of Chowdhury [1990], capable of handling swirling turbulent flows, is used for the present study. The governing equations are solved by standard finite volume technique. A non uniform grid with finer spacing in the regions of large spatial gradients is used, along with staggered control volumes. The nonlinear algebraic equations are solved by an iterative technique. Values of all the variables are first guessed. The software is based on SIMPLE (Semi-Implicit Method for Pressure Linked Equations). The act of equations are solved by using the

tridiagonal matrix algorithm (TDMA). This solution is considered as improved guess and the iteration is repeated until a convergence criterion is satisfied.

At each iteration, it is necessary to employ some degree of under-relaxation. A weighted average of the newly calculated value and the previous value is taken at each point. Because, if the corrections are too large per iteration, the non linearity of the finite difference equations causes divergence. Velocity and pressure corrections per iteration become smaller as the solution proceeds towards convergence.

Final convergence is decided by way of a residual-source criterion, which measures the departures from exactness for the variable  $\phi$  at the point. The residual sources are defined for each variable at each point by equation like,

$$R_p = a_p - \sum_j a_j \phi_j - S_u \quad [2.20]$$

The solution is considered to be converged if the cumulative sum of the absolute residuals throughout the field for all variables is less than 0.4 percent of the inlet flow rate of the corresponding variable.

## 2.6 CLOSURE

The governing differential equations are presented in this chapter in a form that is used in the computer program. The solution technique, finite difference formulations, and boundary conditions are discussed briefly. Finally, the solution procedure is also outlined.

An available computer program is used to simulate the present flow-field and the results are discussed in the next chapter.

# Chapter – 3

## RESULTS AND DISCUSSION

### 3.1 SCOPE

This chapter presents the results of numerical simulation of the swirling turbulent flow through a swirl combustor, using a modified version of the TEACH Computer code of Chowdhury [1990]. The governing equations using the k- $\epsilon$  model, presented in the previous chapter, are used for the present study. First, the problem is defined. Then, for verifying the validity of the programme, comparison is made with the solution of the problem for a particular case for which experimental data are available. The effect of different types of swirl generation and swirl strength at inlet are then studied. Also the effect of changing the non swirling (cooling) and swirling jet ratios are investigated. The results are discussed and finally closing remarks are given.

### 3.2 PROBLEM STATEMENT

As already mentioned, the confined turbulent flow in a swirl combustor with cooling air is analyzed numerically in this thesis. The flow geometry is shown in Fig.1. Three coaxial tubes are considered at the inlet section. The radius of the outer most tube is 4 cm and the middle tube is 2.9 cm. The core tube is 0.95 cm radius and blocked at the inlet. The swirl generator is placed in the middle annular section surrounding the blocked tube. Hence, swirling turbulent flow comes through this middle annular section with an axial velocity  $U_1$  and non swirling

cooling air comes in through the outer annular section with an axial velocity  $U_2$ . After the inlet section, the flows then expand suddenly to the central part of the 4.0 cm radius tube, and interact with each other. At the inlet, axial and tangential mean velocity profiles are specified. The swirling flow comes in with an axial velocity  $U_1 = 15.6$  m/s. For the ratio of the flow rates of swirling and non swirling jets,  $Q_1:Q_2 = 1.0$  and  $2.0$ , the velocity of the non swirling flow is taken as  $U_2 = 15.4$  m/s (Case-I) and  $7.7$  m/s (Case-II), respectively. Swirl can be generated by solid body rotation swirl generator or by applying vanes at constant angle at inlet. Swirl number and Reynolds number are calculated by,

$$S = \frac{\int_0^{R_2} r^2 U_{in} W_{in} dr}{R_2 \int_0^{R_2} r U_{in}^2 dr}, \quad R_e = \frac{2 R_2 U_{in} \rho}{\mu} \quad [3.1]$$

Where,  $U_{in}$  and  $W_{in}$  are the inlet mean axial and tangential velocities respectively.

Uniform profiles for the turbulence kinetic energy and dissipation rate are also assumed at the inlet. The inlet turbulent kinetic energy and dissipation rate are calculated by,

$$k_{in} = 0.03 U_{in}^2, \quad \epsilon_{in} = k_{in}^{3/2} / 0.02 R \quad [3.2]$$

Where,  $U_{in}$  is the inlet mean velocity. Das [1992] studied the effect of grid size variation and recommended grid size of  $46 \times 34$  nodes. Hence, the flow field is solved for a non uniform staggered grid of size  $46 \times 34$  (i.e., there are 46 grids in the axial direction and 34 grids in the radial direction) with finer spacing in the regions of large spatial gradients. The results are described in the subsequent sections.



### 3.3 COMPARISON WITH AVAILABLE EXPERIMENTAL DATA

The results obtained from the program is compared with the experimental result from Brum and Samuelsen measurement of velocity and turbulence. The flow field measured was a nonreacting, confined swirling flow in an 8-cm-diameter tube. The tube was 50 cm long with a two-color laser anemometry system. The swirl was generated by a 12-vane sheet metal swirler at the inlet cross-section. The hub of the  $60^\circ$  swirler was 19 mm in diameter and the tip was 57 mm in diameter with solid body rotation. For these measurement a 50-percent split of swirler to cooling air was maintained. This flow was simulated using the computer code of Chowdhury [1990], which is a modified version of the TEACH Computer Code. A non uniform grid of size 46 x 34 node points is used and the governing equations employing the k- $\epsilon$  model are given in Chapter 2 of this thesis. Simulation is done for the experimental case of constant vane angle swirl generator with vane angle of  $60^\circ$  ( $S=1.15$ ). During computation, the inlet profiles for the mean axial and tangential velocities are specified and inlet swirling velocity of 15.6 m/s with non swirling jet of 15.4 m/s was maintained. The predictions of the numerical model are compared with the experimental results of Brum and Samuelsen [1988] in Figs.5, 6, and 7. In these figures, the solid lines correspond to the numerical predictions of the present model and the triangular marks correspond to the experimental data.

The mean axial velocity distribution across the flow as predicted by the present numerical model at different axial locations,  $X/R = 0.25, 0.50$  and  $2.5$  are shown in Fig.5. Here  $X$  is the axial distance from the sudden expansion section and  $R$  is the radius of the larger pipe. The experimental data of Bum and Samuelsen [1988] are also shown in this figure for comparison. The velocities have been nondimensionalized with the aid of the reference velocity  $U_0$ . It is observed that the model predictions for the mean axial velocity are in reasonable agreement with the experimental data. Considering these the model predictions for the mean axial velocity field are said to be in good agreement with the experimental data.

Comparison of tangential velocity field with experimental data of Brum and Samulsen is given in Fig.6. Here also, the tangential velocity is nondimensionalized with the aid of the reference velocity  $U_0$ . Considering the above probable causes of variation, the model predictions for the tangential velocity field are said to be in good agreement with the experimental data.

Comparison of turbulence kinetic energy with experimental data of Brum and Samuelsen is given in Fig.7. Here also, the turbulence kinetic energy is nondimensionalized with the aid of the reference velocity  $U_0^2$ . Considering the above probable causes of variation, the model predictions for the turbulence kinetic energy are said to be in good agreement with the experimental data.

Based on the above presented results and comparison with experimental data, it may be concluded that the present numerical model has the capability of predicting the swirling turbulent flows with reasonable accuracy. Hence for the present investigation this model will be used for further simulations in the following sections.

### 3.4 EFFECT OF CONSTANT VANE ANGLE SWIRL GENERATION

In section 3.2 of this thesis, the problem for swirling turbulent flow through a swirl combustor with cooling air as shown in Fig.1, has been defined. Adding swirl to the flow field turns it into a complex flow possessing several distinctly different flow regimes, either one or two recirculation regions, high levels of turbulence and decay of the core flow emanating from the upstream tube which ultimately causes better mixing. Various methods may be applied for swirl generation. Swirl may be generated by the swirl generator having solid body

rotation, or may be generated with the swirl vane of constant angle at the inlet. The intensity of swirl generation also has different effects on the flow field. Secondary recirculation known as vortex breakdown may occur for sufficiently high swirl strength. The problem of Section 3.2, is analyzed numerically using the present computational code to study the above mentioned effects, and the results presented. In this section, swirl generation by constant vane angle is considered. Here, the tangential velocity is obtained as  $W = U \tan\theta$ . For uniform inlet axial velocity and constant swirl vane angle  $\theta$ , the tangential velocity at inlet before sudden expansion also becomes uniform. The inlet turbulence kinetic energy and dissipation rates are calculated by equation 3.2. Computations are done using a 46X34-size non-uniform grid.

The effect of different swirl vane angles ranging from  $0^0$  to  $66^0$  on flow pattern, mean axial and tangential velocity profiles, turbulent kinetic energy and dissipation rate are studied. The computational results for Case-I, that is  $Q_1:Q_2=1.0$  are shown in figures 8-14, and those for Case-II, that is  $Q_1:Q_2=2.0$  are shown in Figures 15-21.

### 3.4.1 Effect on Swirling Turbulent Flow Pattern:

The effects on the flow pattern i.e. streamline plots for the flow of Fig.1 has been presented in this section. First we would consider the case of constant vane angle swirl generation at inlet for  $Q_1:Q_2= 1.0$  (Case-I), i.e. for  $U_1=15.6$  m/s and  $U_2=15.4$  m/s. with the non swirling jet of 15.4 m/s. The streamline plots for constant swirl vane angles  $\theta = 0^0, 20^0, 37^0, 56^0$  and  $66^0$  corresponding to swirl numbers  $S = 0, 0.25, 0.5, 1.0$  and  $1.5$  are shown in Fig.8. In this figure the stream functions are nondimensionalized by the mass flow rate. The streamline plots for  $Q_1:Q_2=2.0$  (Case-II), i.e. for  $U_1=15.6$  m/s and  $U_2=7.7$  m/s are also plotted in Fig.15, for the above swirl vane angles. For non-swirling flow ( $\theta = 0^0$ ), from Fig.8 and 15 only primary corner recirculation is found near the centerline.

As the vane angle is increased to  $\theta = 20^\circ$ , it can be found from Figs.8 and 15 that the length of the primary corner recirculation decreases for all the cases. This is actually due to the compression of the primary recirculation for sudden expansion by the adverse pressure gradient developing near the centerline for the swirl.

At vane angle  $\theta = 37^\circ$  it can be found from Fig.8 that primary corner recirculation has completely vanished. But for the Case-II, small secondary on axis recirculation is created near the centerline, as shown in Fig.15.

At vane angle  $\theta = 56^\circ$ , large secondary recirculation due to swirl is developed for both cases. This recirculation is clockwise. It grows along the length and tries to remain near the centerline. The secondary recirculation for Case-II is slightly larger than that for Case-I.

As the vane angle is further increased to  $\theta = 66^\circ$ , the on-axis recirculation due to swirl grows bigger as shown in Figs.8 and 15, corresponding to Case-I and Case-II. Comparing these figures it can also be seen that the secondary recirculation moves further to the wall due to smaller non swirling velocity in Case-II.

The swirl strength at which the primary corner recirculation just decays completely that is the transition swirl strength is slightly smaller for Case-II. After this transition swirl strength, only on axis recirculation due to swirl prevails which grows with the increasing swirl strength for both the cases.

### 3.4.2 Effect on Mean Axial Velocity Profiles:

The distribution of the mean axial velocity across the flow for different cases have been presented in this section. For constant vane angle swirl generation at inlet,

mean axial velocity profiles for constant vane angle,  $\theta = 0^\circ, 20^\circ, 37^\circ, 56^\circ$  and  $66^\circ$  corresponding to the swirl number  $S = 0, 0.25, 0.5, 1.0$  and  $1.5$  are considered respectively.

Fig.9 and 16 show the vector diagrams for the axial velocity  $U$  and radial velocity  $V$ , for  $Q_1:Q_2=1.0$  and  $Q_1:Q_2=2.0$  respectively. The velocities have been non-dimensionalized by the reference velocity  $U_0=U_1=15.6$  m/s. For vane angle  $\theta=20^\circ$ , the velocity near the wall in Fig.16 is much smaller than that in Fig.9. The reason is that, for Case-II ( $Q_1:Q_2=2.0$ ) the velocity at inlet for the non swirling cooling air was only 7.7 m/s, compared to 15.4 m/s for Case-I of Fig.9. As a result, inner swirling flow had more chance to expand towards the wall. As the vane angle is further increased to  $37^\circ$  to  $56^\circ$  and  $66^\circ$ , the vector matrix changes rapidly due to swirl strength. An opposite directional vector develops near the axis with low magnitude to indicate the recirculation direction as clockwise.

The distribution of the dimensionless mean axial velocity across the flow for vane angles  $\theta = 0^\circ, 20^\circ, 37^\circ, 56^\circ$  and  $66^\circ$  at different axial locations from inlet are shown in Fig.11 and 18, for Case-I ( $Q_1:Q_2=1.0$ ) and Case-II ( $Q_1:Q_2=2.0$ ), respectively. Here,  $X$  is the distance from the inlet section and  $R$  is the radius of the combustor. For Case-I, at  $X/R = 0.2$  curves for constant swirl vane angle  $\theta = 20^\circ$  and  $37^\circ$  are positive in all the range of  $r/R$ . But for  $\theta = 0^\circ, 56^\circ$  and  $66^\circ$  they are negative when  $r/R$  is in range from 0.0 to 0.3. Vane angle  $\theta = 66^\circ$  move to maximum negative value and also maximum positive value at this ratio. Vane angle  $\theta = 20^\circ$  becomes nearly straight from  $r/R$  ratio of 0.25. In Case-II, at  $\theta = 20^\circ$  the curve is no longer straight, it moves nearly straight from  $r/R=0.2$  ratio to 0.70, but after that it decreases. The other curves also behave in the same fashion and become both negative and positive in magnitude.

At  $X/R = 0.6$  and  $1.0$  for Case-I curves for constant swirl vane angle  $\theta = 20^\circ$  and  $37^\circ$  are positive in all the range of  $r/R$ . But for  $\theta = 0^\circ, 56^\circ$  and  $66^\circ$  they are negative when  $r/R$  is in range from 0.0 to 0.4 except in 1.0 ratio the magnitude

increases. Vane angle  $\theta = 66^\circ$  move to maximum negative value and also at maximum positive value behave like a sine curve. Vane angle  $\theta = 20^\circ$  becomes nearly straight from  $r/R$  ratio 0.20. In Case-II, at  $\theta = 66^\circ$  the curve is no longer straight. The other curves also behave in the same fashion like the curve at  $\theta = 56^\circ$  and remain in both negative and positive magnitude. This difference between the Case-I and Case-II is due to the non swirling jet is reduced to 50% in Case-II.

The more of  $X/R$  ratio increases to 1.50. Vane angle  $66^\circ$  curve shifts radially towards the wall. Because as the ration increases the effect of swirling decays and gives more magnitude near wall due to the vector diagram. In Case-II a sharp change occur at  $r/R$  ratio of 0.75.

At ratio  $X/R = 4.0$ , The velocity pattern changes to a different view. The sharp change at 0.75 diminishes and at  $\theta = 0^\circ$  and  $\theta = 20^\circ$  the curves takes as D shape. This is due to the swirl strength and non-swirling flow. The vector matrix also supports the velocity pattern. In Case-I no negative velocity magnitude appears at this  $X/R$  ratio because swirl strength ceases, so no recirculation due to swirl. It is found that higher vane angles have larger negative portions near the axis supporting larger on-axis recirculation at higher vane angles.

It is observed that curves of constant vane angles  $\theta = 20^\circ, 37^\circ, 56^\circ$  and  $66^\circ$  show tremendous increase in axial velocity near the inclined wall. Constant vane angle swirl generator generates constant azimuthal velocity with respect to radius. To satisfy the mass conservation law, it becomes negative near the axis creating a secondary on axis recirculation. Since this increase in axial velocity is higher near inclined wall for larger swirl vane angles, larger negative portions are associated with larger swirl vane angles. The curve of this swirl vane angle shows positive high axial velocity in the range of  $r/R = 0.2$  to 2.0 confirming to the mass conservation law. Therefore, axial velocity profiles for constant vane angle swirl generation at inlet relate to their corresponding flow patterns with respect to direction and intensity.

### 3.4.3 Effect on Mean Tangential Velocity Profiles:

The distributions of the mean tangential velocity across the flow for different cases have been presented in this section. For constant vane angle swirl generation at inlet, mean tangential velocity profiles for constant vane angle,  $\theta = 0^\circ, 20^\circ, 37^\circ, 56^\circ$  and  $66^\circ$  corresponding to the swirl number  $S = 0, 0.25, 0.5, 1.0$  and  $1.5$  are considered respectively.

Fig.10 and 17 show the vector diagrams for the axial velocity  $U$  and tangential velocity  $W$ , for  $Q_1:Q_2=1.0$  and  $Q_1:Q_2=2.0$  respectively. The velocities have been non-dimensionalized by the reference velocity  $U_0=U_1=15.6$  m/s. For vane angle  $\theta=20^\circ$ , the velocity near the wall in Fig.16 is much smaller than that in Fig.10. The reason is that, for Case-II ( $Q_1:Q_2=2.0$ ) the velocity at inlet for the non swirling cooling air was only 7.7 m/s, compared to 15.4 m/s for Case-I of Fig.9. As a result, inner swirling flow had more chance to expand towards the wall. As the vane angle is further increased to  $37^\circ$  to  $56^\circ$  and  $66^\circ$ , the vector matrix changes rapidly due to swirl strength. The tangential velocity magnitude increased at  $X/R = 1.50$  to  $2.75$ . For Case-II the near wall axial velocity component decreases compared to Case-I. An opposite directional vector develops at the axis with low magnitude to indicate the recirculation direction as clockwise.

The distribution of the dimensionless mean tangential velocity across the flow for vane angles  $\theta = 0^\circ, 20^\circ, 37^\circ, 56^\circ$  and  $66^\circ$  at different axial locations from inlet are shown in Fig.12 and 19, for Case-I ( $Q_1:Q_2=1.0$ ) and Case-II ( $Q_1:Q_2=2.0$ ), respectively. Here,  $X$  is the distance from the inlet section and  $R$  is the radius of the combustor. For Case-I, at  $X/R = 0.2$  curves the tangential velocity becomes maximum at  $r/R$  of 0.78 for vane angle  $\theta = 66^\circ$ . A sharp change is observed at this point, because the magnitude increases proportionately with  $r/R$  ratio and suddenly decreases to 0 magnitude near 0.9 of  $r/R$  ratio. But at no swirl case that is for vane angle  $\theta = 0^\circ$  it rises at the beginning and after that it becomes flat and

decays at 0.78. So the more swirl strength increases the more sharp changes occurs in the curves. This maximum point indicates the maximum friction energy level for the imaginary fluid core and its surrounding. For Case-II, similar behavior observed but in lower magnitude. Curve for  $\theta = 56^\circ$  and  $\theta = 66^\circ$  coincides with one another for Case-I up to the value of 0.20 ratio but a distinction is observed for Case-II due to lower non swirling flow.

At  $X/R = 0.6$  and  $1.0$  for Case-I curves for constant swirl vane angle  $\theta = 20^\circ$  and  $37^\circ$  are nearly same as 0.20 ratio, but for  $\theta = 56^\circ$  and  $66^\circ$  the curve decreased from the pick value as compared to lower  $r/R$  ratio but more sharpness occur for vane angle  $\theta = 56^\circ$ . This is due to the fact that the swirl strength decay with radial distance nearer to the wall where the theoretical rotating fluid core no longer exists.

The more  $X/R$  ratio increases to 1.50 and 2.0 similar curves are found for  $\theta = 20^\circ$ ,  $\theta = 37^\circ$ ,  $\theta = 56^\circ$ , and  $\theta = 66^\circ$  Vane angle. All the curves turn to be linearly increasing with  $r/R$  ratio and at the rotating fluid core periphery it becomes maximum and after that it decreases linearly and moves to zero magnitude for Case-I. In Case-II, it behaves as before except it does not become zero for higher vane angles. So the span of the curves for Case-II increases as compared with the curves of Case-I, which is explained with the vector diagram explanation. At  $X/R = 4.0$  all the curves becomes D shaped with lower magnitude indicating that nearer to the wall tangential velocity is lowest. The tangential velocities in the region near the centerline are much lower than those away from it. The reason is that, the tangential velocity near the centerline has dissipated creating an adverse pressure gradient, which in turn produces the secondary on-axis recirculation due to swirl.

Therefore, tangential velocity profiles for constant vane angle swirl generator at inlet show decrease in velocity at the places in the flow field where secondary recirculation is produced by the adverse pressure gradient through dissipation of tangential velocity.



### 3.4.4 Effect on Turbulence Kinetic Energy:

Higher turbulence kinetic energy gives better mixing which is very important for combustion. So it is the main point of focus of the whole analysis. The turbulence kinetic energy profiles for different swirl intensities are plotted in Figs. 13 and 20 respectively for constant vane angle swirl generation at inlet for Case-I and case-II.

First we would consider the upstream sections  $X/R = 0.2$  in Fig.13. It can be observed that except vane angle for  $0^\circ$  every curve has its two distinct sharp change points at nearly 0.2 and 0.8 of  $r/R$  ratio. It gives the idea about the rotating core fluid and the non-rotating fluid interaction plane where the energy level is maximum due to layer to layer friction. The tangential velocity diagram justifies this also. This higher turbulence kinetic energy generated from the big secondary on axis recirculation growth before the transition swirl strength is achieved. The main difference between Case-I and Case-II is in the magnitude of second rise of the energy level.

At  $X/R = 0.6$ , the initial kinetic energy is increased for all the cases and vane angles. The first sharp change in the energy level becomes smother. The highest kinetic energy level becomes lower to indicate that the non-swirling jet influences the core rotation and also indicating that the secondary recirculation is no longer prevails. The more of  $X/R$  ratio increases, the more first fluctuation in the energy level decay with the initial level because more time the fluid gets to develop a uniform patterns with higher energy level.

For  $X/R$  ratio 1.50 the sharp decrease of energy level as observed for lower  $X/R$  ratios now starts gaining energy and becomes equal to the initial energy level. With higher  $X/R$  ratio the turbulence kinetic energy increases and finally it reaches the maximum level nearly to that point where it was lowest at lower ratios and the value of the turbulence kinetic energy level is higher for Case-I.

Therefore, turbulence kinetic energy is found to be higher for Case-I at any particular swirl strength after the transition swirl strength (post-transition swirl strength). It remains almost same at any pre-transition swirl strength for all cases.

### 3.4.5 Effect on Turbulence Dissipation Rate:

Turbulence dissipation rate profiles show similarity in their shapes with turbulence kinetic energy profiles. Turbulence dissipation rate profiles are plotted for all the cases and  $X/R$  ratios having constant vane angle swirl generation at inlet in Figs. 14 and 21 respectively for Case-I and Case-II. It is observed at sections  $X/R = 0.2, 0.6, 1.0, 1.5, 2.0$  and  $4.0$  that the intensities of the turbulence dissipation rate are lower than those of the turbulence kinetic energy for all the swirl strengths. But at section  $X/R = 0.2$ , the intensities of the turbulence dissipation rate are found to be higher than those of the turbulence kinetic energy for all the swirl strengths. For Case-II all the dissipation rate are lower as we compared these to Case-I. This is due to the fact that lower turbulence kinetic energy is observed for Case-II.

## 3.5 EFFECT OF SOLID BODY ROTATION SWIRL GENERATION

In this section swirl generated by solid body rotation is considered. The intensity of swirl generation also has different effects on the flow field. Secondary

recirculation known as vortex breakdown may occur for sufficiently high swirl strength. The problem of Section 3.2, is analyzed numerically using the present computational code to study the above mentioned effects, and the results presented. Here, the tangential velocity varies linearly with radius. For uniform inlet axial velocity and solid body rotation, the tangential velocity at inlet before sudden expansion also becomes uniform. The inlet turbulence kinetic energy and dissipation rate are calculated by equation 3.2. Computations are done using a 46X34-size non-uniform grid.

The effect of different swirl strength ranging from 0.25 to 1.5 on flow pattern, mean axial and tangential velocity profiles, turbulent kinetic energy and dissipation rate are studied. The computational results for Case-I, that is  $Q_1:Q_2=1.0$  are shown in figures 25-28, and those for Case-II, that is  $Q_1:Q_2=2.0$  are shown in Figures 32-35.

### 3.5.1 Effect on Swirling Turbulent Flow Pattern:

We would consider now the case of solid body rotation swirl generation at inlet, which is a forced vortex generator type. The streamline plots for different swirl intensities are plotted in Figs. 22 and 29 respectively for Case-I and Case-II. In Figs. 22 and 29 the stream functions are nondimensionalized by the mass flow rate. For low swirl strength of  $S = 0.25$ , from Figure only primary corner recirculation is found like that of constant vane angle swirl generation at inlet for both the cases. Comparing these cases for  $S = 0.50$ , it is observed that the size of the primary recirculation is almost same. The small clockwise rotating flow within this primary recirculation is observed for both the cases.

As the swirl strength is increased to  $S = 0.75$ , it is found from Figure that length of the primary corner recirculation decreases to zero level and a secondary on axis recirculation due to swirl develops. This secondary on axis recirculation is

found to be located downstream to the reattachment point of the primary recirculation.

As the swirl strength is further increased to  $S = 1.00$ , it is found that the secondary on axis recirculation has grown bigger and has a tendency to form off axis recirculation. The on axis recirculation are found to be located downstream to the reattachment point of the primary corner recirculation. The reason for this is that, with the increase of swirl strength tangential velocity increases and centrifugal force due to this swirl compresses the primary recirculation. On axis recirculation becomes off axis recirculation because the mass of fluid shifts from the axis outwards due to swirl and solid body rotation swirl generator produces swirl linearly proportional to the radius.

Since near swirl strength  $S = 1.50$  primary recirculation just completely vanishes, this swirl strength is referred to as transition swirl strength under solid body rotation swirl generation at inlet. This flow phenomenon is found because higher tangential velocity component of this higher swirl strength dissipates to create higher adverse pressure gradient, which overcomes the positive pressure gradient.

Solid body rotation swirl generator at inlet generates the same trend of flow pattern as the constant vane angle swirl generator at inlet. But higher complexities are associated with the solid body rotation swirl generation than the constant vane angle swirl generation at inlet. Considerable secondary recirculation is found for  $S \geq 1.0$ . For Case-II, inner swirling flow penetrates to the wall surface faster than for Case-I, which can be determined by comparing Fig. 10, 24 and 17 and 31.

### 3.5.2 Effect on Mean Axial Velocity Profiles:

The distribution of the mean axial velocity across the flow for different cases have been presented in this section. For solid body rotation swirl generator at inlet, mean axial velocity profiles for swirl number  $S = 0.25, 0.50, 0.75, 1.00$  and  $1.50$  are considered respectively.

From Figs.16 and 30 the vector distribution of Case-II can be observed for axial velocity combination for  $U_0$  and non-swirling inlet jet  $U_2$ . For swirl number  $0.25$ , the vector velocity profiles changes more rapidly in Case-II. As the vector moves towards the wall it's magnitude decreases sharply for  $U_2=7.7$  m/s, but at  $U_2=15.4$  m/s (from Figs.9 and 23) it gains some amount of axial velocity so the magnitude near to the wall is more compare to the center axis, As the swirl number is further increased to  $0.50$  to  $0.75$  and  $1.00$ , the vector matrix changes rapidly due to swirl strength. An opposite directional vector develops at the axis with low magnitude to indicate the recirculation direction as clockwise.

For Case-I, at  $X/R = 0.2$  curves for solid body rotation swirl generator are positive in the range of  $0.20$  to  $1.0$  of  $r/R$  ratio. But at the beginning the curve is in negative domain except for Swirl number  $S= 0.75$ . In Case-I all the curves first increases and after a certain point they nearly becomes flat. The maximum magnitude is near  $0.78$  of  $r/R$  ratio. Swirl number  $S= 0.50$  and  $0.75$  followed the same track like swirl number  $S=0.25$ . For Case-II the situation is different due to the effect of reduction in non-swirling jet velocity. All the curves first increases up to a limit and continue to move nearly unaltered and again they decline and move straight.

At  $X/R = 0.6$  changes are found in all the curves. All of them shift from the negative value towards the positive values and also their initial magnitude of axial velocity increases. Swirl number  $S = 1.50$  gets the maximum value and it stays for longer period in negative part with  $r/R$  ratio. But the initial sharp change to the negative maximum value becomes smooth. For Case-II, all the curves behave as

same as before but the peak value for  $S = 1.50$  increases due to shifting to the theoretical rotating fluid core.

For  $X/R = 1.0$  and  $1.5$  for Case-I curves starts moving towards the positive level with increased magnitude values because the secondary recirculation is no longer exists for causing the pressure gradient to give rise to the tangential velocity component. In Case-II, all the curves followed the same pattern like lower ratio with higher values near the wall, because of inlet non-swirling jet.

When the ratio of  $r/R$  gets its maximum value from  $2.0$  to  $4.0$  that is very close to the wall all the curves shifts from the negative values to the positive value. The curve for  $S = 0.50$  and  $0.75$  are no longer coincides with the curve at  $S = 0.25$ . But the maximum magnitude for the  $S = 1.50$  decreased from the value that was obtained at  $r/R$  ratio of  $2.0$ . In Case-II, as on the wall the axial velocity is zero so the change is found for the case of all the curves because they increased up to a maximum level with lower slope and declines even with higher slope, thus the end value for  $S = 1.50$  is less from the starting magnitude of axial velocity.

### 3.5.3 Effect on Mean Tangential Velocity Profiles:

Let us now consider the tangential velocity profiles having solid body rotation swirl generation at inlet at different swirl intensities are plotted in Figs. 26 and 33 respectively.

The distributions of the mean tangential velocity across the flow for different cases have been presented in this section. For solid body rotation swirl generator at inlet, mean tangential velocity profiles for swirl number  $S = 0.25, 0.50, 1.00$  and  $1.50$  are considered.

From Figs.17 and 31 the vector distribution of Case-I and Case-II can be observed for tangential velocity combination for  $U_0$  and non swirling inlet jet  $V$ . For swirl number  $S = 0.25$ , the vector velocity profiles changes more rapidly in Case-II. As the vector moves towards the wall it's magnitude decreases sharply for  $U_2=7.7\text{m/s}$ , but at  $U_2=15.4\text{m/s}$  it gains some amount of tangential velocity so the magnitude near to the wall is more compare to the center axis. As the swirl strength is further increased to  $S = 0.50$  to  $S= 1.00$  and  $S =1.50$ . the vector matrix changes rapidly due to swirl strength. The tangential velocity magnitude increased at  $X/R = 1.50$  to  $2.75$ . For Case-II the near wall axial velocity component decreased compared to Case-I. An opposite directional vector develops at the axis with low magnitude to indicate the recirculation direction as clockwise.

For Case-I, at  $X/R = 0.2$  curves the tangential velocity becomes maximum at  $0.75$  of  $r/R$  ratio for  $S = 1.50$ . A sharp change is observed at this point, because the magnitude increases proportionately with  $r/R$  ratio and suddenly decreased to  $0$  magnitude near  $0.85$  of  $r/R$  ratio. But at no swirl case that is for swirl number  $S = 0.25$ . It rises at the beginning and after that it becomes flat and decays at  $0.78$  of the ratio. So the more swirl strength increases the more sharp changes occurs it the curves. This maximum point indicates the maximum friction energy level for the imaginary fluid core and its surrounding. For Case-II, similar behavior observed but in lower magnitude. Curve for  $S = 1.00$  and  $S = 1.50$  no longer coincides with one another as in the case of constant vane angle for Case-I up to  $0.20$  ratio but a distinction is observed for Case-II due to lower non swirling flow.

At  $X/R = 0.6$  and  $1.0$  for Case-I curves for  $S = 0.25$  and  $S = 0.50$  are nearly same as  $0.20$  ratio, but for  $S = 1.00$  and  $1.50$  the curve decreased form the pick value as compared to lower  $r/R$  ratio but more sharpness occur for vane angle  $S = 1.50$ . This is due to fact the swirl strength decay with radial distance nearer to the wall where the theoretical rotating fluid core no longer exists.

The more  $X/R$  ratio increases to  $1.50$  and  $2.0$  similar curves are found for  $S = 0.25$ ,  $S = 0.50$ ,  $S = 1.00$ , and  $S = 1.50$  swirl number. All the curves turn to be

linearly increasing with  $r/R$  ratio and at the rotating fluid core periphery it becomes maximum and after that it decreases linearly and moves to zero magnitude for Case-I. In Case-II, it behaves as before except it does not become zero for higher vane angles. So the span of the curves for Case-II increases as compared with the curves of Case-I, which is explained with the vector diagram explanation. At  $X/R = 4.0$  all the curves becomes D shaped with lower magnitude indicating that nearer to the wall tangential velocity is lowest. The tangential velocities in the region near the centerline are much lower than those away from it. The reason is that, the tangential velocity near the centerline has dissipated creating an adverse pressure gradient, which in turn produces the secondary on-axis recirculation due to swirl.

Therefore, tangential velocity profiles for solid body swirl generator at inlet show decrease in velocity at the places in the flow field where secondary recirculation is produced by the adverse pressure gradient through dissipation of tangential velocity.

### 3.5.4 Effect on Turbulence Kinetic Energy:

If the turbulence kinetic is higher it better mixing which is very important for combustor design. It is the vital point of focus of the whole analysis. The turbulence kinetic energy profiles for different swirl intensities are plotted in Fig.27 and 34 respectively for solid body rotation swirl generation at inlet.

First we would consider the upstream sections  $X/R = 0.2$  in Figs. 27a. It can be observed that every curve has its one distinct sharp change points at nearly 0.8 of  $r/R$  ratio. It gives the idea about the rotating core fluid and the non-rotating fluid interaction plane where the energy level is at maximum due to layer to layer friction. The tangential velocity diagram justifies this also. This higher turbulence



kinetic energy generated from the big secondary on axis recirculation growth before the transition swirl strength is achieved. The main difference between Case-I and Case-II is in the magnitude of second Rise of the energy level.

At  $X/R = 0.6$ , the initial kinetic energy is increased for all the cases and swirl numbers. There is an initial rise for all the curves but it decays with increase of  $r/R$  ratio. The energy level becomes lower to indicate that the non-swirling jet influences the core rotation and also indicating that the secondary recirculation is no longer prevails. The more of  $X/R$  ratio increases the more fluctuation in the energy level decay with the initial level because more time the fluid gets to develop a uniform patterns with higher energy level.

For  $X/R$  ratio of 1.50 the sharp decrease of energy level as observed for lower  $X/R$  ratios now starts gaining energy and becomes equal to the initial energy level. With higher  $X/R$  ratio the turbulence kinetic energy increases and finally it reaches the maximum level nearly to that point where it was lowest at lower ratios and the value of the turbulence kinetic energy level is higher for Case-I.

Therefore, turbulence kinetic energy is found to be higher for Case-I at any particular swirl strength after the transition swirl strength (post-transition swirl strength). It remains almost same at any pre-transition swirl strength for all cases. So, turbulence kinetic energy is found to be very low at the transition swirl strength. Constant vane angle swirl generator is found to produce higher turbulence kinetic energy when compared to solid body rotation swirl generator at inlet. Rate of mixing increases with the increase of turbulence kinetic energy. Increased rate of mixing gives higher combustion efficiency and thereby low fuel cost.

### 3.5.5 Effect On Turbulence Dissipation Rate:

Turbulence dissipation rate profiles are plotted for all the swirl number considered having solid body rotation swirl generation at inlet in Figs. 28 and 35. Turbulence dissipation rate profiles show similarity in their shapes with turbulence kinetic energy profiles. It is observed at sections for  $X/R = 0.2, 0.6, 1.0, 1.5, 2.0$  and  $4.0$  that the intensities of the turbulence dissipation rate are lower than those of the turbulence kinetic energy for all the swirl strengths. But at section  $X/R = 0.2$ , the intensities of the turbulence dissipation rate are found to be higher than those of the turbulence kinetic energy for all the swirl strengths. For Case-II all the dissipation rate are lower as we compared these to Case-I. This is due to the fact that lower turbulence kinetic energy is observed for Case-II.

## 3.6 CLOSURE

The present computer code is used to simulate the swirling turbulent flow for different swirl generator and non swirling inlet jet velocity. To verify the validity of the computer code the predicted results are first compared with the available experimental data and found to have reasonably good matching. The flow is then studied for different swirl strength with constant vane angle swirl generator and solid body swirl generator at the inlet. A stable non-uniform grid size  $46 \times 34$  is used in the present numerical simulation.

# Chapter – 4

## CONCLUSION

In this chapter, the main findings of the present computational study are summarized and some suggestions for future work have been made.

### 4.1 SUMMARY OF MAIN FINDINGS

The results of this thesis have been presented in the previous chapter. Based on those results the following conclusions may be drawn:

- i. The present computational model is capable of predicting complex flows like swirling turbulent flow having various types of swirl generator and non-swirling or cooling inlet jets with reasonable accuracy.
- ii. The change in swirl strength and types of swirl generator has significant effect on flow patterns, axial velocity, tangential velocity, turbulence kinetic energy and turbulence dissipation rate of the flow field after expansion in the outer tube as described in the experimental setup boundary level. Transition swirl strength is defined to be the swirl strength at which primary corner recirculation just completely vanishes. The lower the swirl strength, the lower the transition swirl strength. The trend of growth of different types of flow pattern is observed to be similar at all the cases. Two case considered in this study, Case-I and case-II depending on the inlet non swirling jet velocity 15.4 m/s and 7.7 m/s. Turbulence kinetic energy becomes very low at the transition swirl strength. The higher the X/R ratio higher the higher the turbulence kinetic

energy at any particular swirl strength after the transition swirl strength of the corresponding swirl case.

- iii. The method of swirl generation at inlet plays an important role on the distribution of fluid flow properties after expansion. Constant vane angle swirl generator, at inlet it generates only primary corner recirculation at low swirl strengths, primary corner and secondary on-axis recirculation at moderate swirl strengths becomes transition swirl strength. Solid body rotation swirl generator generates only primary corner recirculation at very low swirl strengths, primary corner and secondary on-axis recirculation at low swirl strengths, primary corner and secondary off-axis recirculation at moderate swirl strengths before the transition swirl strength, only secondary off-axis recirculation at moderate swirl strengths after the transition swirl strength, and secondary on-axis recirculation at high swirl strengths. Much higher turbulence kinetic energy is generated by constant vane angle swirl generator than solid body rotation swirl generator at inlet for the same swirl strength. Comparing the Fig. 8 and 22 and also Fig.9 and 23 it can be concluded that recirculation for constant vane angle is greater than that of solid body rotation thus the mixing will be better with constant vane angle swirl generation at inlet. Again by comparing Fig.8 and 15 and also 22 and 29 it is clear that secondary recirculation for Case-II is greater than that of Case-I.
- iv. Tangential velocity dissipates to create adverse pressure gradient, which in turn produces the secondary on-axis or off-axis recirculation. Tangential velocity profiles show decrease in velocity at the places in the flow field where secondary recirculation is produced by the adverse pressure gradient through dissipation of tangential velocity.

## 4.2 SUGGESTIONS FOR FUTURE WORK

The following works can be done in future:

1. Effect of non-swirling inlet jet flow through the blocked section can be employed with non-uniform or asymmetric cross section.
2. Higher order schemes can be used to have better accuracy of predictions.
3. More sophisticated turbulence model can be employed.
4. Transport equation for temperature can be added.

## REFERENCES

1. Ahmed SA, "Velocity measurements and turbulence statistics of a confined Isothermal swirling flow", *Experimental Thermal and Fluid Science*, Vol.17, No.3, pp. 256-264. [Jul 1998].
2. Ahmadi, G. and Chowdhury, S.J., "A Rate-Dependent Algebraic Stress Model for Turbulence", *J. Appl. Math. Modeling*, 15, 516-524 [1991].
3. Amano, R.S., "A Study of Turbulent Flow Downstream of an Abrupt Pipe Expansion", *J. AIAA*, 21, 1400-1405 [1983].
4. Bradshaw, P., Cebeci, T. and Whitelaw, J.H., "Engineering Calculation Methods for Turbulent Flow", Academic Press, New York [1981].
5. Chowdhury, S.J., "Thermodynamically Consistent Rate-Dependent Models for Turbulence", "Ph.D. Thesis, Clarkson University, New York, USA [1990].
6. Daley, R.J. and Harlow, F.H., "Transport Equation in Turbulence", *Phys. Fluids* 13, 2634 [1970].
7. Das, R.N., "Numerical Study of Coaxial Turbulent Jets with Sudden Axisymmetric Expansion", M.Sc. Thesis, BUET, Dhaka, Bangladesh [1992].
8. Donaldson, C., "Calculation of Turbulent Shear Flows for Atmospheric and Vortex Motion", *AIAA J.* 10, pp. 4-12 [1972].
9. Hanjalic, K. and Launder, B.E., "A Reynolds Stress Model of Turbulence and its Application to Thin Shear Layer", *J. Fluid Mech.* 52, 609 [1972].

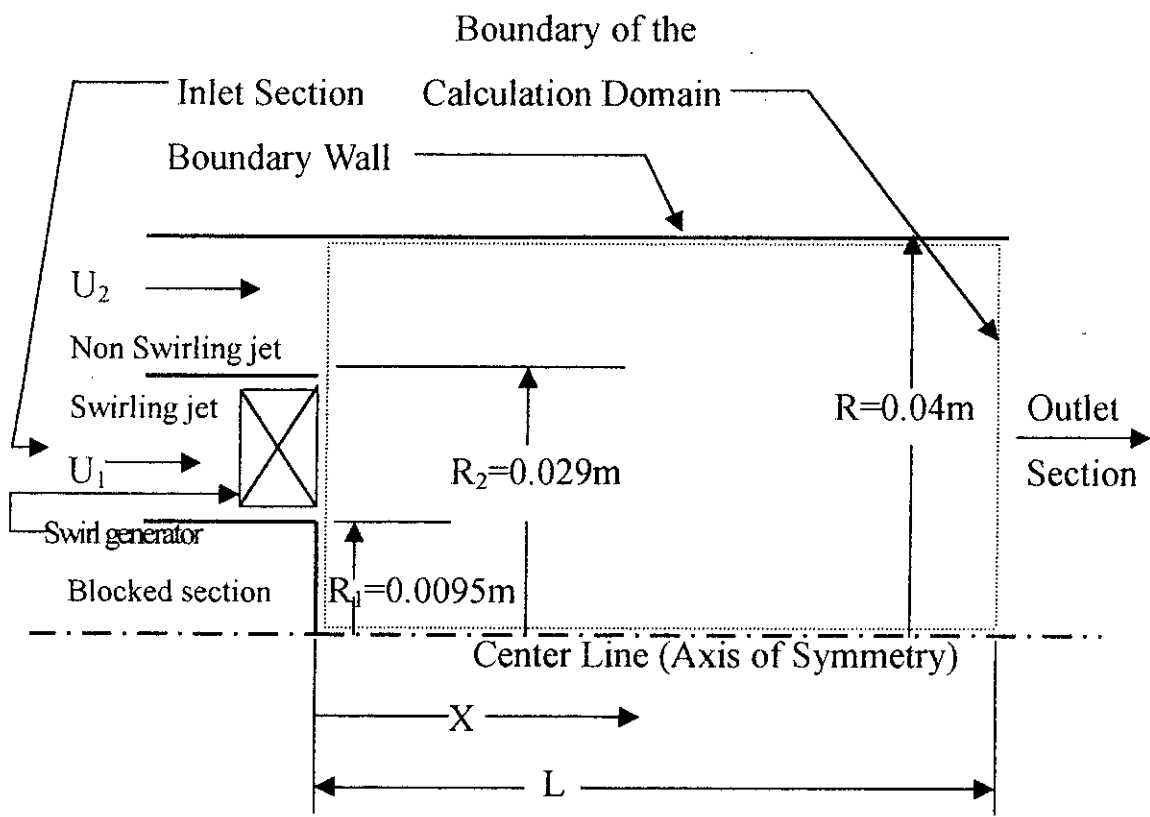
10. Hsu AT, Anand MS, Razdan MK, "Calculation of a premixed swirl combustor using the PDF method", American Society of Mechanical Engineers (Paper), p.10p.[ 1997].
11. Hogg, S. and Leschziner, M.A., "Computation of Highly Swirling Confined Flow with a Reynolds Stress Turbulence Model", J. AIAA, Vol. 27, No. 1, p. 57-63 [1989].
12. Jones, W.P. and Launder, B.E., "The Prediction of Laminarization with a Two Equation Model of Turbulence", Int. J. Heat and Mass Transfer 15, 301-314 [1972].
13. Jones, W.P. and Launder, B.E., "The Calculation of Low Reynolds Number Phenomena with a Two-equation Model of Turbulence", Int. J. Heat and Mass Transfer 16, 1119-1130 [1973].
14. Launder, B.E. and Spalding, D.B., "Mathematical Models of Turbulence". Academic Press, New York [1972].
15. Launder, B.E. and Spalding, D.B., "Turbulence Models and their Applications to the Prediction of Internal Flows", Heat Fluid Flow, 2, 43-54 [1972].
16. Launder, B.E., Recce, G.J. and Rodi, W., "Progress in the Development of a Reynolds Stress Turbulence Closure", J. Fluid Mech., 68, 537 [1975].
17. Lumley, J.L., "Toward a Turbulence Constitutive Relation", J. fluid Mech. 41, pp.413-434 [1970].
18. Lumley, J.L. and Khajeh-Nouri, B., "Computation of Turbulent Transport". Advances in Geophysics A18, 169-192 [1974].
19. Lumley, J.L., "Turbulence Modeling", J. Appl. Mech., Trans, ASME 50, pp. 1097-1103 [1983].

20. Nallasamy, M., "Turbulence Models and Their Applications to the Prediction of Internal Flows", A Review Pergamon Journals Ltd., Vol. 15, No. 2. p. 151-194 [1987].
21. Park TW, Roquemore WM, Katta VR, Aggarwal SK, "Numerical study of two-phase flow field in a simplified swirl cup combustor", American Society of Mechanical Engineers, Fluids Engineering Division (Publication) FED. Vol.244. pp.215-223. [1997].
22. Pasini S, Coghe A, Ghezzi U, Solero G, "Experimental characterization of flows in the model of a strongly swirling combustor", Proceedings of the Intersociety Energy Conversion Engineering Conference, Vol.2, pp.916-920. [1997].
23. Prandtl, L., ZAMM, 5, 136 [1925].
24. Reynolds, W.C., "Annual Review of Fluid Mechanics", Vol. 8, ed, M. VanDyke, Wehausen, V. and Lumley, J. L. Palo Alto, p. 183, CA [1976].
25. Rodi, W., "A New Algebraic for Calculating the Reynolds Stresses", ZAMM. 56, T219-T221 [1976].
26. Rodi, W., "Examples of Turbulence Models for Incompressible Flow", AIAA J. 20, pp. 872-889 [1982].
27. Sanger JL, Dellenback PA, "Heat transfer in counters-whirled coaxial jet mixing", Journal of Propulsion and Power, Vol.14, No.3, pp.384-391, [May-Jun 1998].
28. Sanghi, S. and Aubry, N., "Mode Interaction Models for Near Wall Turbulence", J. Fluid Mechanics, p. 455-488 [1993].
29. Sajjad Mayeed M., "Numerical study of the effect of Expansion angles on turbulent swirling flow", M.Sc. Thesis, BUET, Dhaka, Bangladesh [1997].



30. Shtilman, L., Spector, M. and Tsinober, "On Some Kinematics Versus Dynamic Properties of Homogeneous Turbulence", *J. Fluid Mechanics*, p. 65-77 [1993].
31. Smirnov A, Lipatnikov A, Chomiak J., "Some aspects of turbulence and combustion modeling of swirl-stabilized LPP combustion", *American Society of Mechanical Engineers, Internal Combustion Engine Division (Publication) ICE*, Vol.31, No.2, pp. 37-46, [1998].
32. Spalding, D.B., *Turbulence Models, a Lecture Course*, Imperial College of Science and Technology [1982].
33. Su A, Chang JH, Ho WC, "Numerical simulations of coal-fired swirl rectangular combustor", *American Society of Mechanical Engineers, Heat Transfer Division. (Publication) HTD*, Vol.357-2, pp. 85-92, [1998].
34. Tennekes, H. and Lumley, J.L., "A First Course in Turbulence", MIT Press. Cambridge [1972].
35. Tsao JM, Lin CA., "Reynolds stress modelling of jet and swirl interaction inside a gas turbine combustor", *International Journal for Numerical Methods in Fluids*, Vol.29, No.4, pp. 451-464, [Feb 28 1999].
36. Yoshizawa. A., "Statistical Analysis of the Derivation of the Reynolds Stress from its Eddy Viscosity Representation", *Phys. Fluids* 27, 1 377-1387 [1984].
37. Yoshizawa, A., "A Statistically Derived System of Equations for Turbulent Shear Flows", *Phys. Fluids* 28, 59-63 [1985].
38. Zeman, O., "Annual Review of Fluid Mechanics", Vol. 13, ed. VanDyke. M. Wehausen V. and Lumley J. L. Palo Alto, CA [1981].
39. Joarder, M.A.S., "Numerical Study of Swirling Turbulent Flow through an Abrupt Expansion", M.Sc. Thesis, BUET, Dhaka, Bangladesh [1994].

40. Xia JL, Smith BL, Benim AC, Schmidli J, Yadigaroglu G." Effect of inlet and outlet boundary conditions on swirling flows". Computers & Fluids. Vol.26. No.8. pp.811-823. [Nov 1997].



$U_1=U_0=15.6 \text{ m/s}$  (Fixed)

$U_2=15.4 \text{ m/s}$  for Case-I

$U_2=7.7 \text{ m/s}$  for Case-II

FIG.1. Geometry of confined swirling jet experimental setup for Brum and Samulsen.

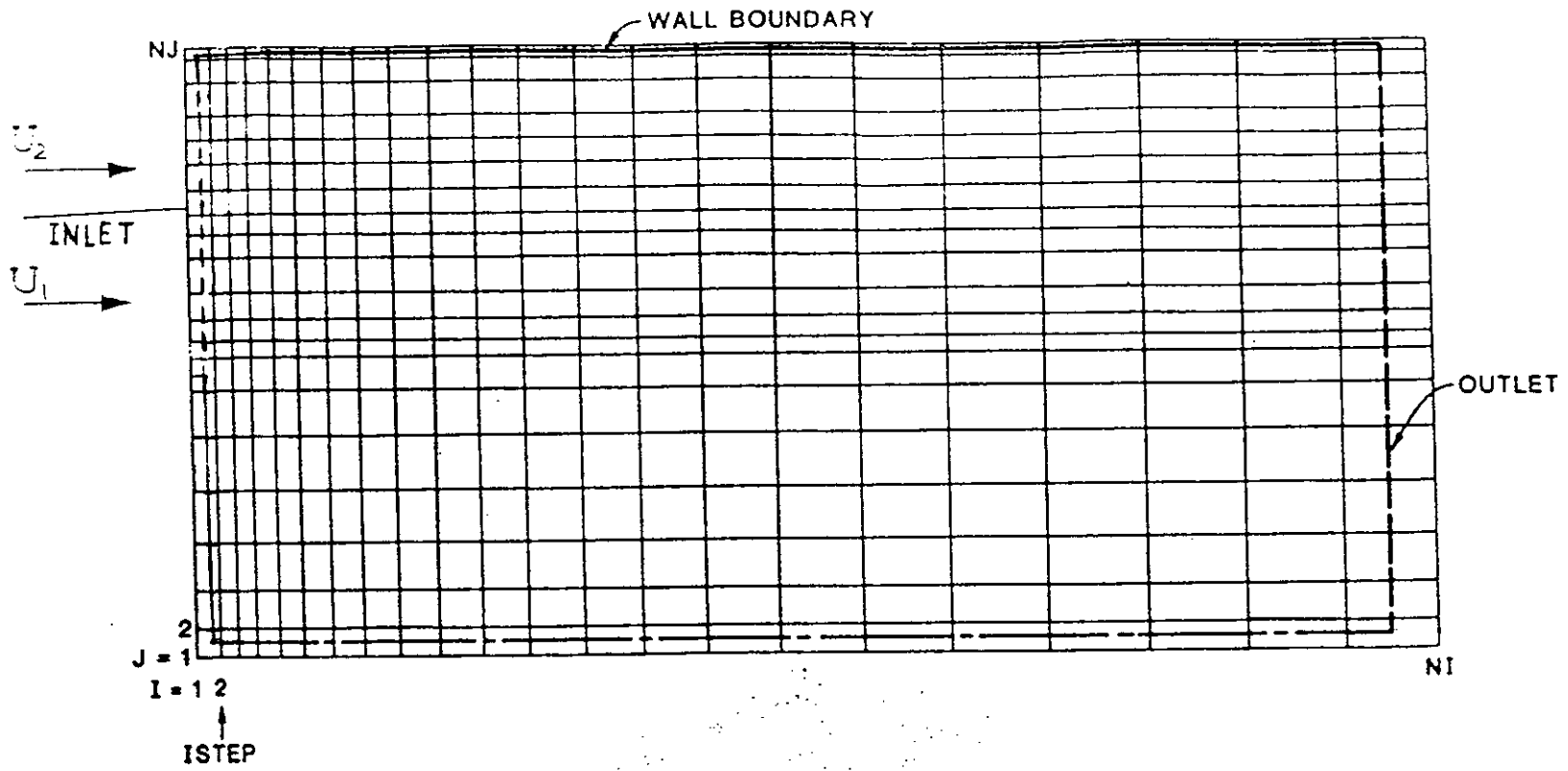


FIG.2 Non uniform Staggered grid.

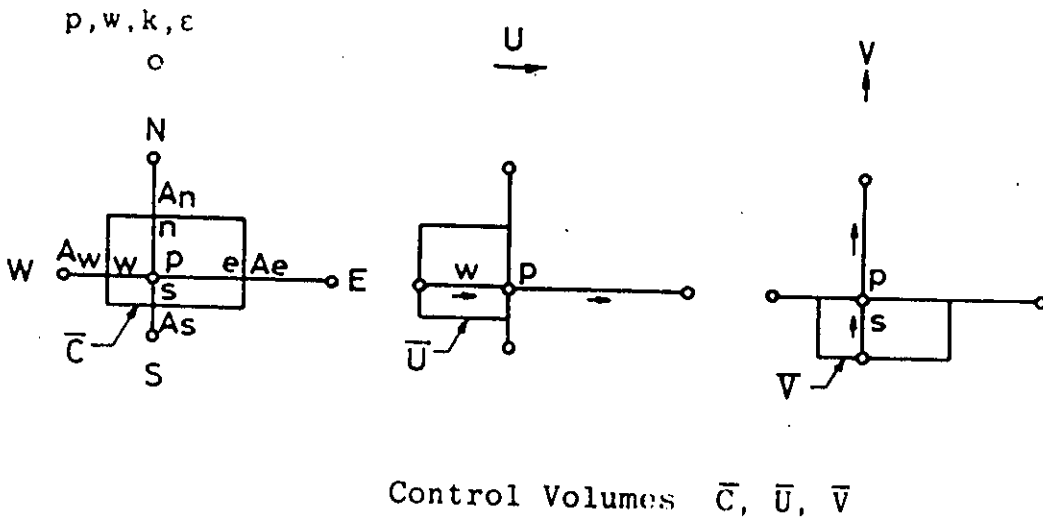
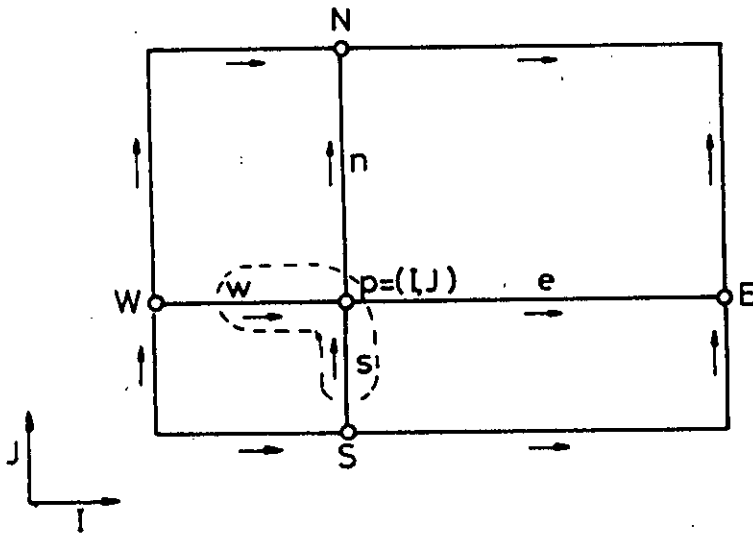


FIG.3. Three control volumes associated with points of the three grids.



Three Grids: For  $p, w, k, \epsilon$  -- At Position Marked (o)  
 For U Velocity -- At Position Marked ( $\rightarrow$ )  
 For V Velocity -- At Position Marked ( $\uparrow$ )

FIG.4. Nonuniform grid system employed to fit the flow domain

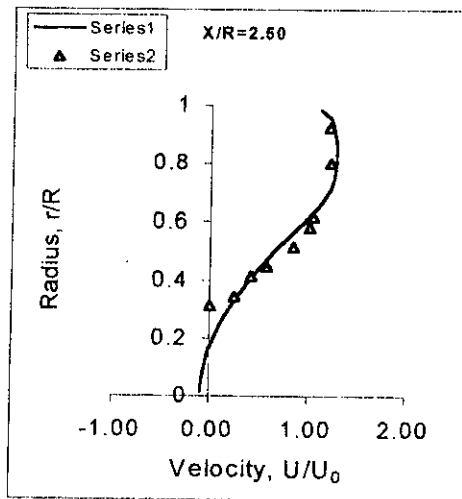
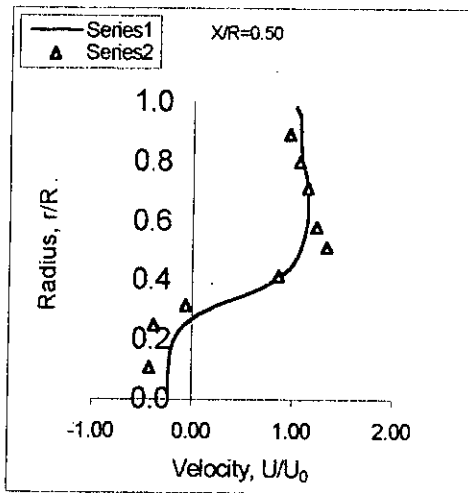
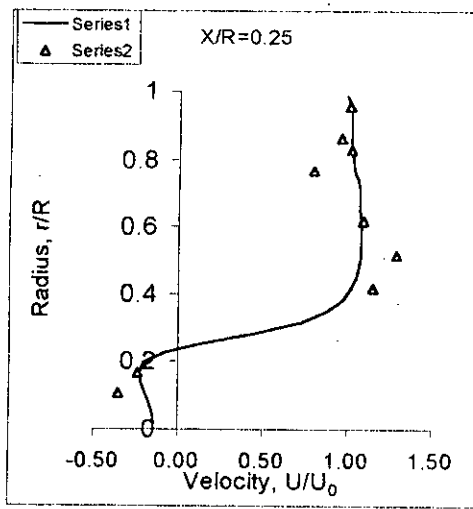


FIG. 5. Comparison of computed dimensionless mean axial velocity profiles with experimental data. (Series-1 is from numerical prediction and Series- 2 is from Brum and Samuelsen experimental data)

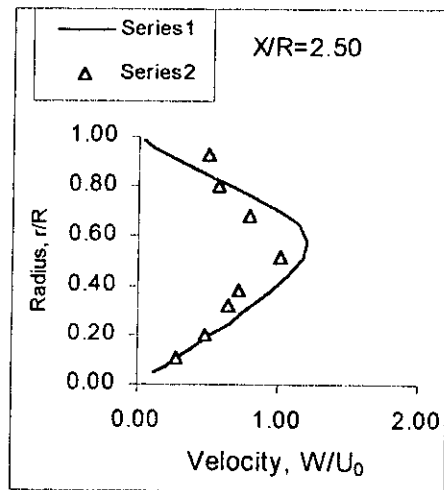
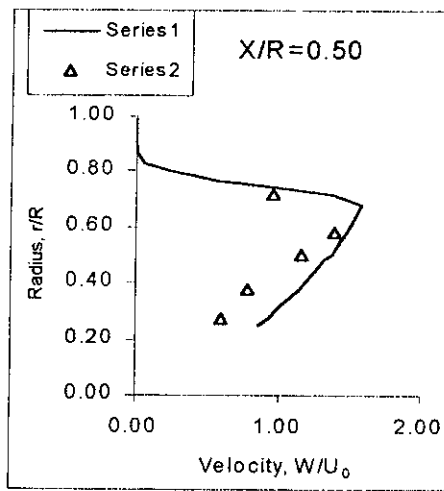
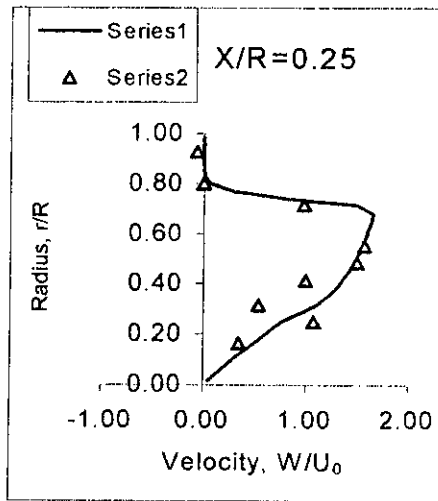


FIG. 6. Comparison of computed dimensionless mean tangential velocity profiles with experimental data. (Series-1 is from numerical prediction and Series- 2 is from Brum and Samuelsen experimental data)

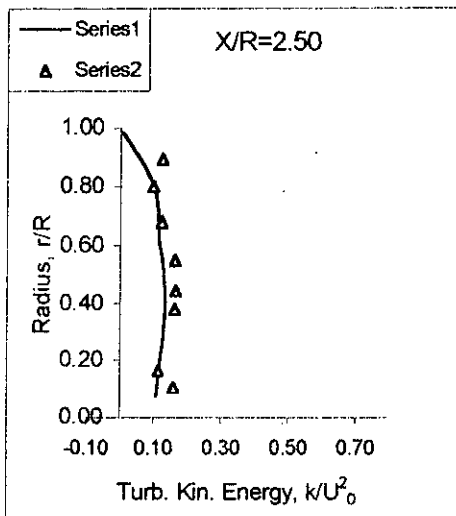
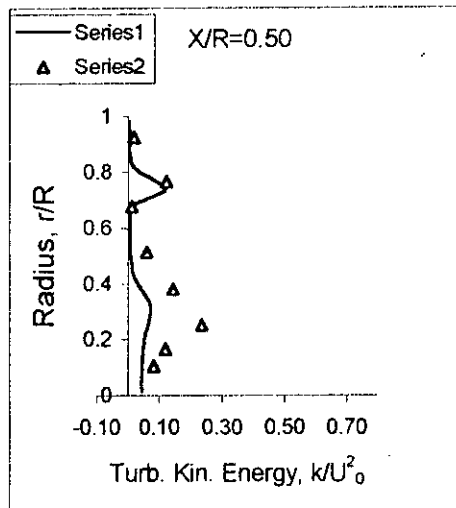
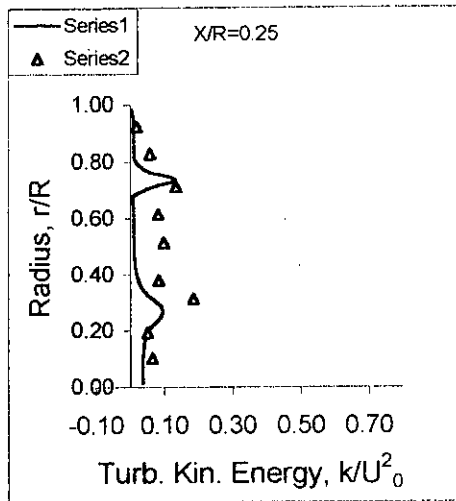


FIG.7. Comparison of computed dimensionless turbulence kinetic energy profiles with experimental data. (Series-1 is from numerical prediction and Series- 2 is from Brum and Samuelsen experimental data)



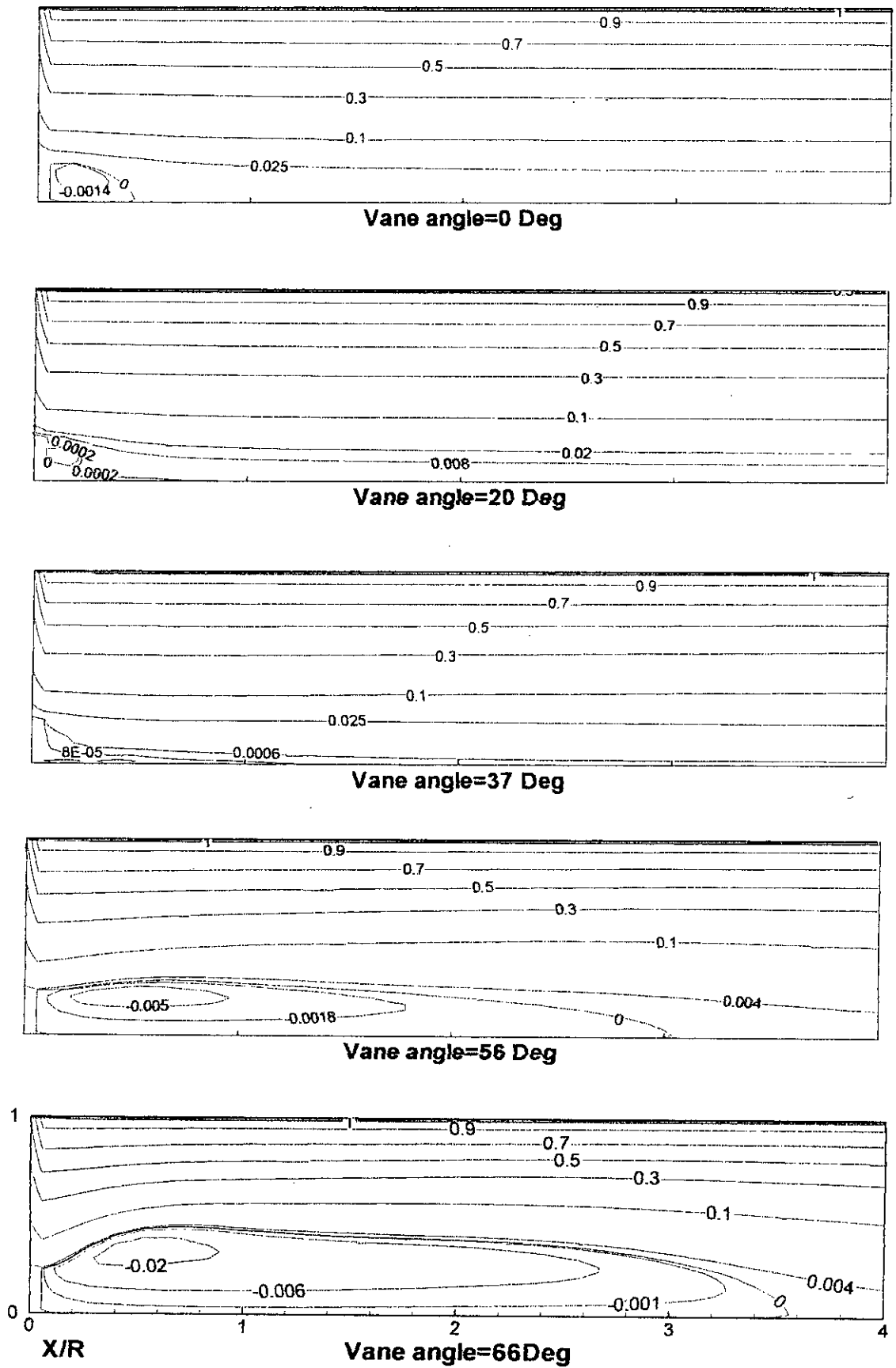
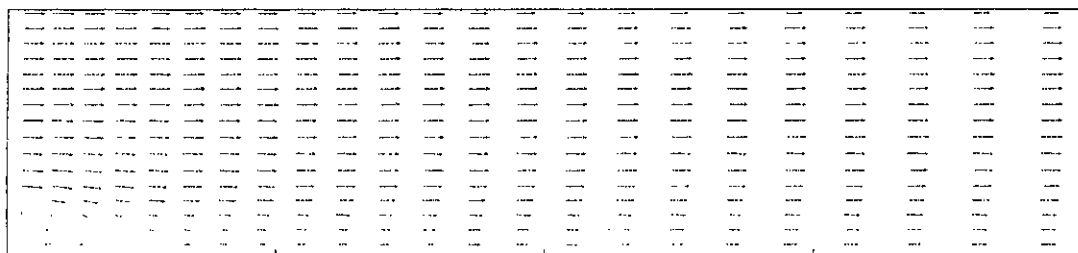
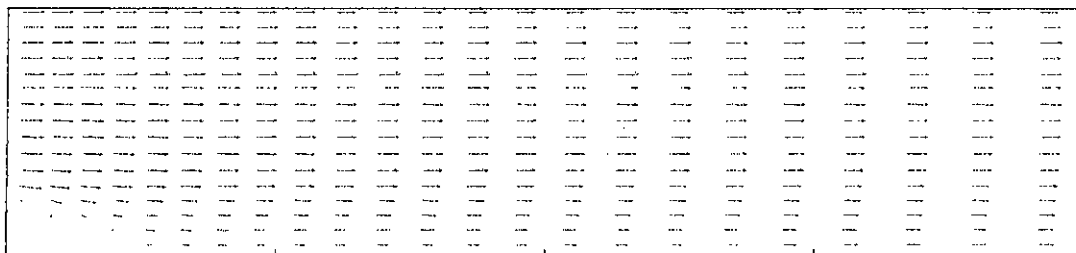


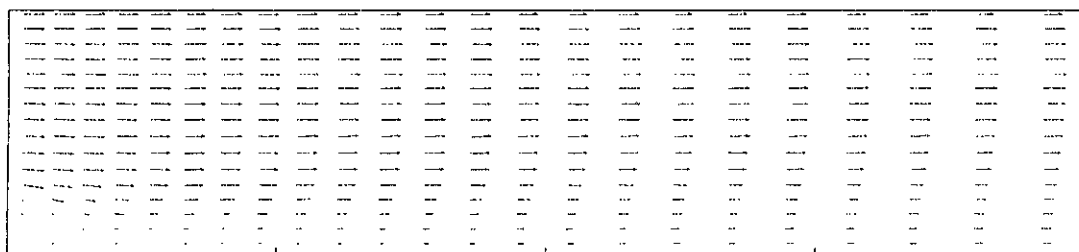
Fig. 8. Streamline plots for constant vane angle swirl generator at inlet for Case-I.



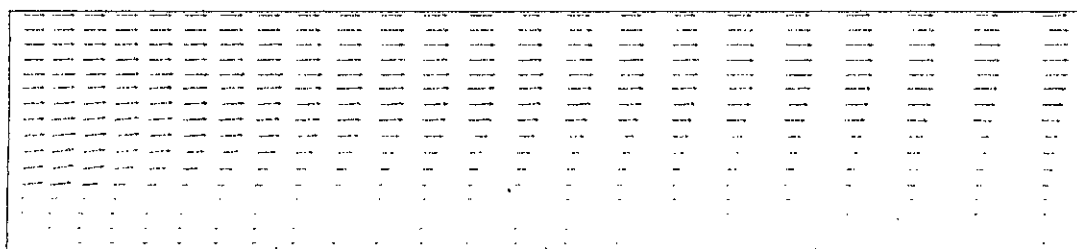
**Vane angle=0 Deg**



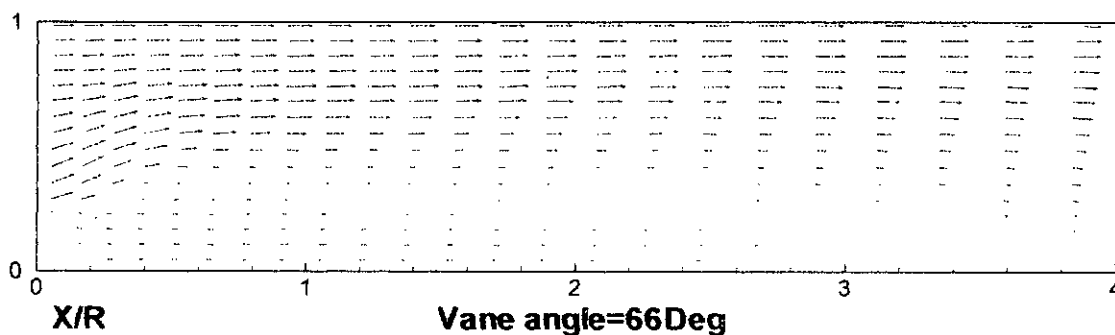
**Vane angle=20 Deg**



**Vane angle=37 Deg**



**Vane angle=56 Deg**



**Vane angle=66 Deg**

FIG.9. Comparison of vector Diagram for combined axial and radial velocities at inlet for constant vane angle swirl generator for Case-I.

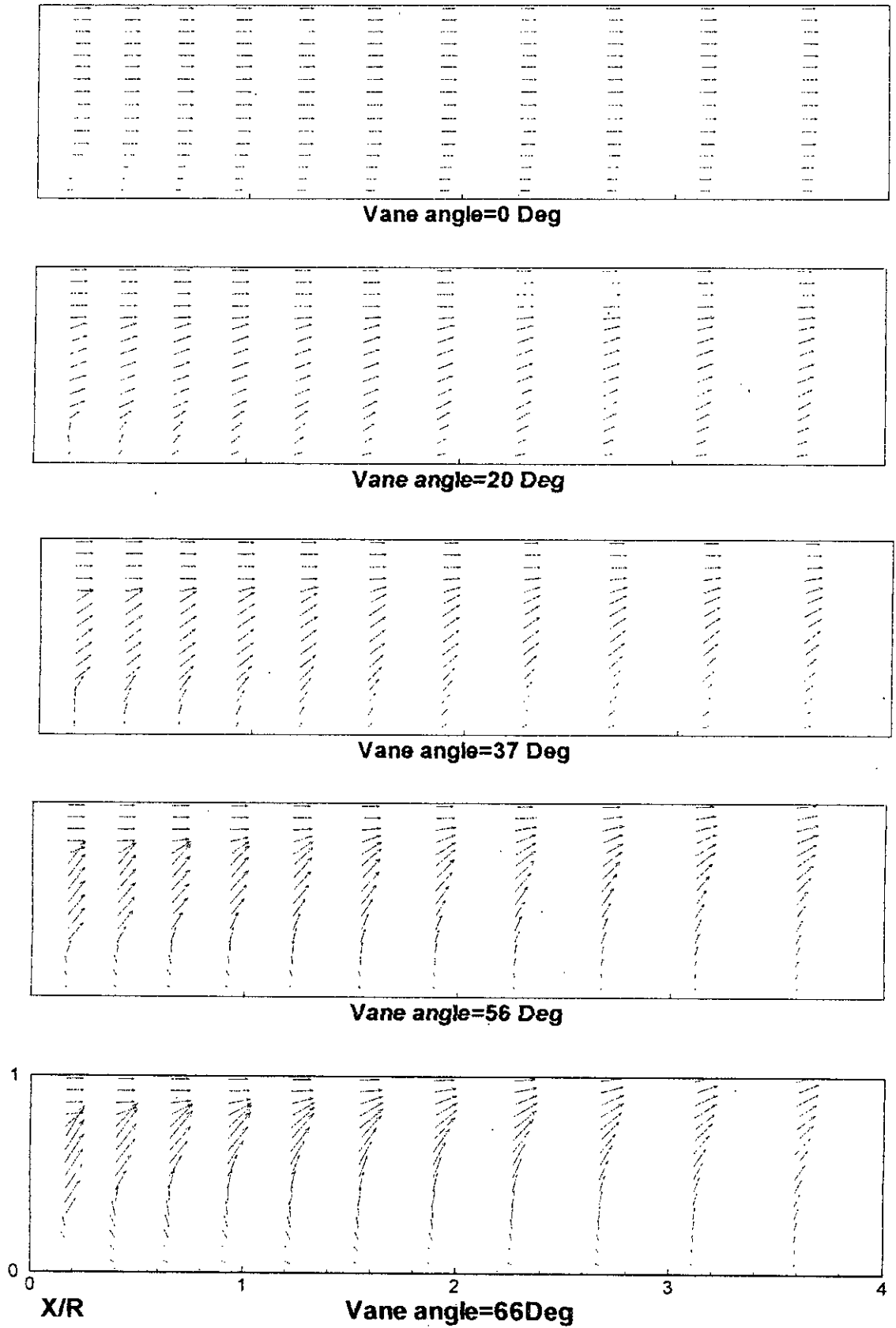


FIG. 10. Comparison of vector Diagram for combined axial and tangential velocities at inlet for constant vane angle swirl generator for Case-I

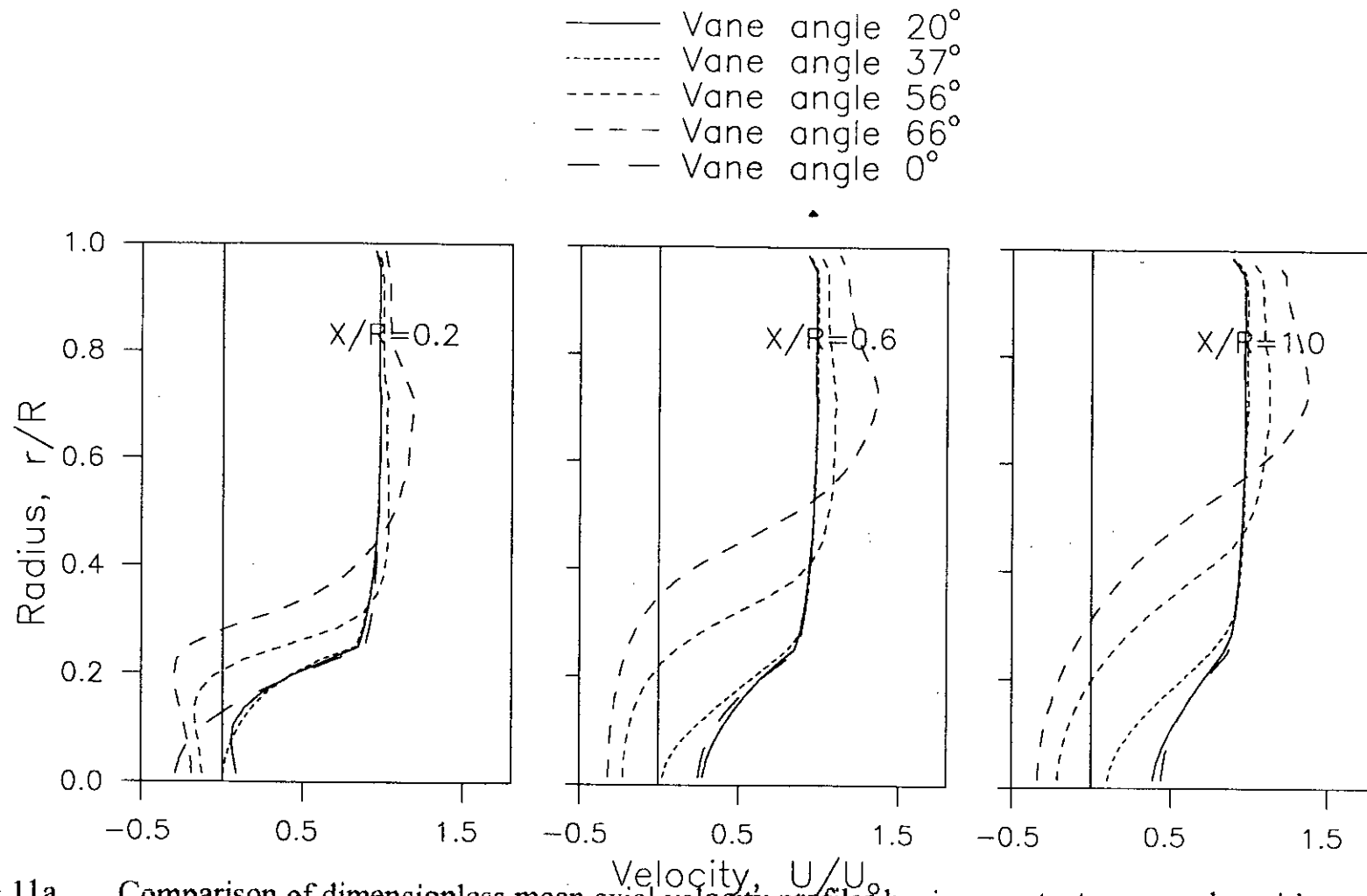


FIG.11a. Comparison of dimensionless mean axial velocity profiles having constant vane angle swirl generator at inlet.

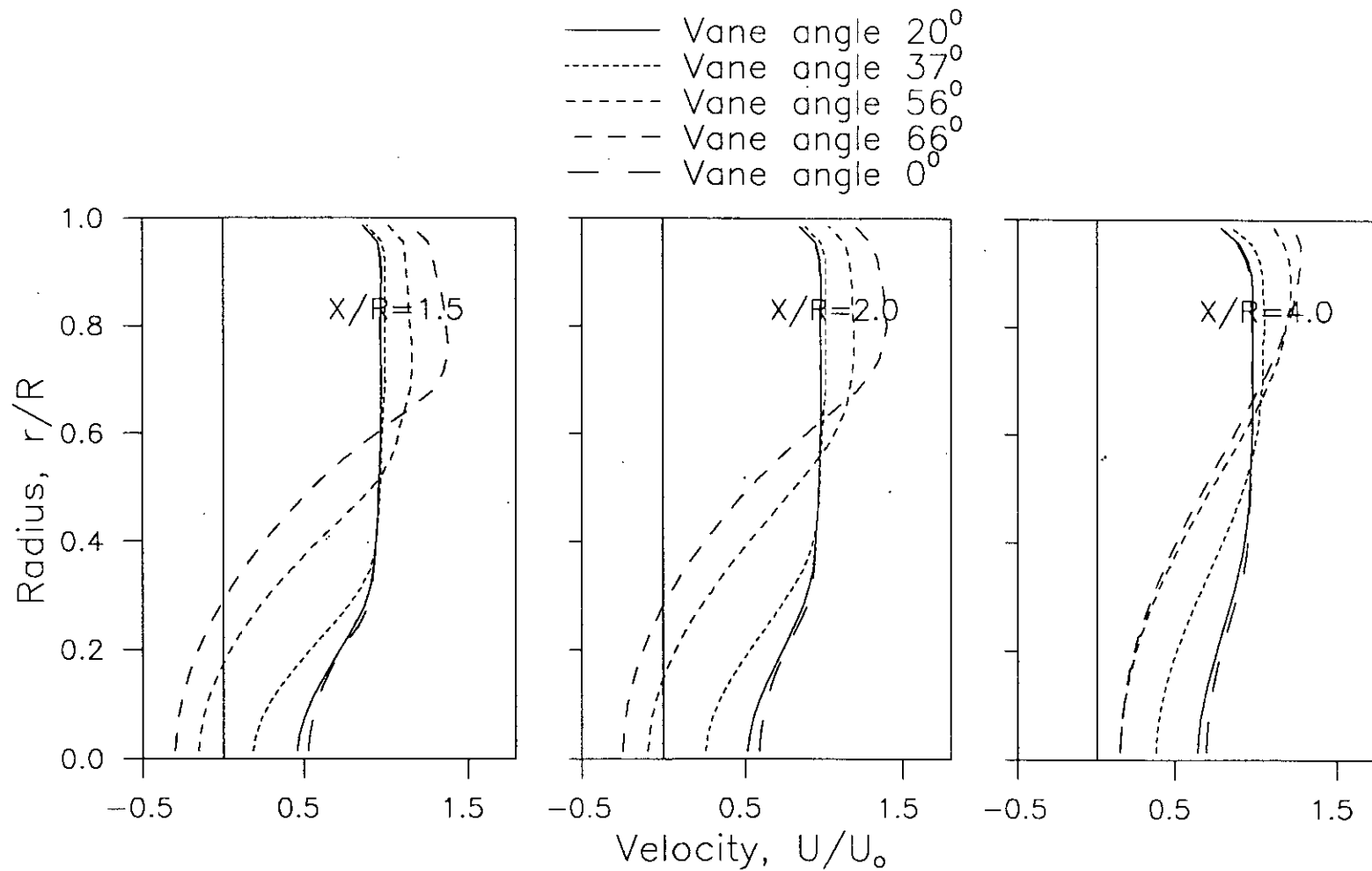


FIG.11b. Comparison of dimensionless mean axial velocity profiles having constant vane angle swirl generator at inlet.

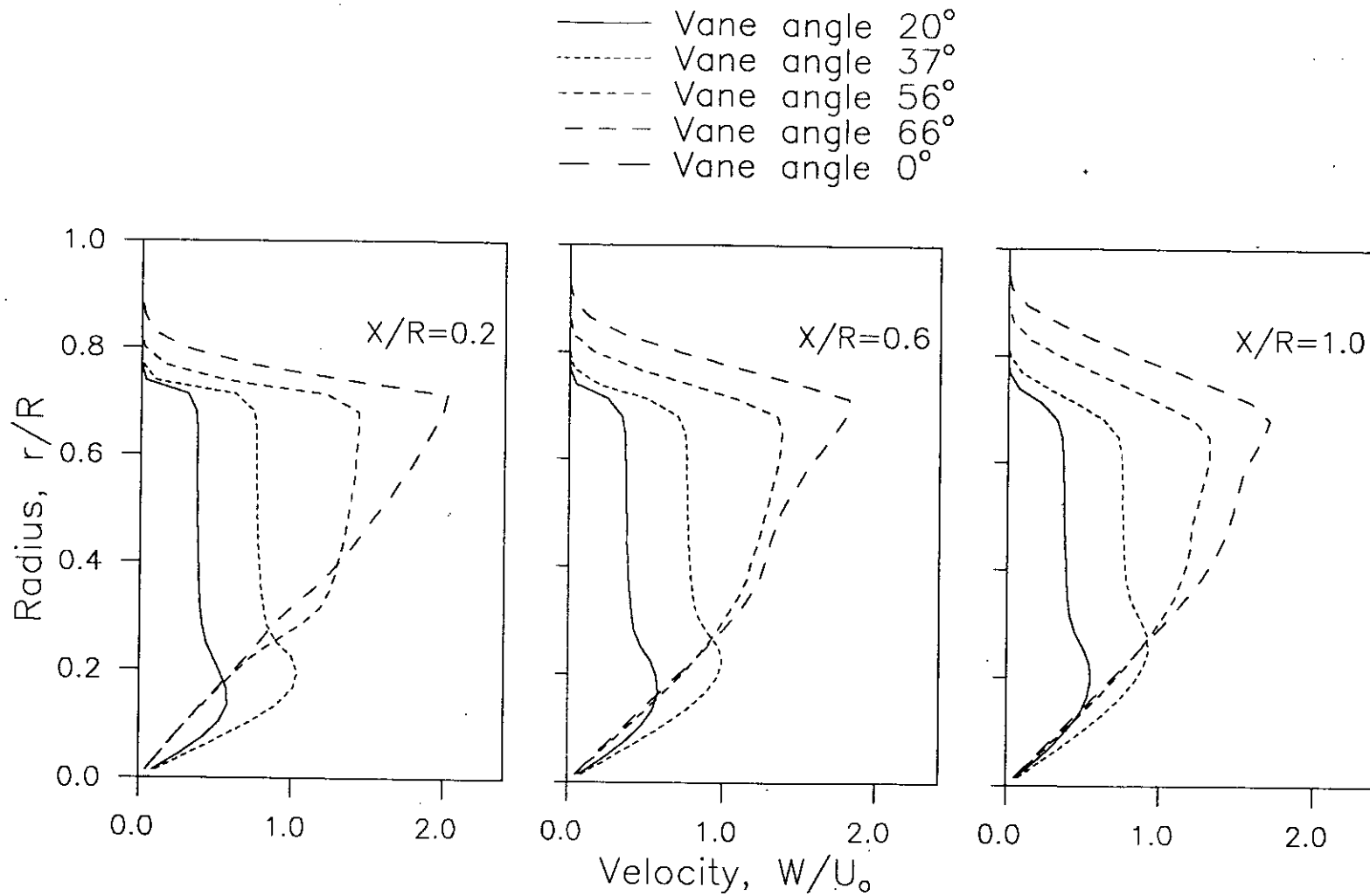


FIG.12a. Comparison of dimensionless mean tangential velocity profiles having constant vane angle swirl generator at inlet.

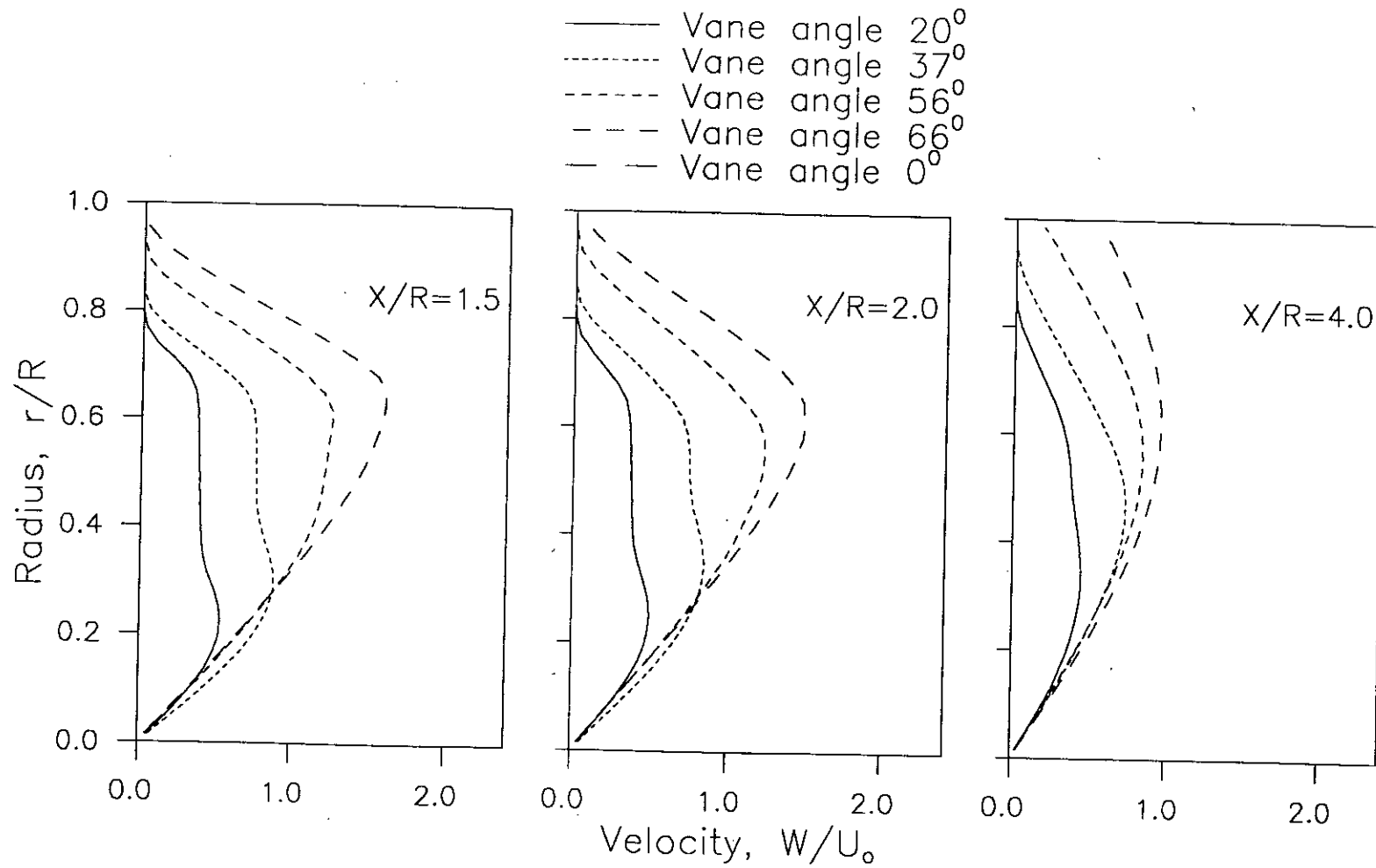


FIG.12b. Comparison of dimensionless mean tangential velocity profiles having constant vane angle swirl generator at inlet.

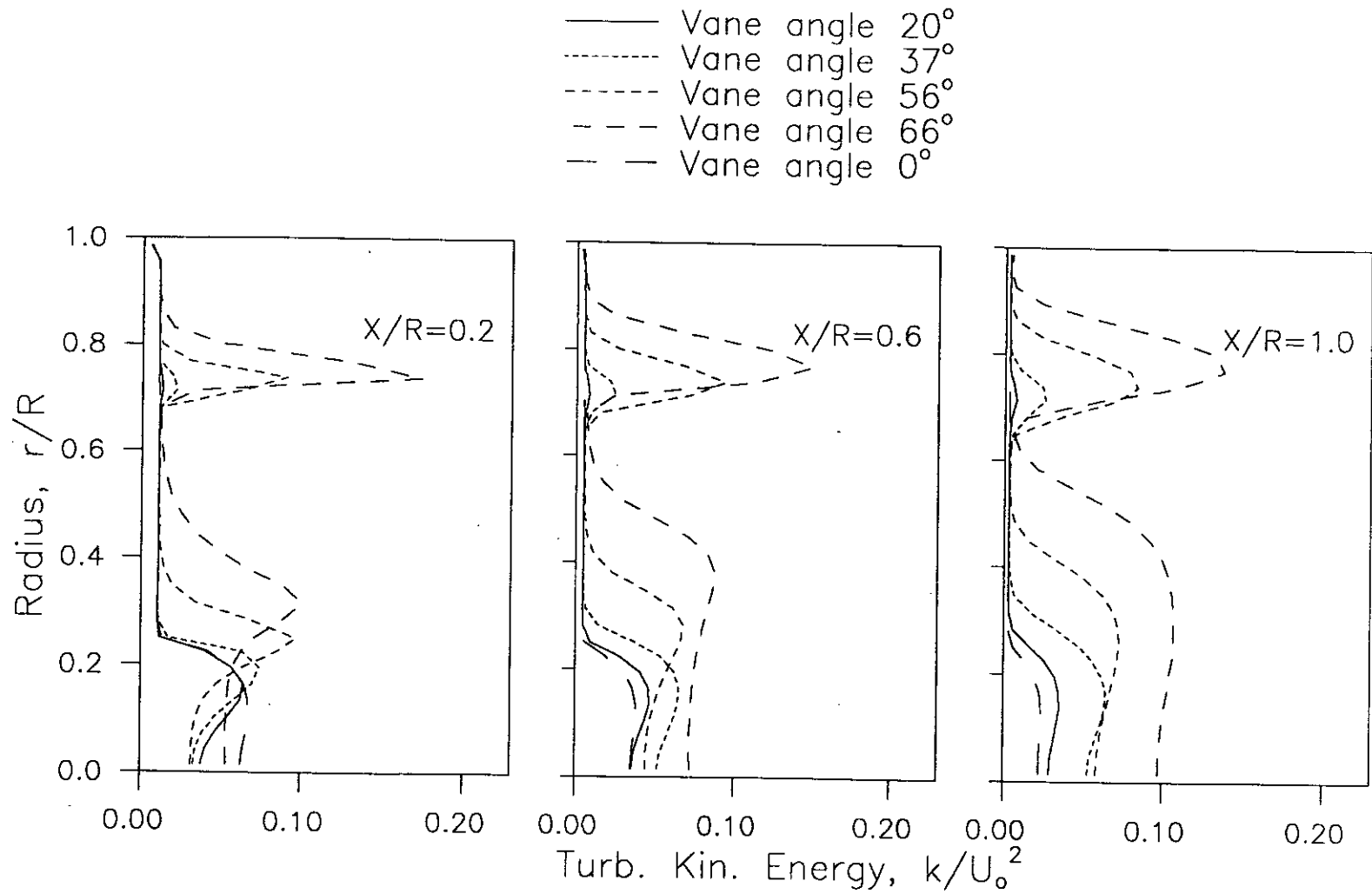


FIG.13a. Comparison of dimensionless turbulence kinetic energy profiles having constant vane angle swirl generator at inlet.



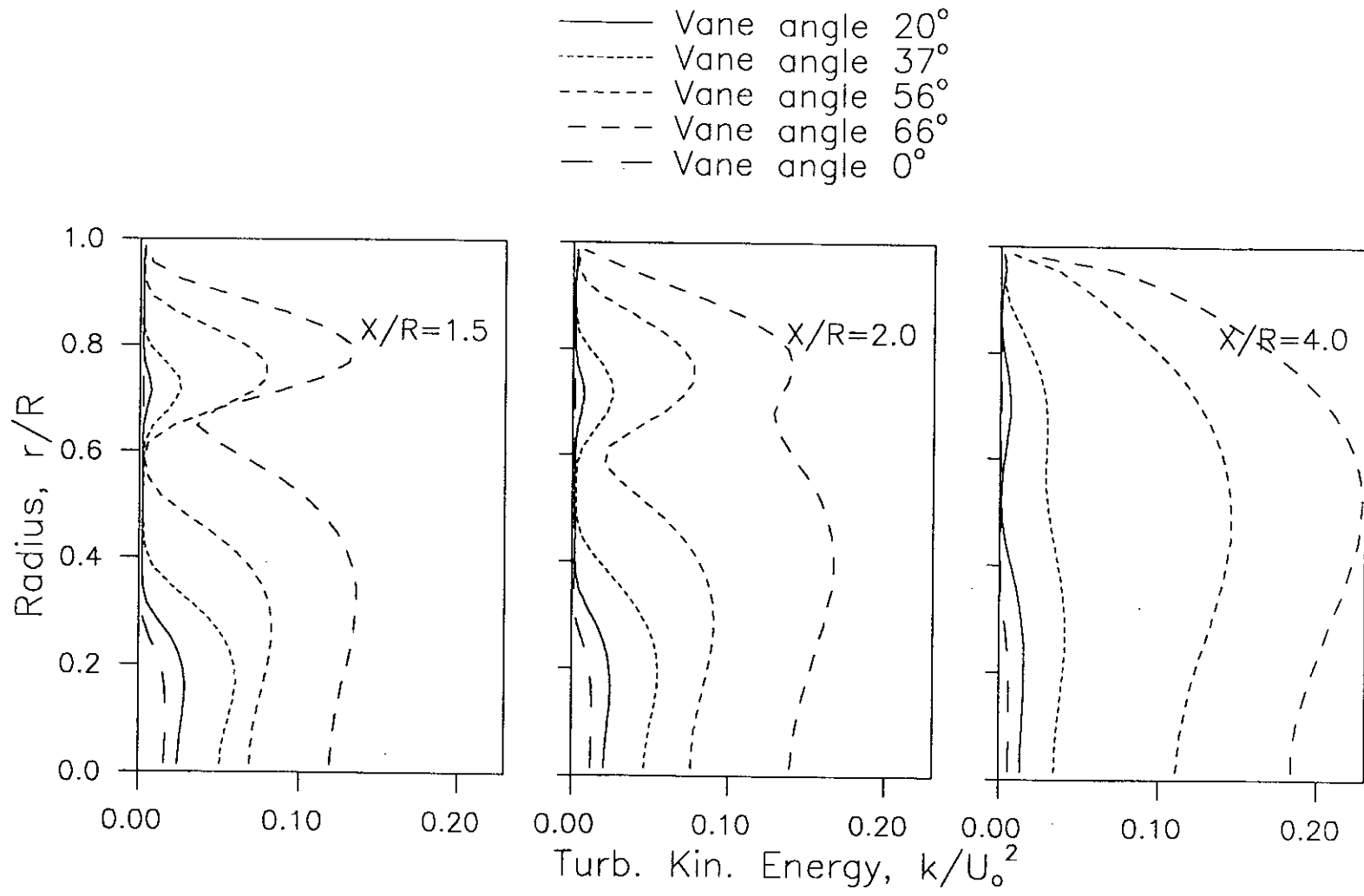


FIG.13b. Comparison of dimensionless turbulence kinetic energy profiles having constant vane angle swirl generator at inlet.

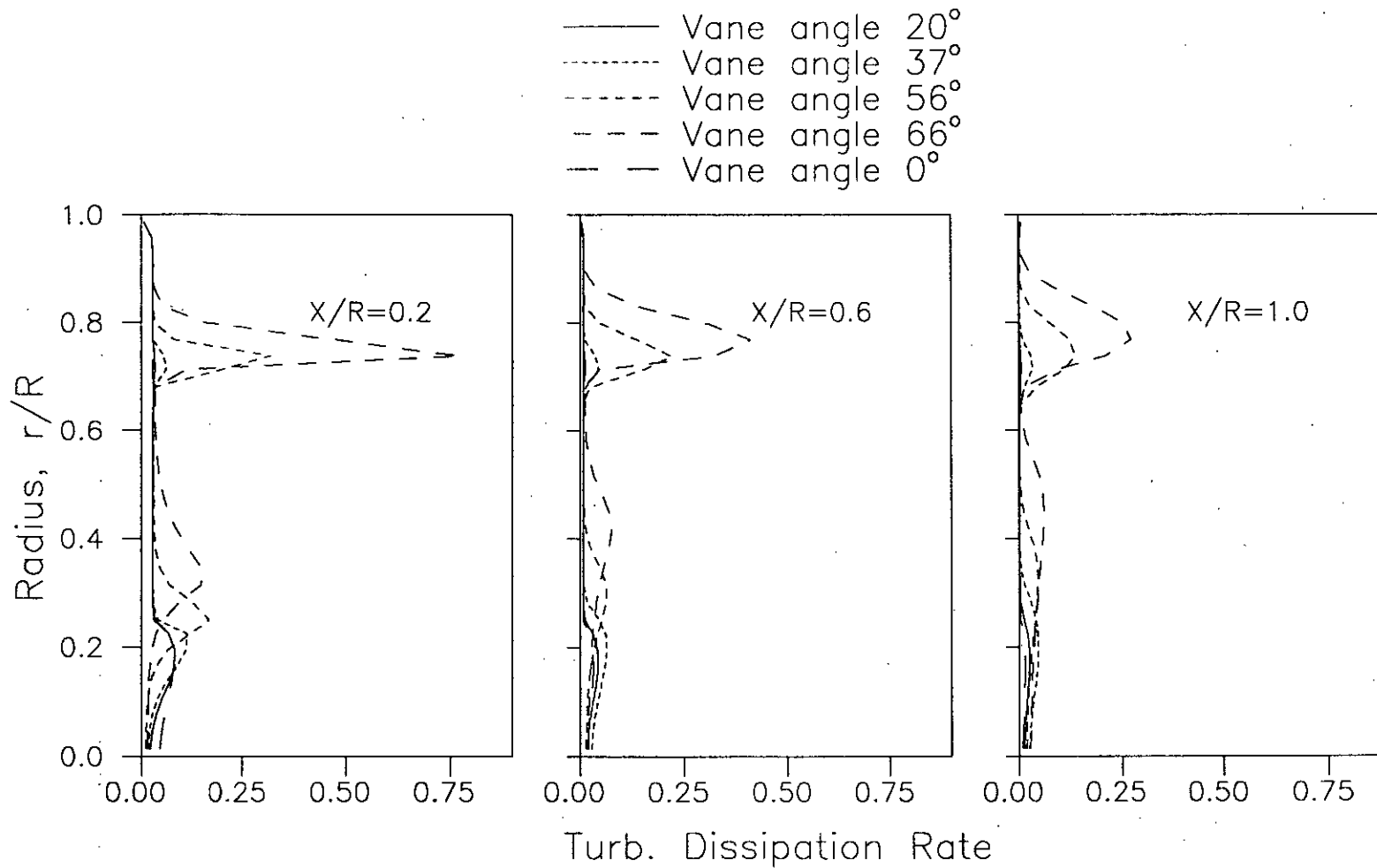


FIG.14a. Comparison of dimensionless turbulence dissipation rate profiles having constant vane angle swirl generator at inlet.

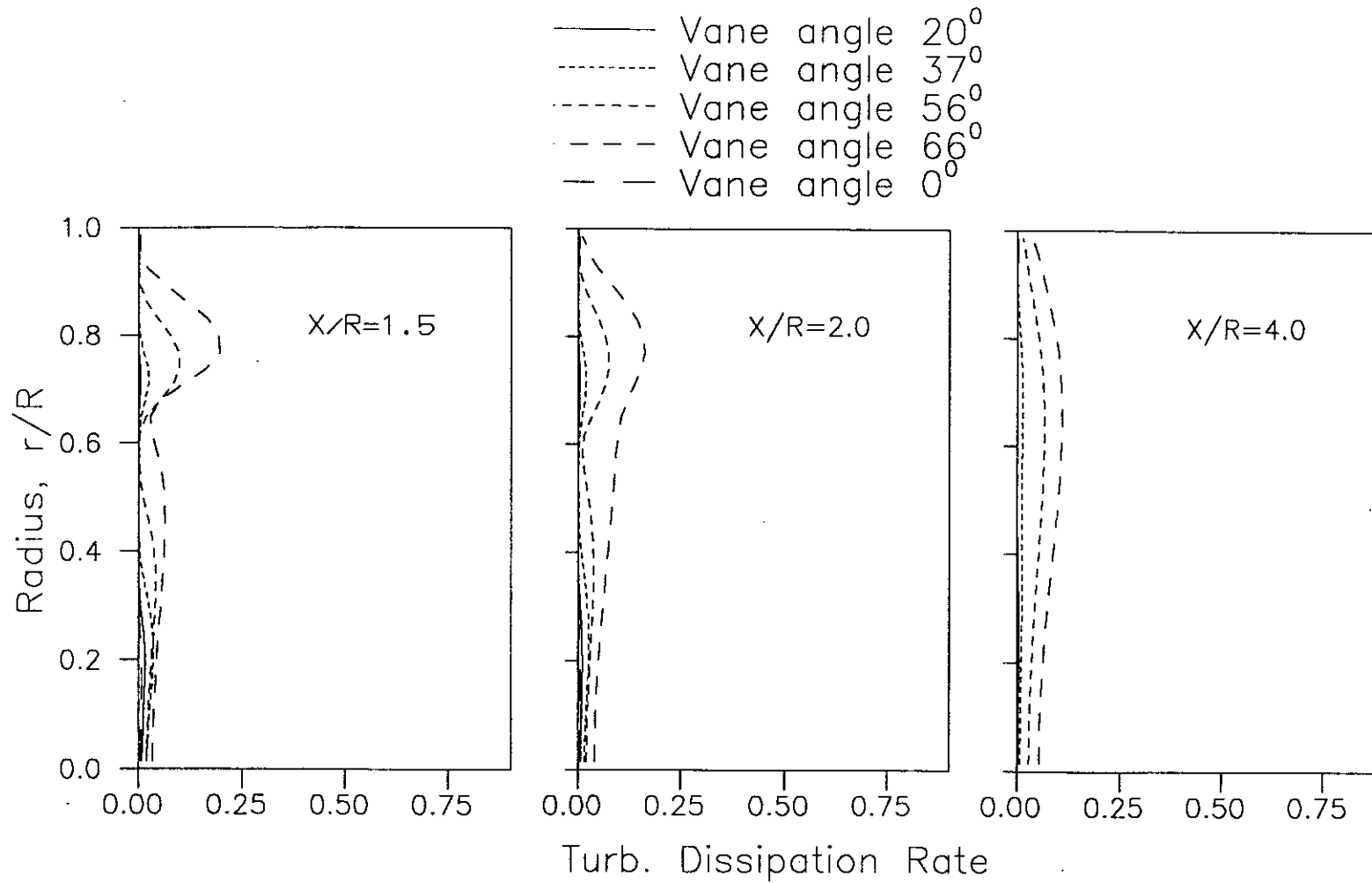
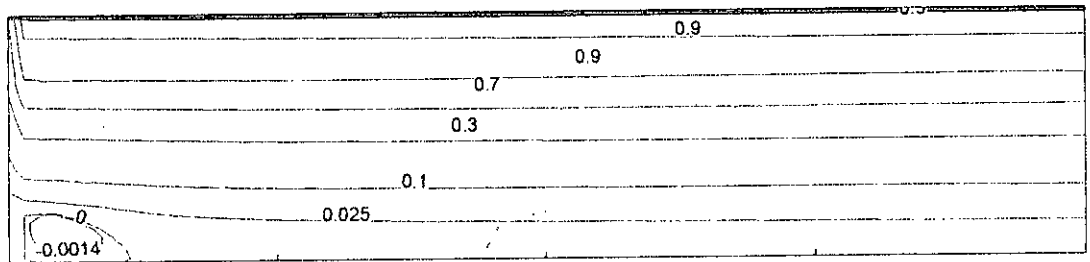
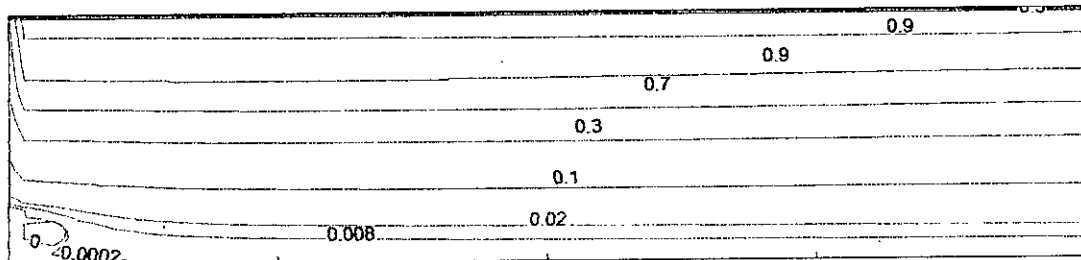


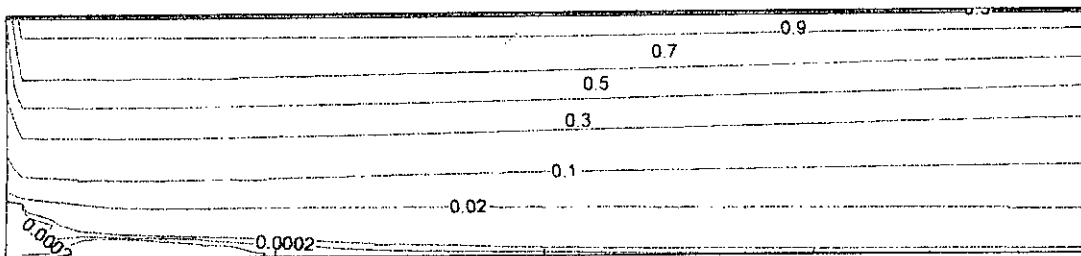
FIG.14b. Comparison of dimensionless turbulence dissipation rate profiles having constant vane angle swirl generator at inlet.



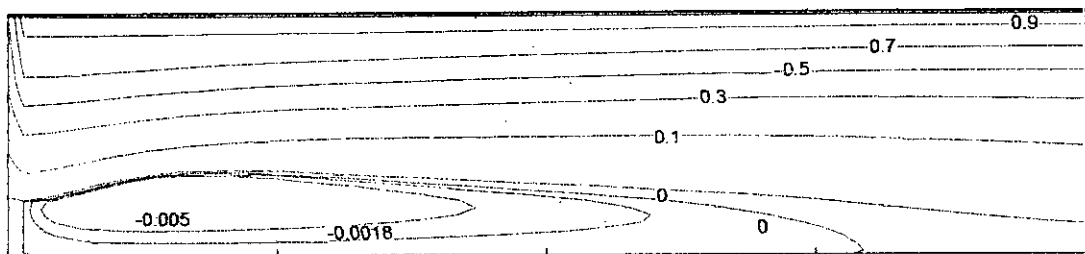
**Vane angle=0 deg**



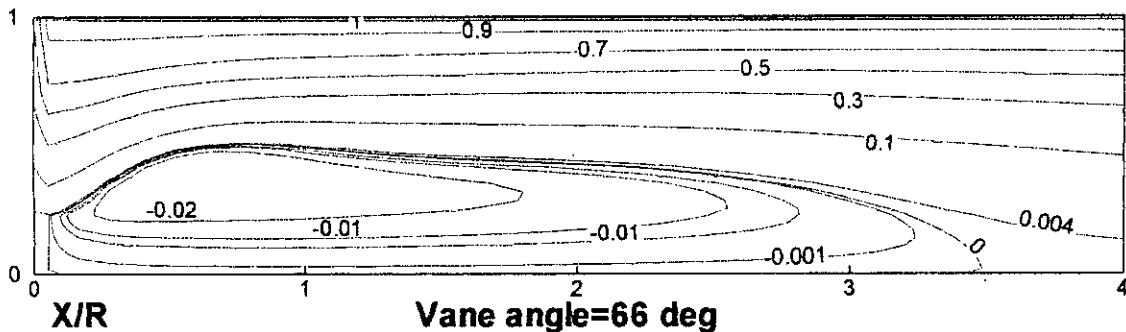
**Vane angle=20 deg**



**Vane angle=37 deg**



**Vane angle=56 deg**



**Vane angle=66 deg**

**FIG. 15.. Streamline plots for constant vane angle swirl generator at inlet for Case-II**

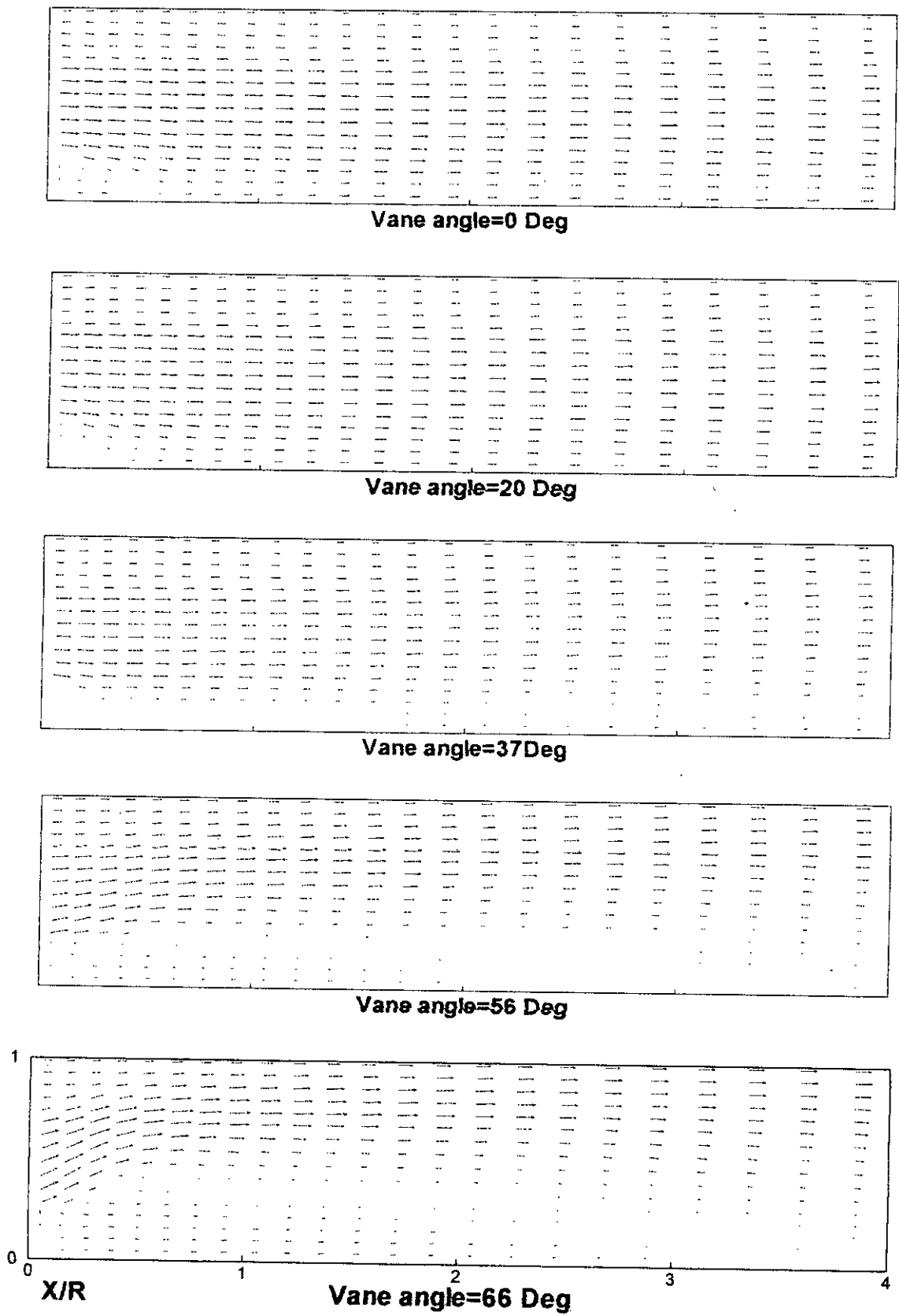


FIG.16. Comparison of vector Diagram for combined axial and radial velocities at inlet for constant vane angle swirl generator for Case-II

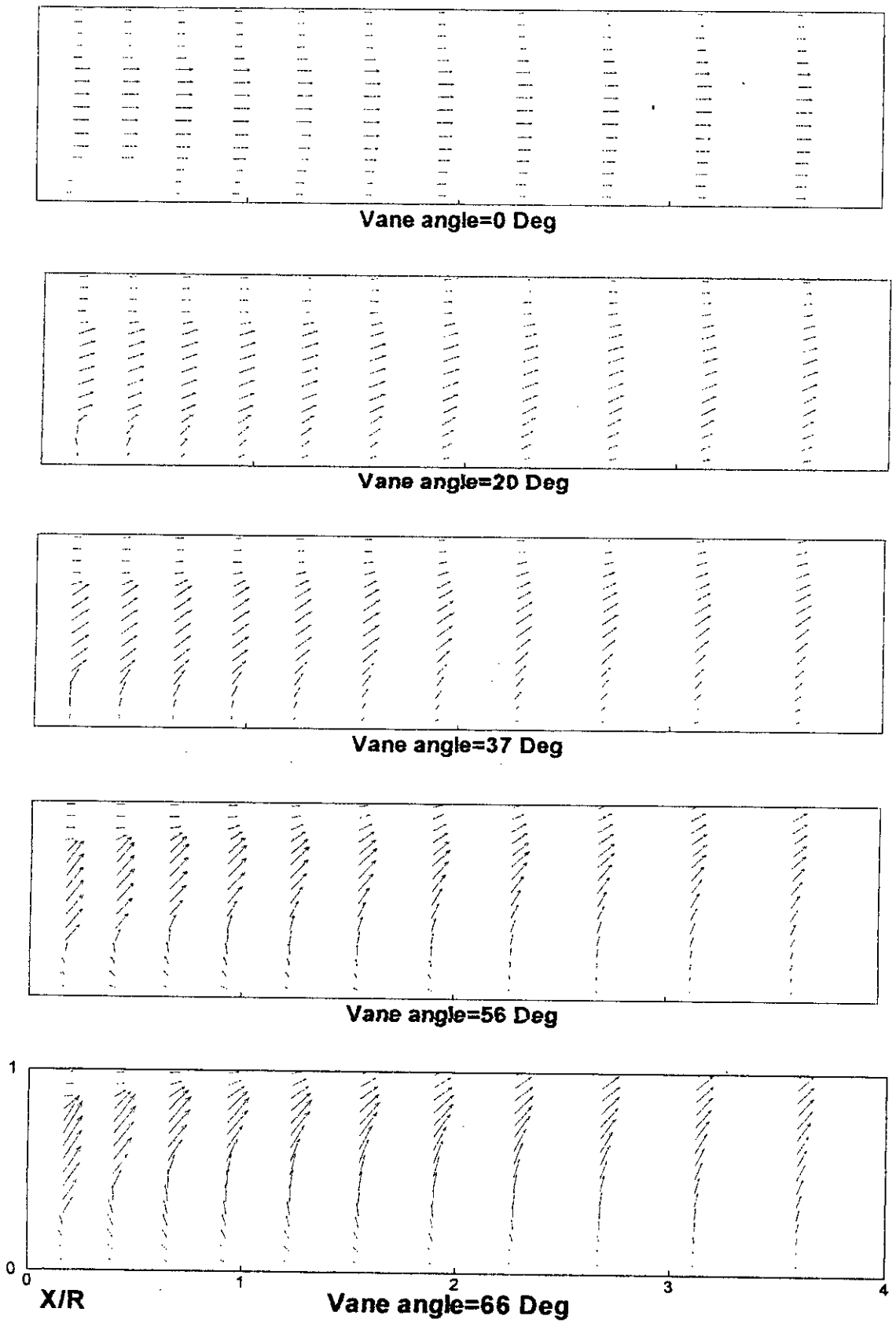


FIG.17. Comparison of vector Diagram for combined axial and tangential velocities at inlet for constant vane angle swirl generator for Case-II

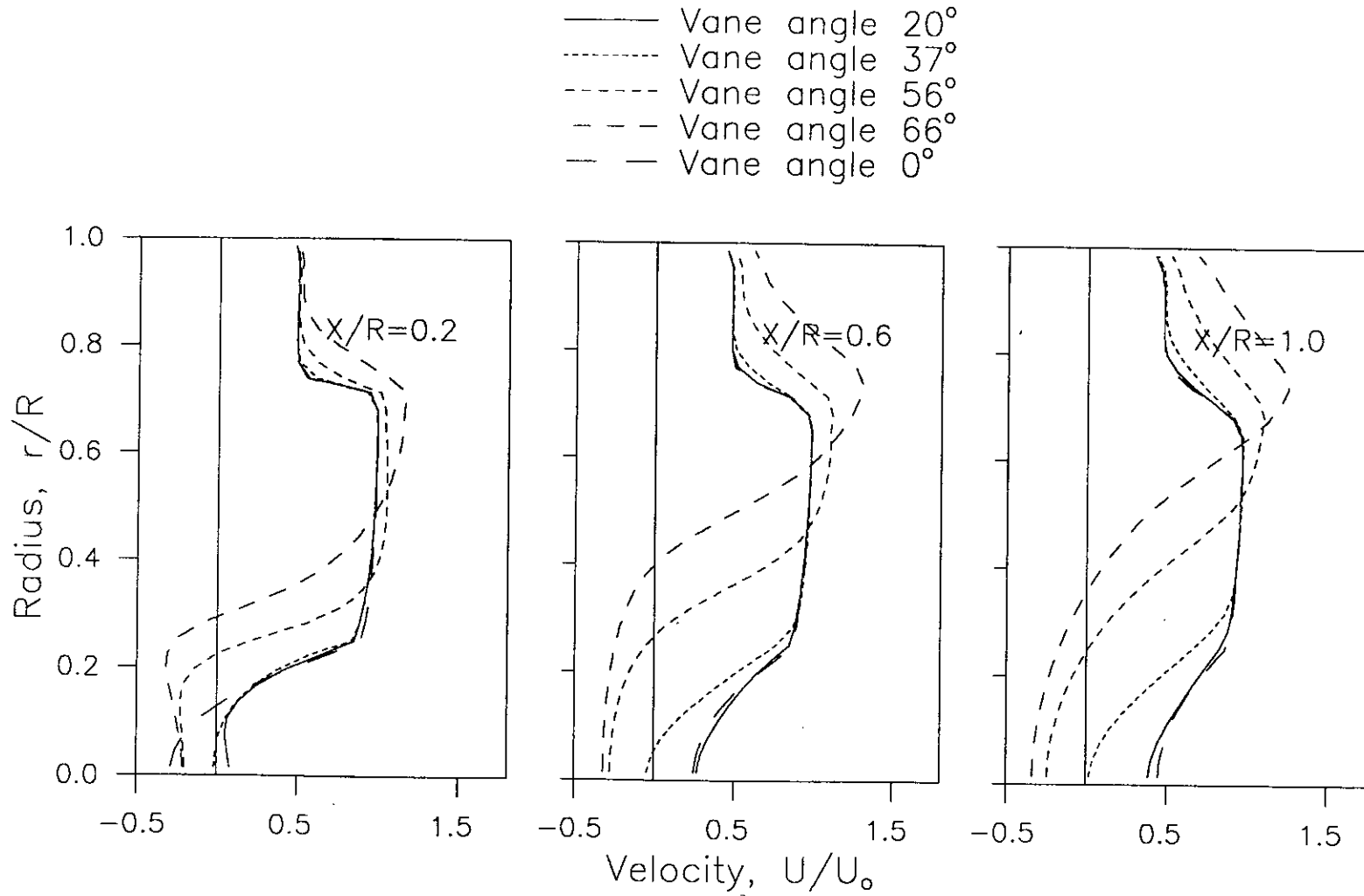


FIG. 18a. Comparison of dimensionless mean axial velocity profiles having constant vane angle swirl generator at inlet For Case-II.

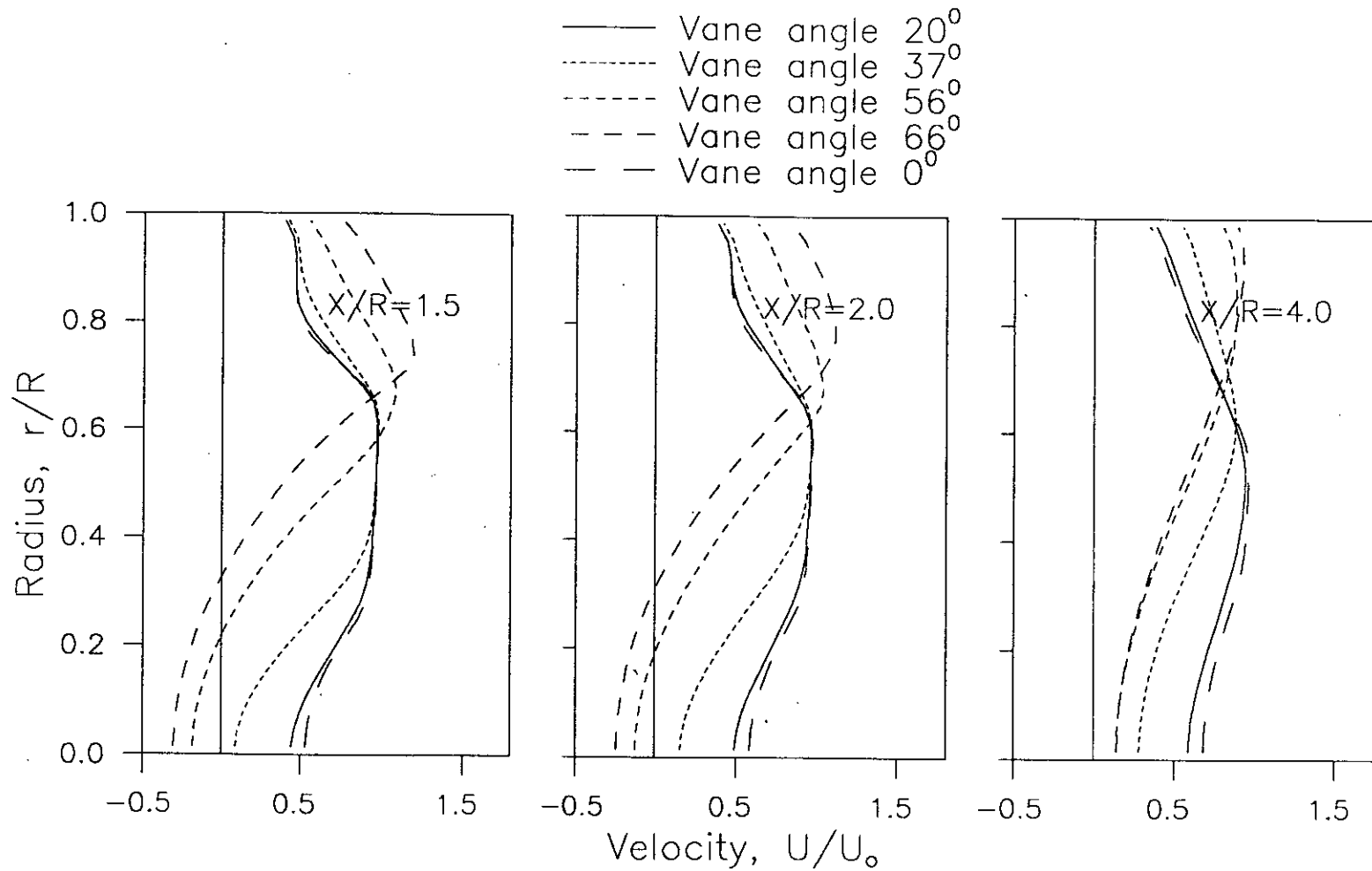


FIG.18b. Comparison of dimensionless mean axial velocity profiles having constant vane angle swirl generator at inlet For Case-II.



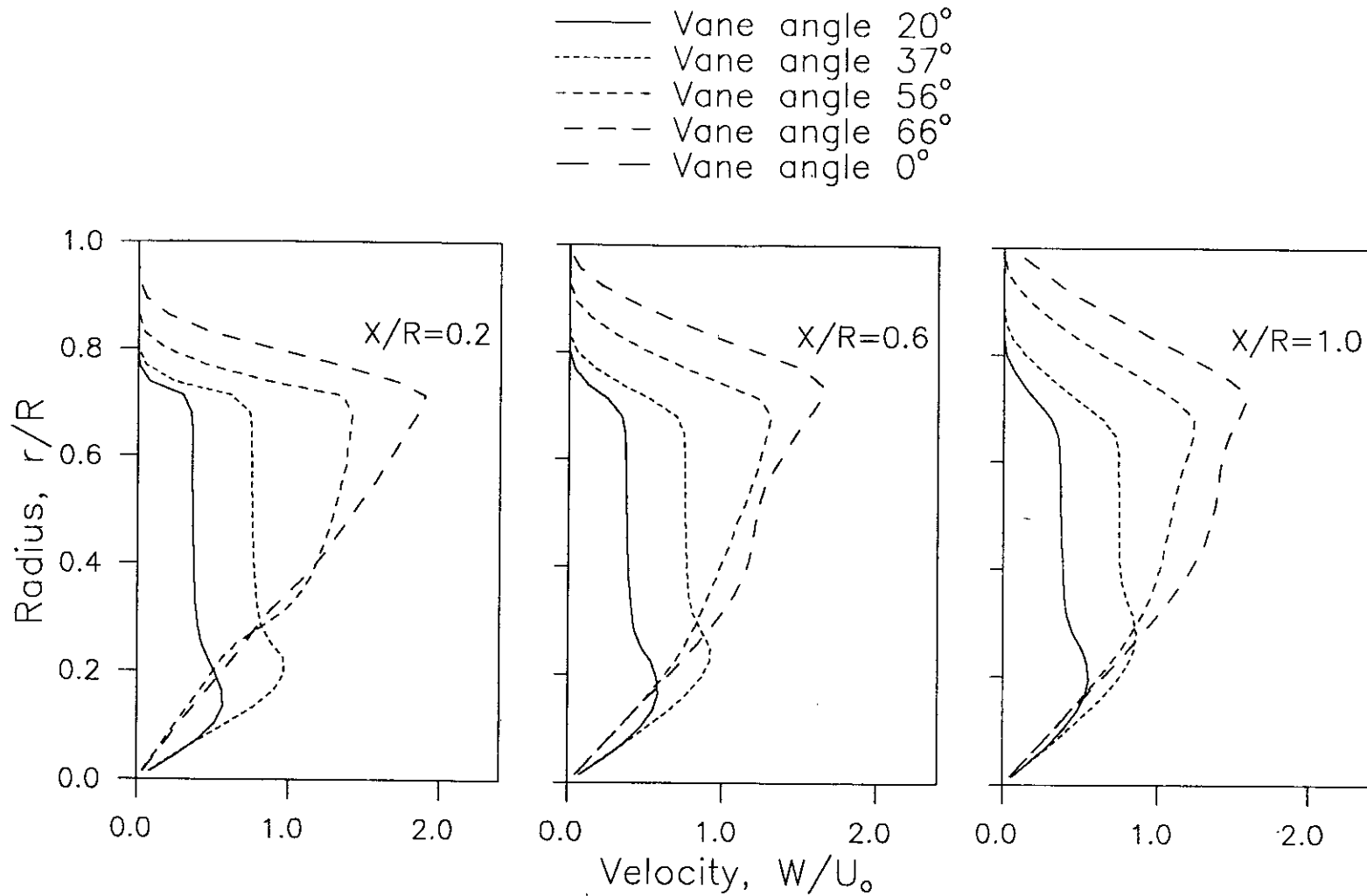


FIG.19a. Comparison of dimensionless mean tangential velocity profiles having constant vane angle swirl generator at inlet For Case-II.

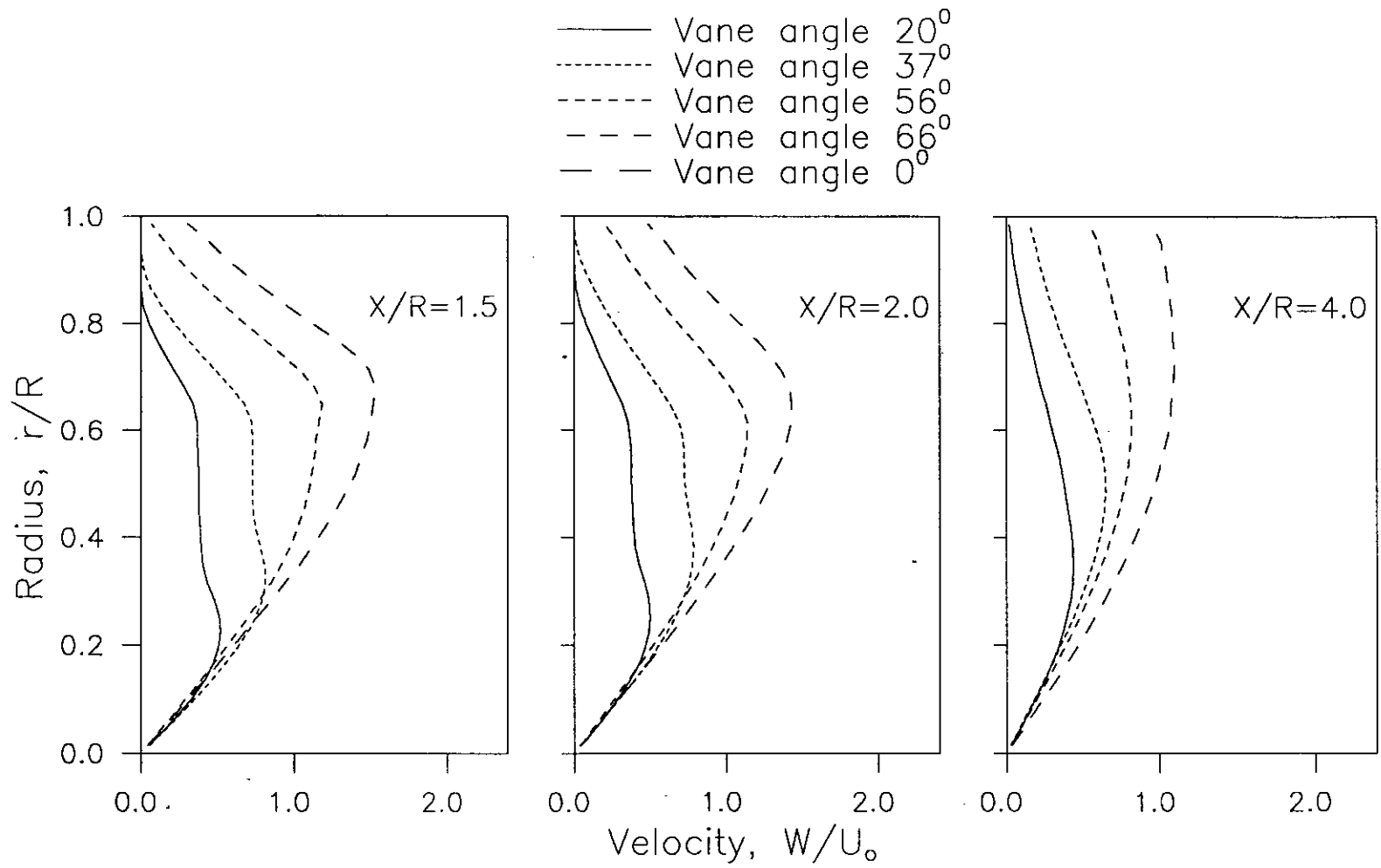


FIG.19b. Comparison of dimensionless mean tangential velocity profiles having constant vane angle swirl generator at inlet For Case-II.

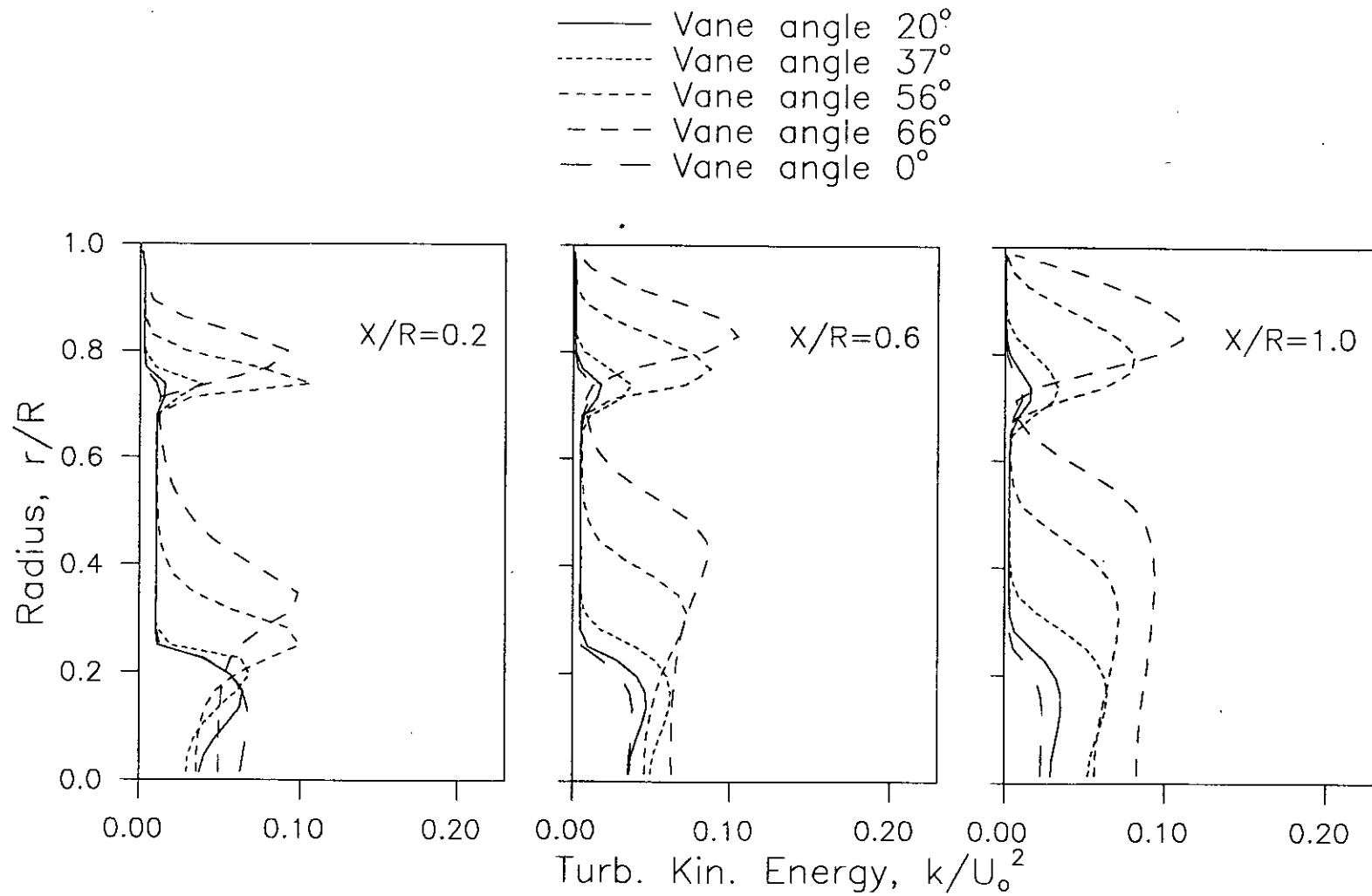


FIG.20a. Comparison of dimensionless turbulence kinetic energy profiles having constant vane angle swirl generator at inlet For Case-II.

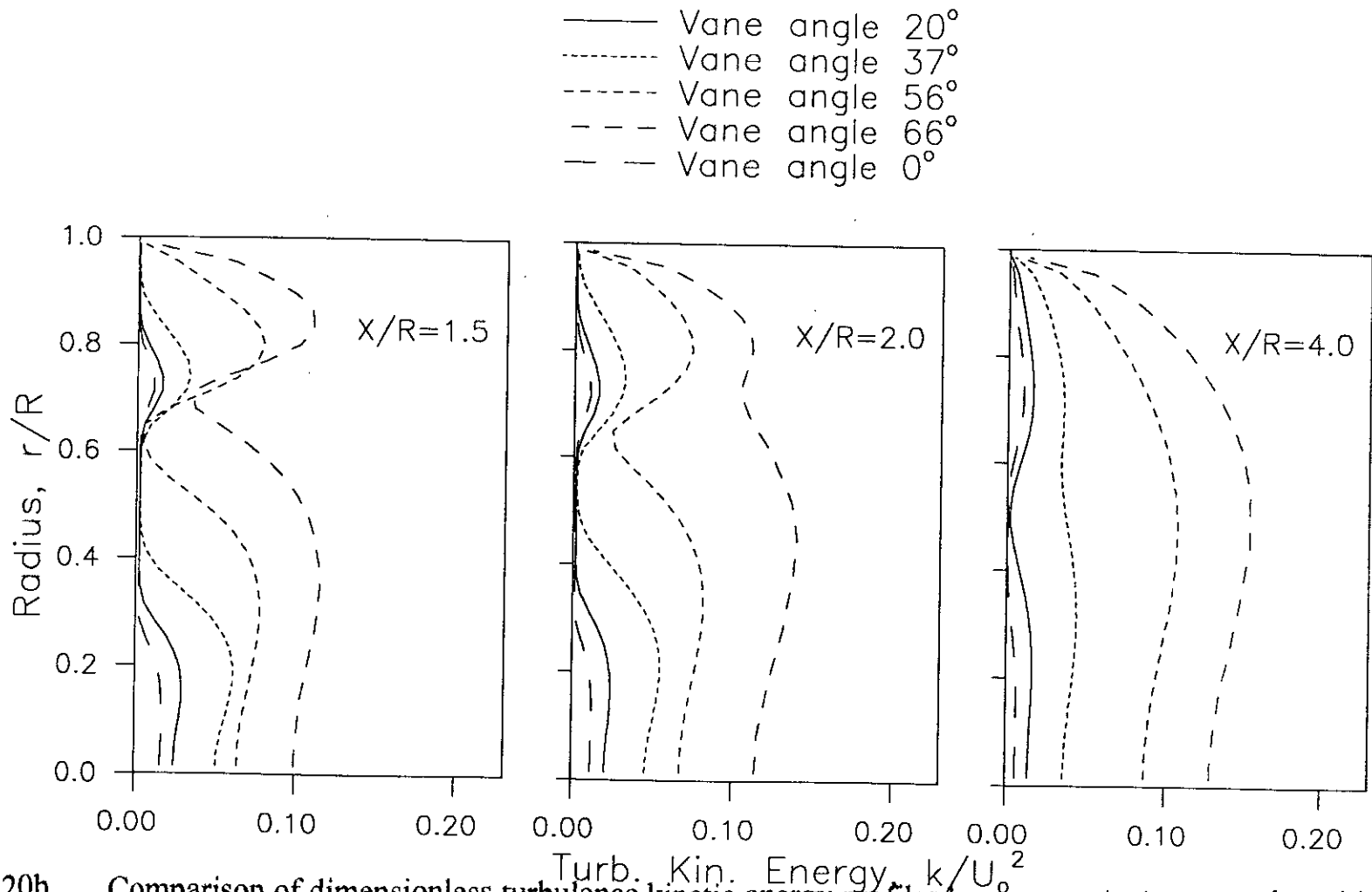


FIG.20b. Comparison of dimensionless turbulence kinetic energy profiles having constant vane angle swirl generator at inlet For Case-II.

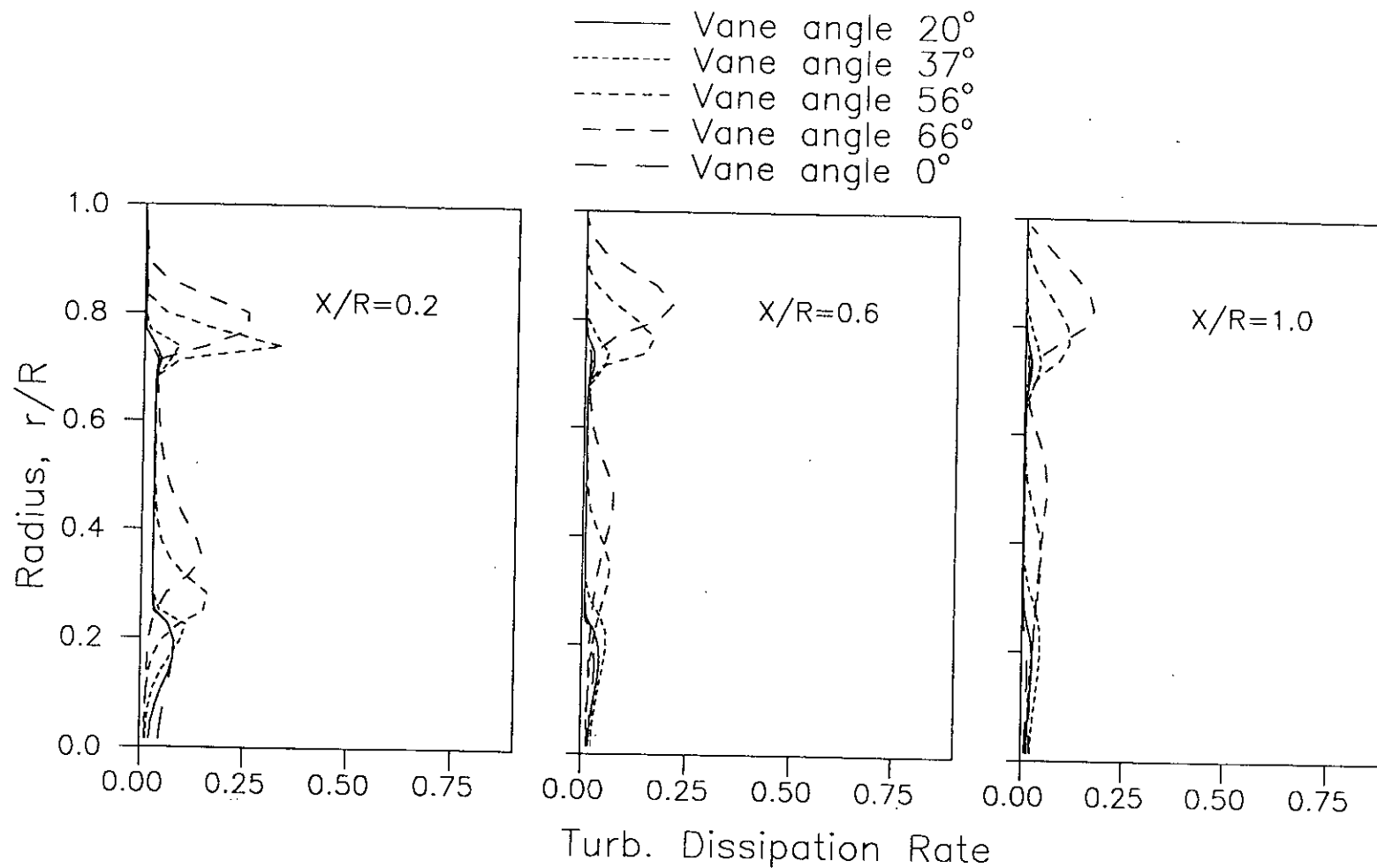


FIG.21a. Comparison of dimensionless turbulence dissipation rate profiles having constant vane angle swirl generator at inlet For Case-II.

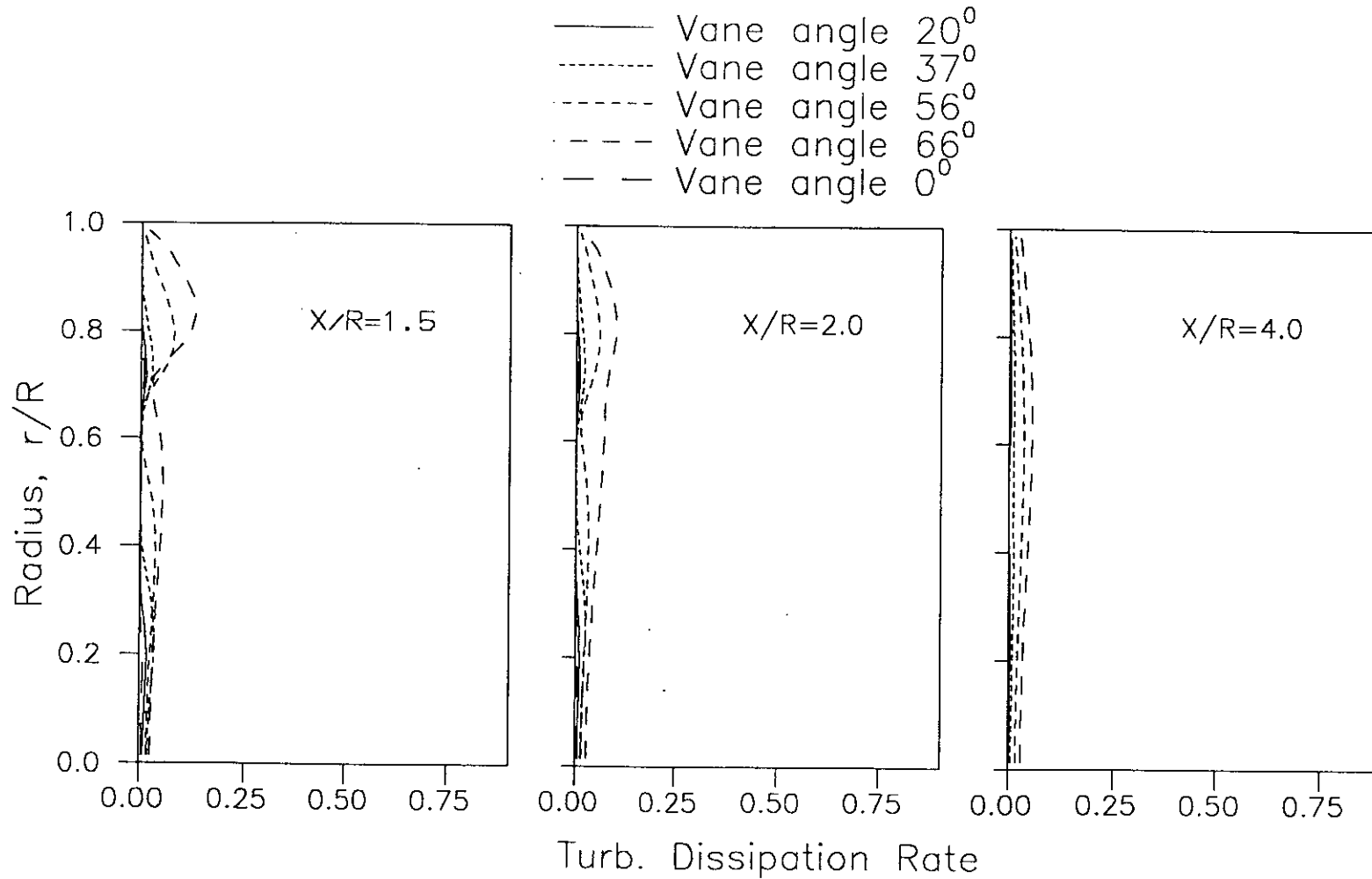


FIG.21b. Comparison of dimensionless turbulence dissipation rate profiles having constant vane angle swirl generator at inlet For Case-II.

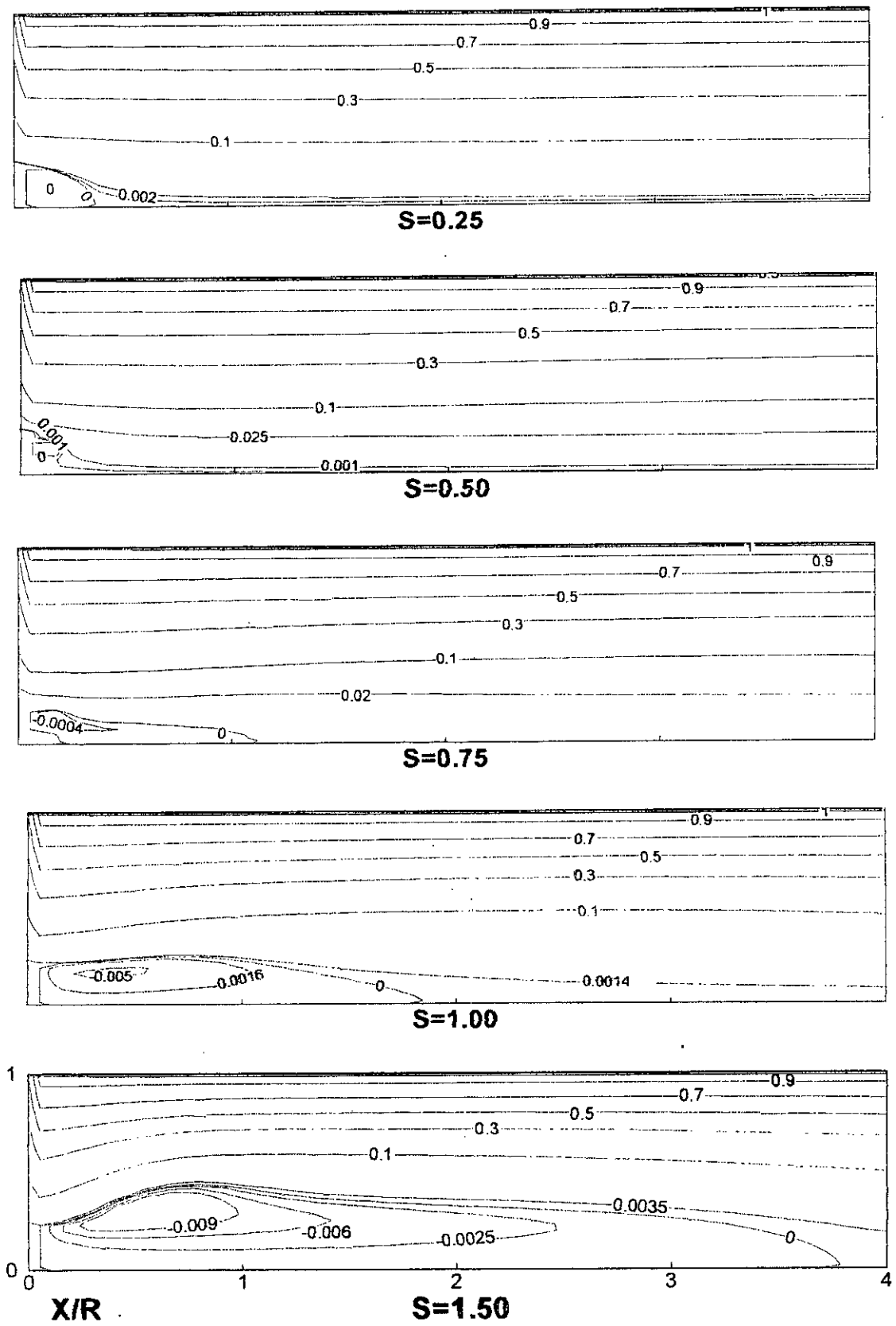


FIG. 22. Streamline plots for solid body rotation swirl generator at inlet for Case-I.

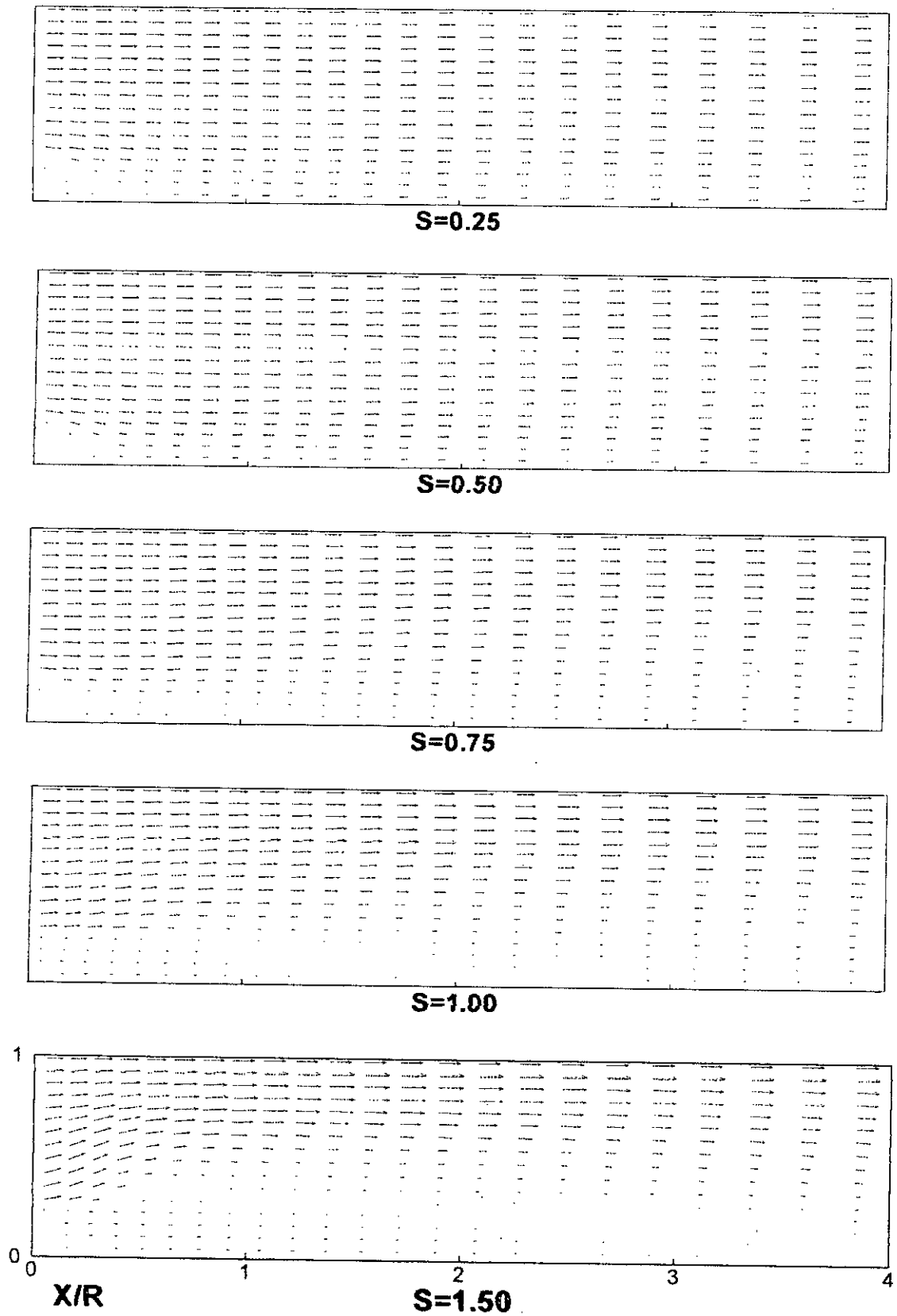


FIG.23. Comparison of vector Diagram for combined axial and radial velocities at inlet for solid body swirl generator for Case-I.



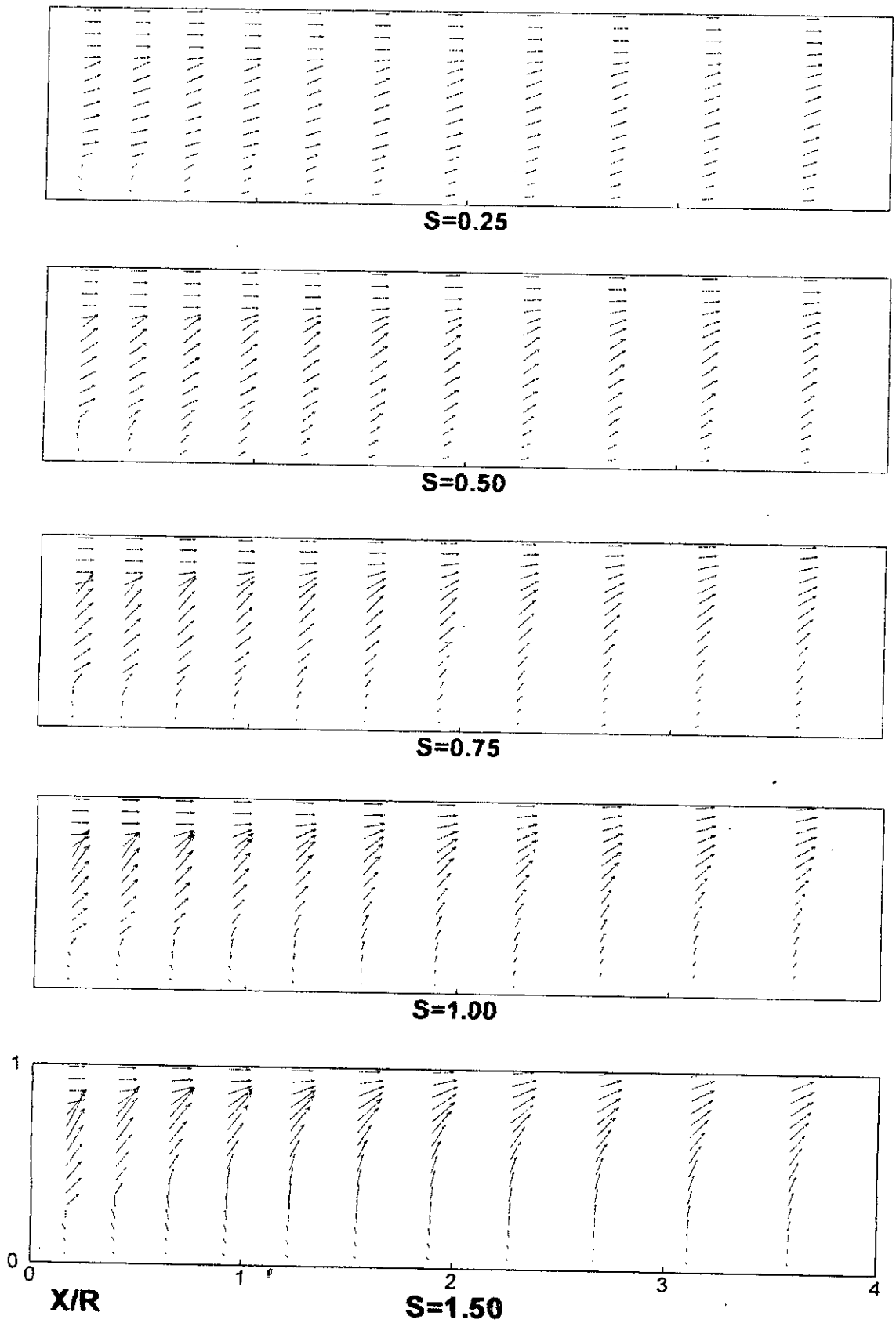


FIG.24. Comparison of vector Diagram for combined axial and tangential velocities at inlet for solid body swirl generator for Case-I.

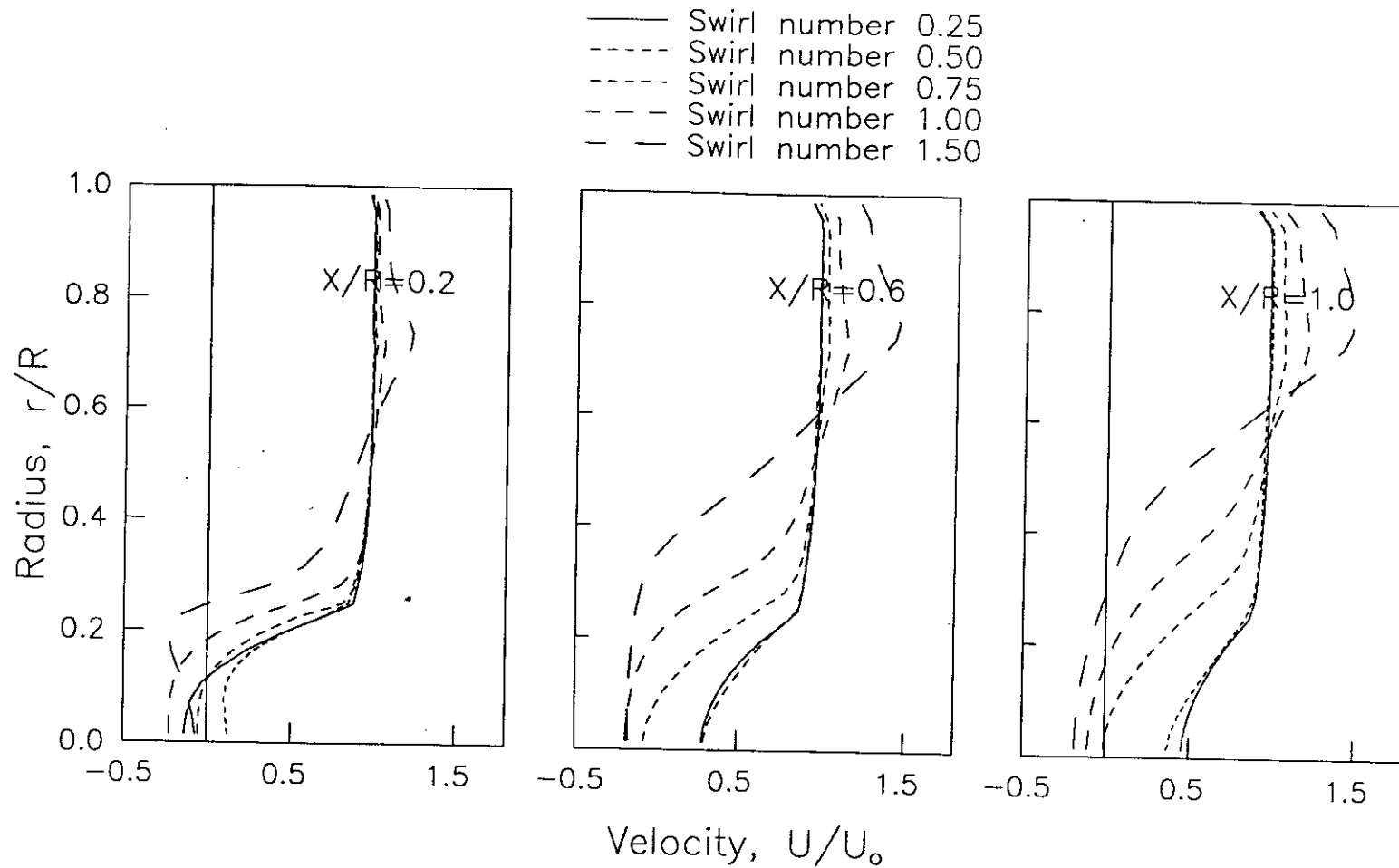


FIG.25a. Comparison of dimensionless mean axial velocity profiles having solid body swirl generator at inlet For Case-I.

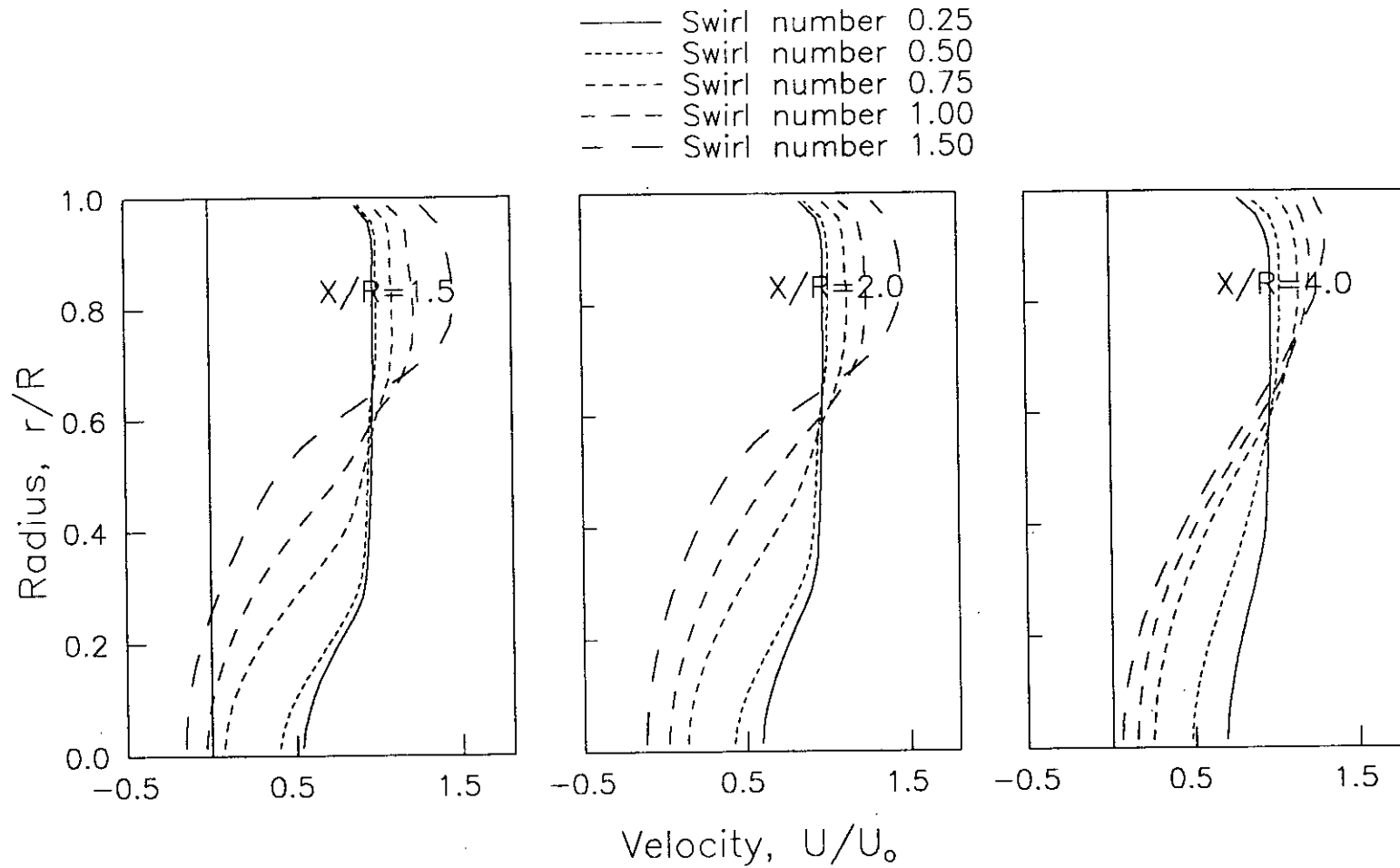


FIG.25b. Comparison of dimensionless mean axial velocity profiles having solid body swirl generator at inlet  
 For Case-I.

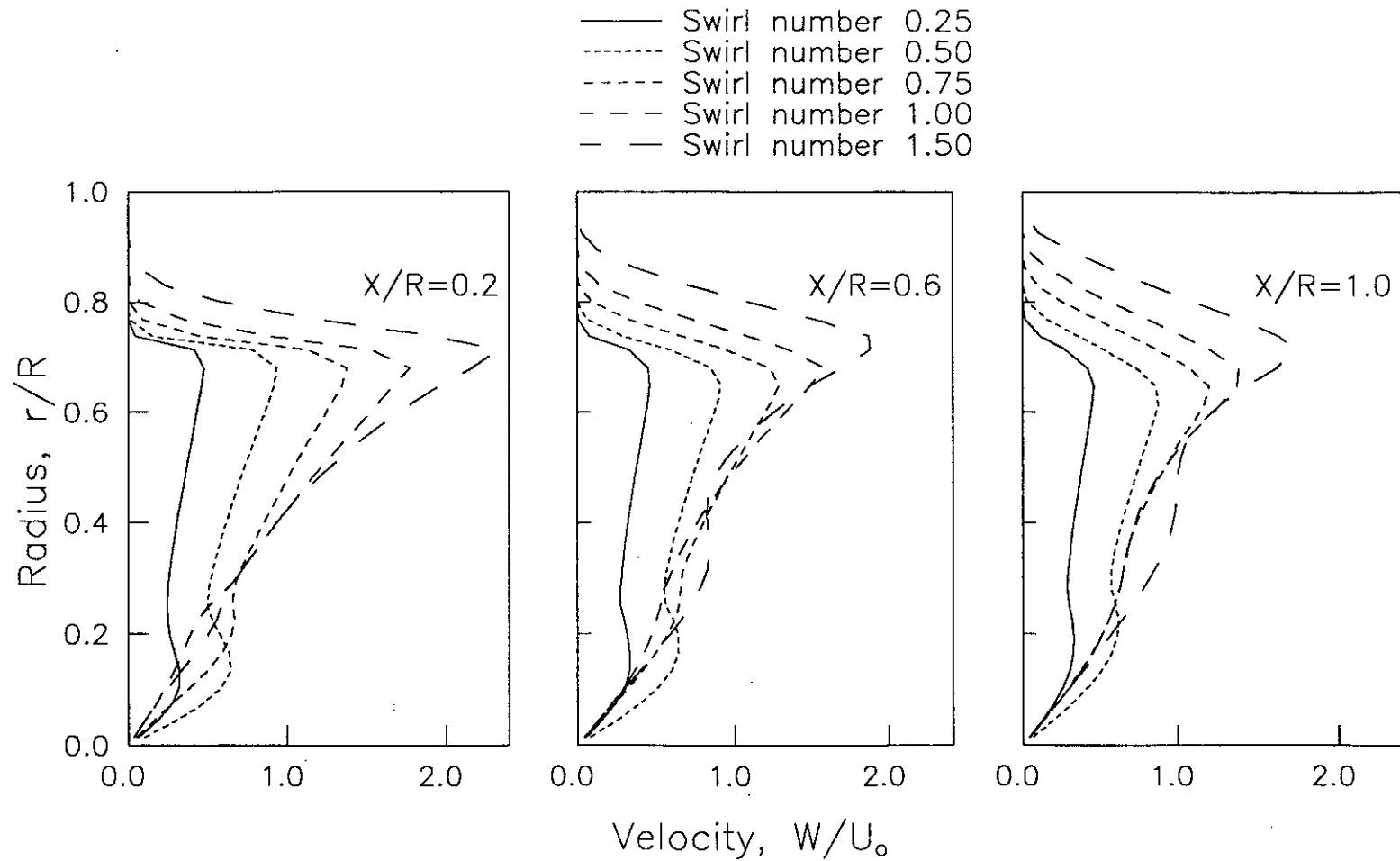


FIG.26a. Comparison of dimensionless mean tangential velocity profiles having solid body swirl generator at inlet For Case-I.

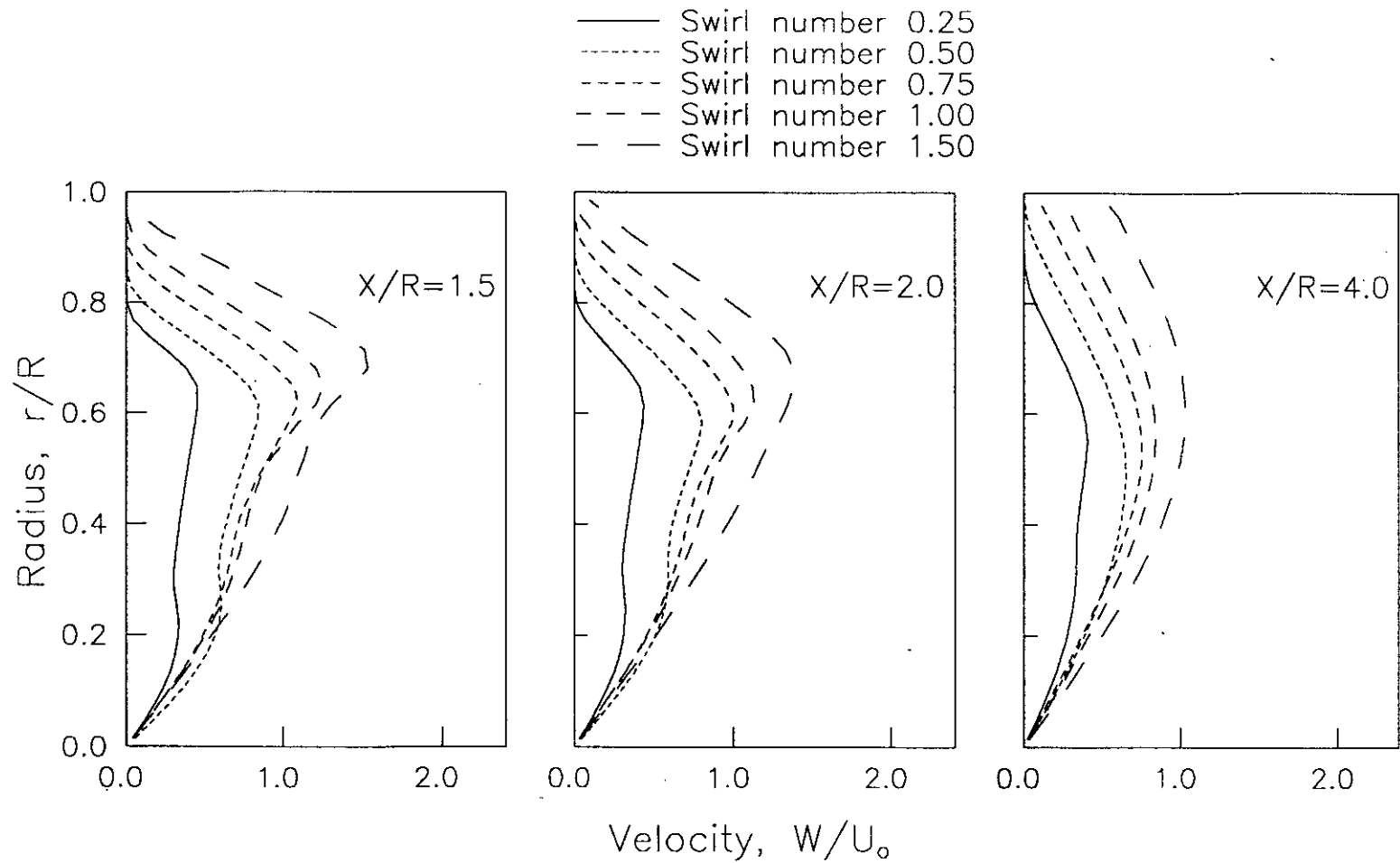


FIG.26b. Comparison of dimensionless tangential velocity profiles having solid body swirl generator at inlet for Case-II

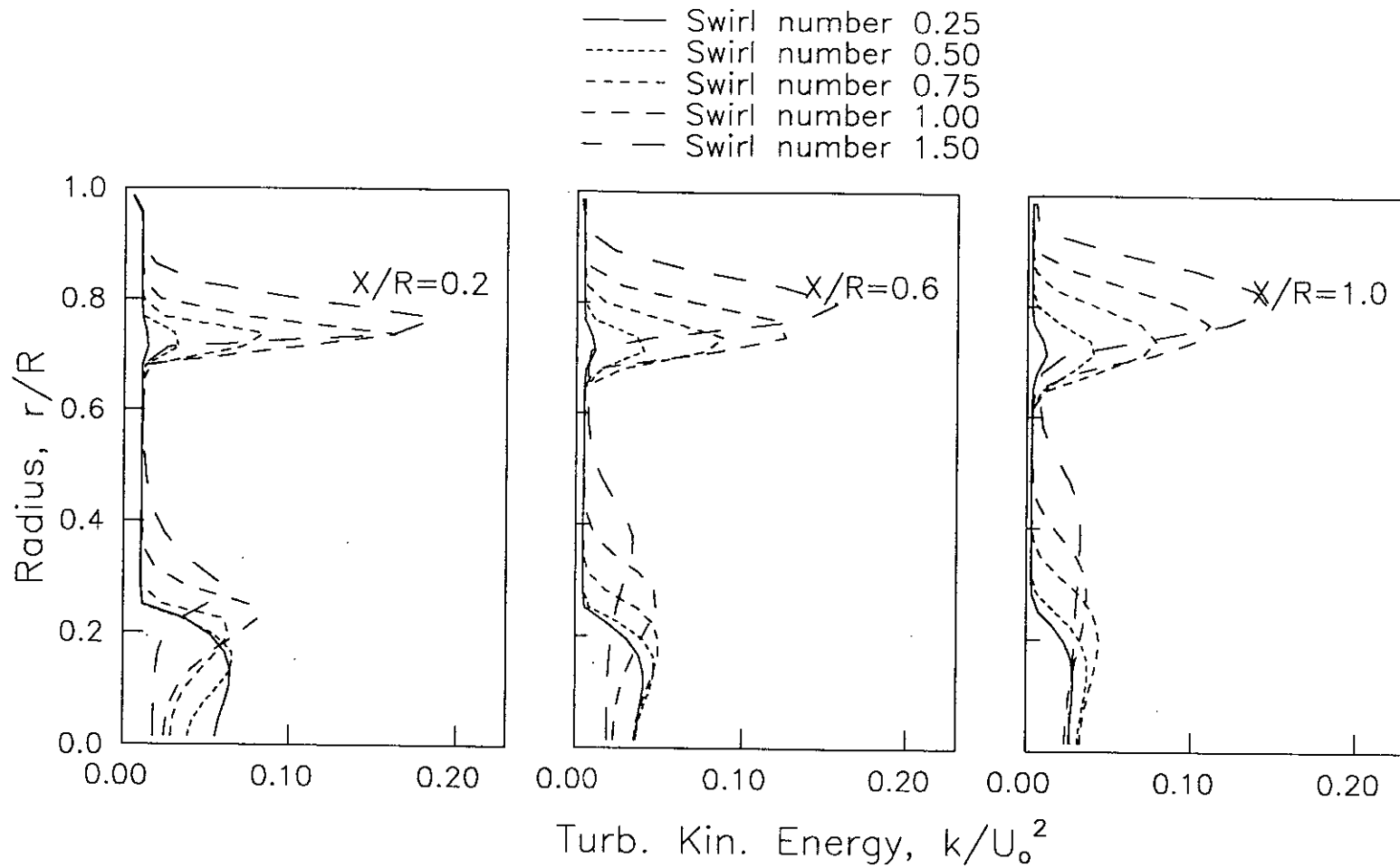


FIG.27a. Comparison of dimensionless turbulence kinetic energy profiles having solid body swirl generator at inlet For Case-I.

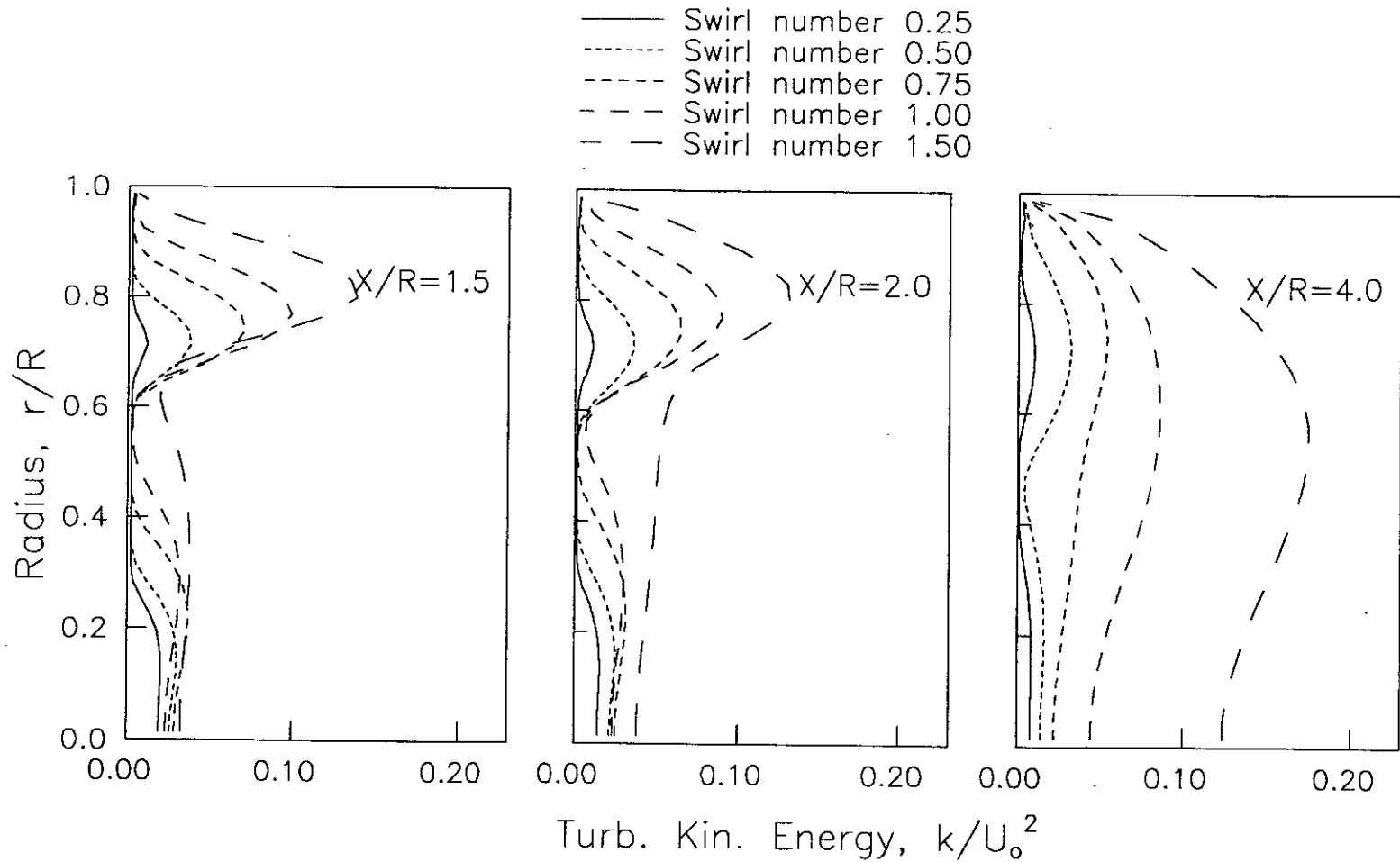


FIG.27b. Comparison of dimensionless turbulence kinetic energy profiles having solid body swirl generator at inlet For Case-I.

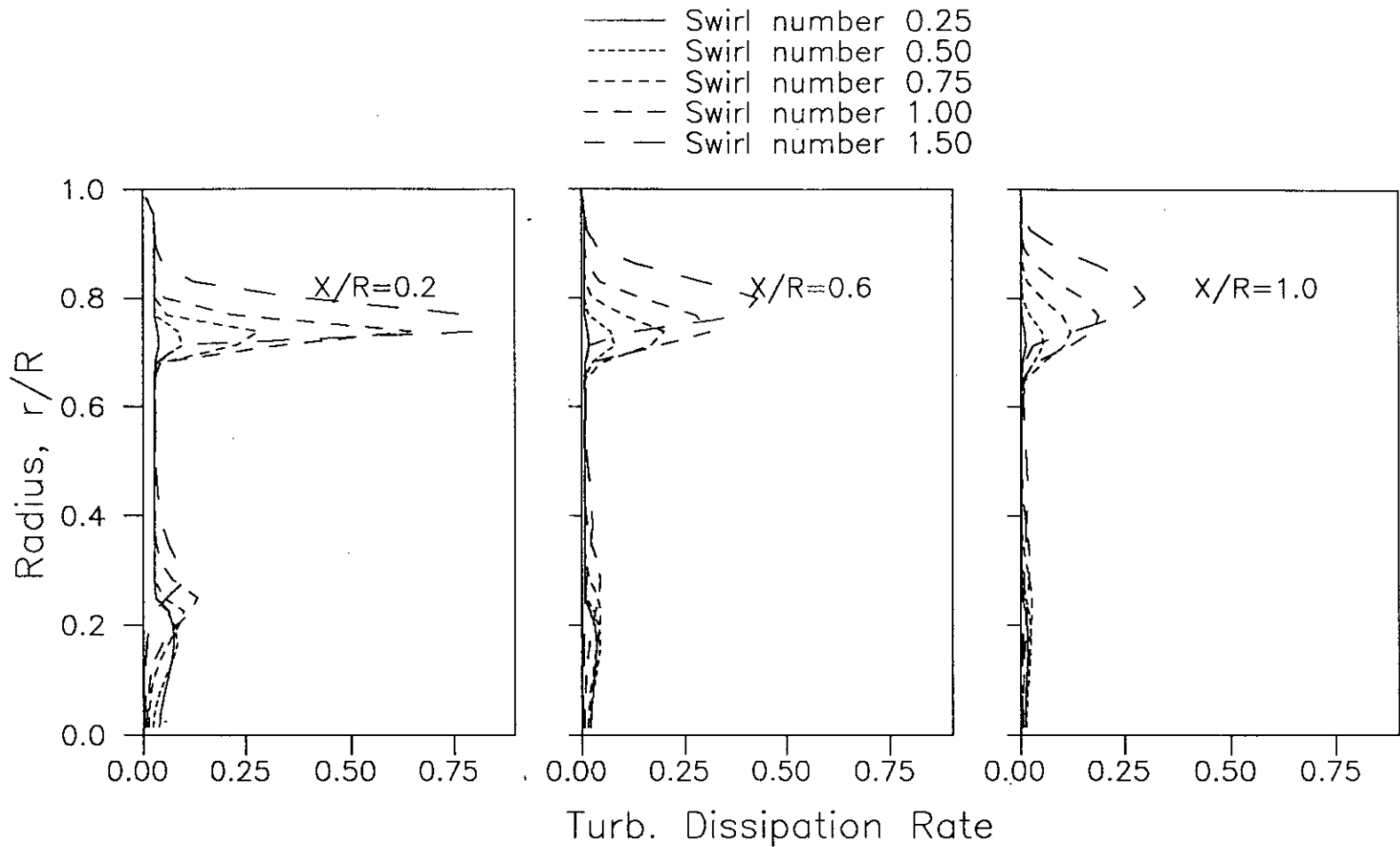


FIG.28a. Comparison of dimensionless turbulence dissipation rate profiles having solid body swirl generator at inlet For Case-I.



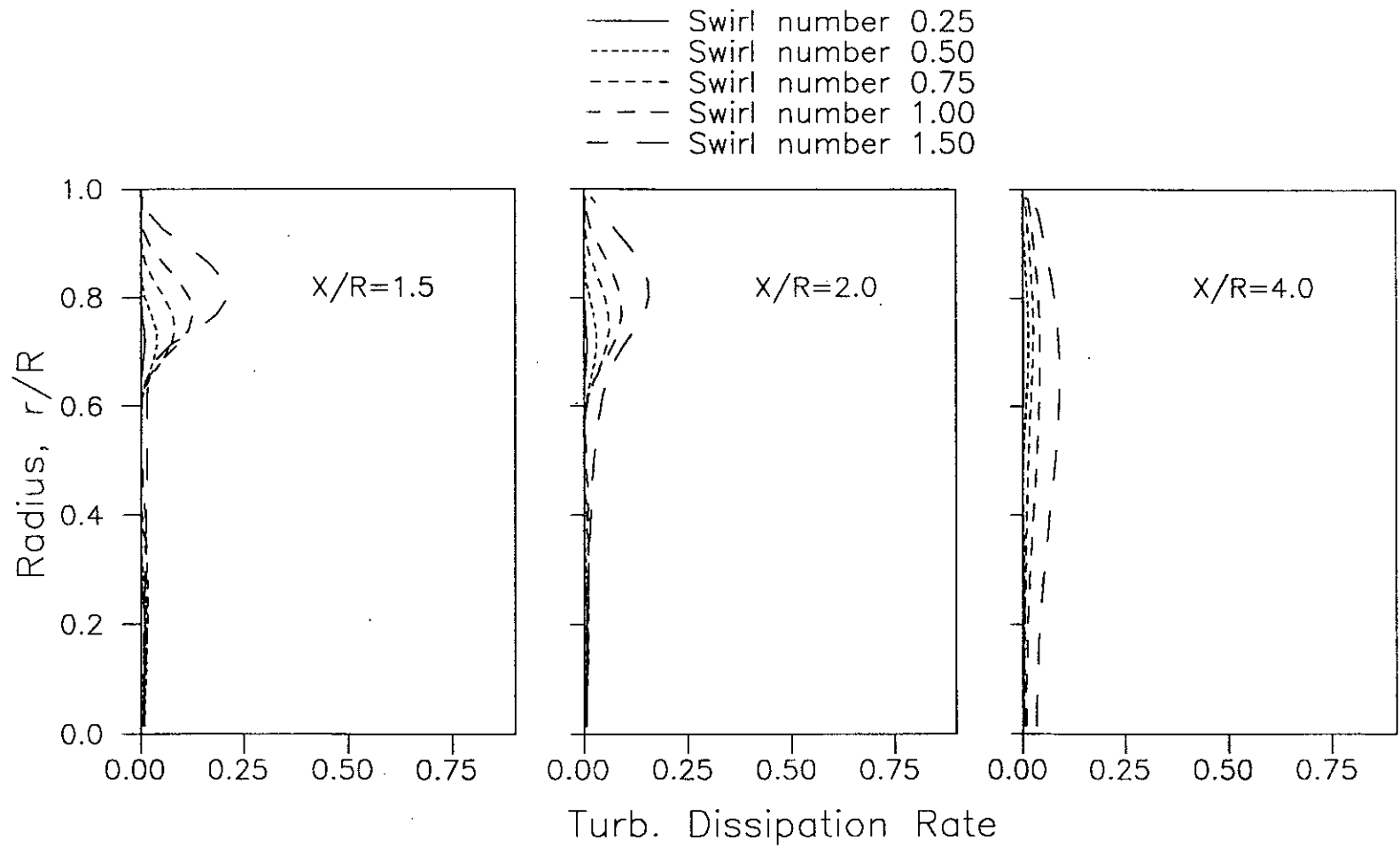


FIG.28b. Comparison of dimensionless turbulence dissipation rate profiles having solid body swirl generator at inlet For Case-I.

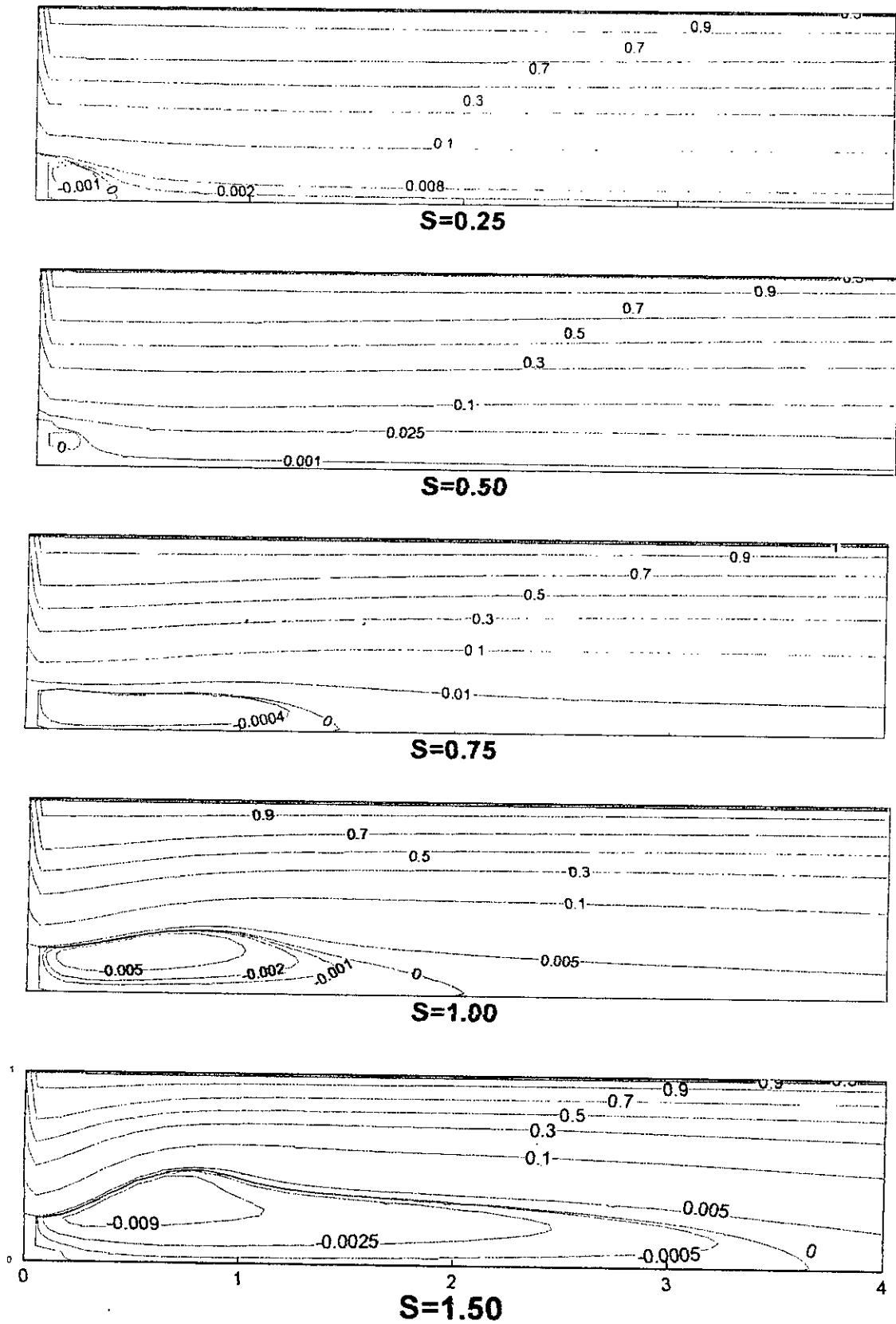
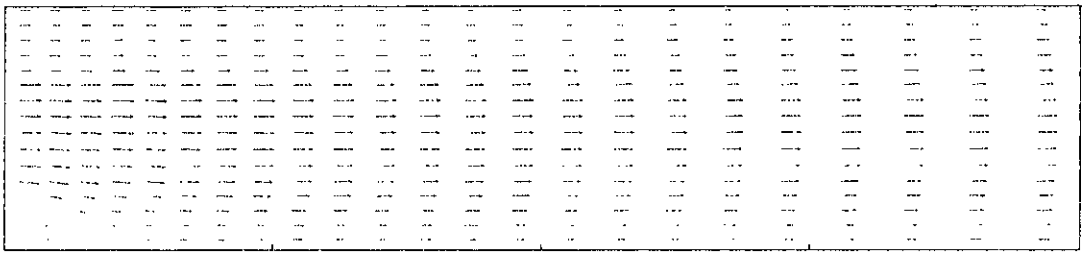
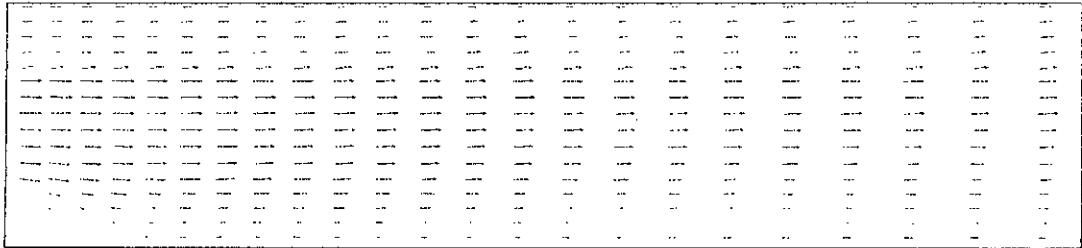


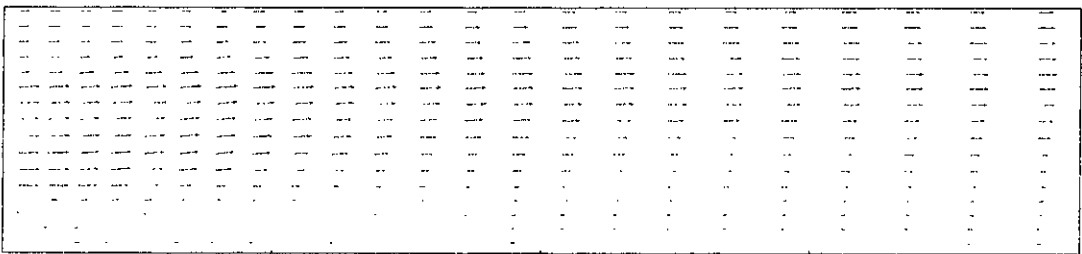
FIG. 29. Streamline plots for solid body rotation swirl generator at inlet for Case-II.



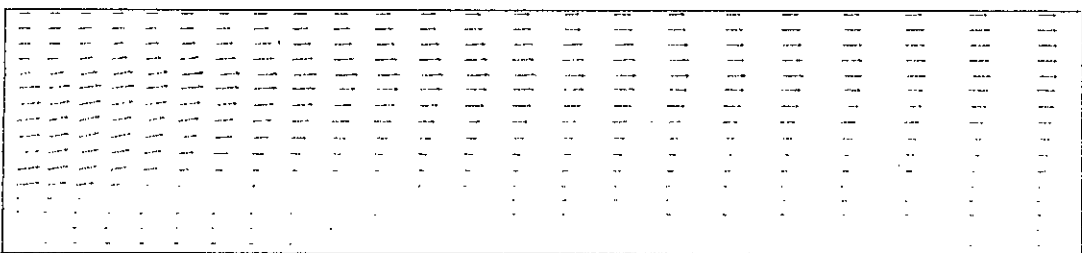
**S=0.25**



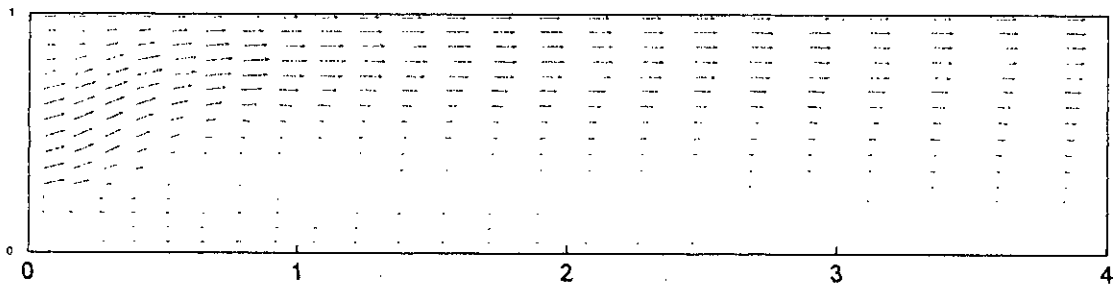
**S=0.50**



**S=0.75**



**S=1.00**



**S=1.50**

FIG.30. Comparison of vector Diagram for combined axial and radial velocities at inlet for solid body swirl generator for Case-II.

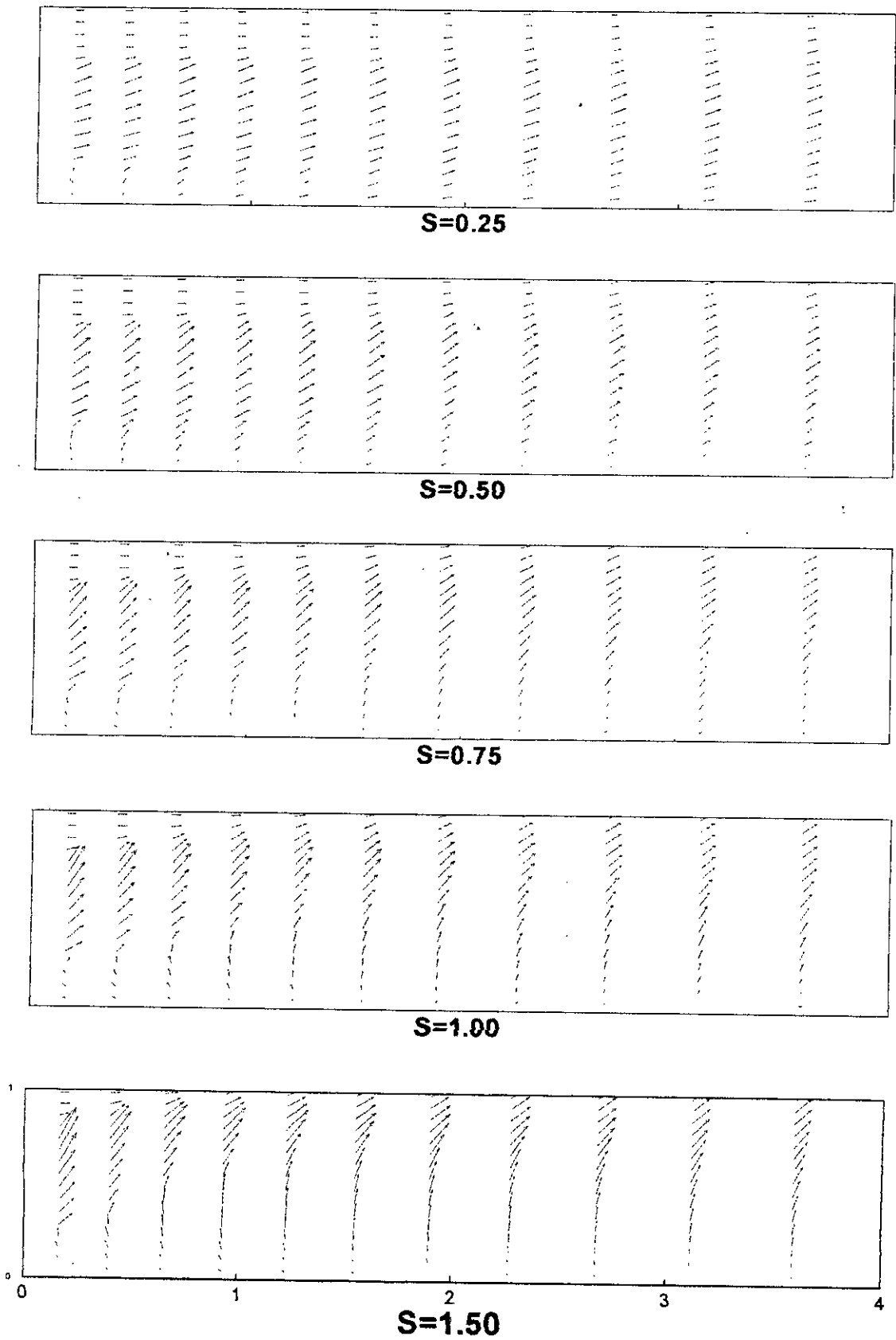


FIG.31. Comparison of vector Diagram for combined axial and tangential velocities at inlet for solid body swirl generator for Case-II.

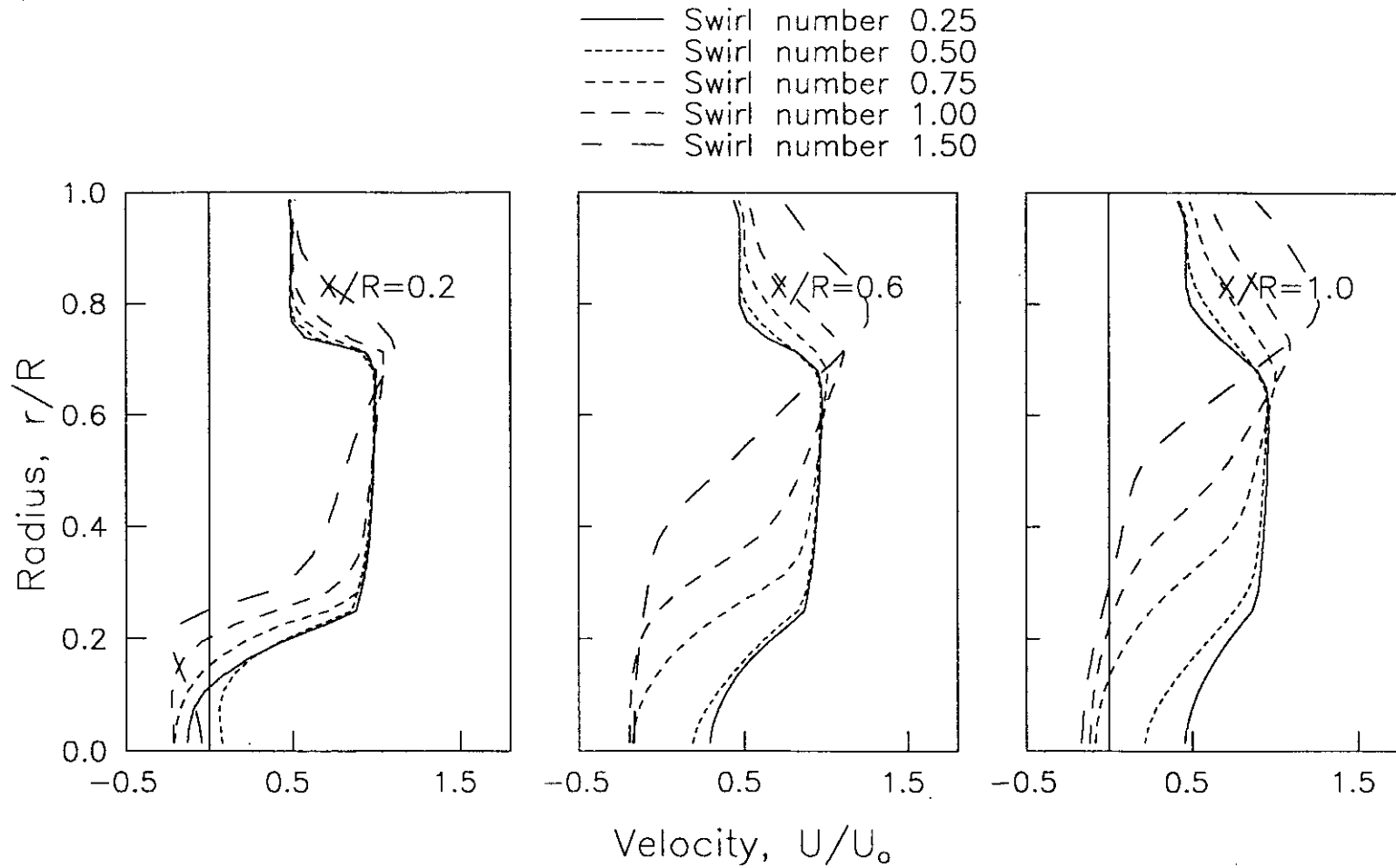


FIG.32a. Comparison of dimensionless mean axial velocity profiles having solid body swirl generator at inlet for Case-II

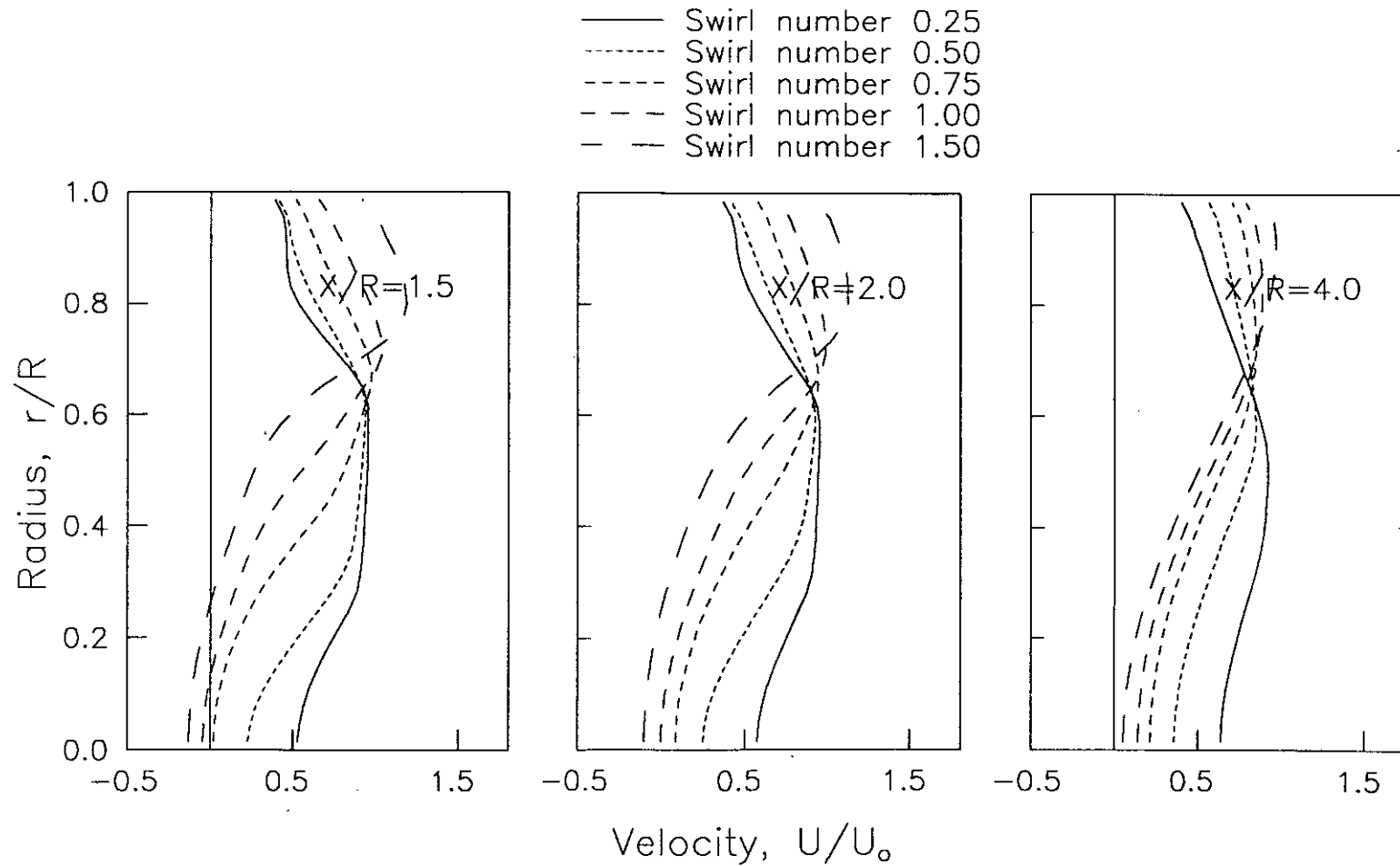


FIG.32b. Comparison of dimensionless mean axial velocity profiles having solid body swirl generator at inlet for Case-II

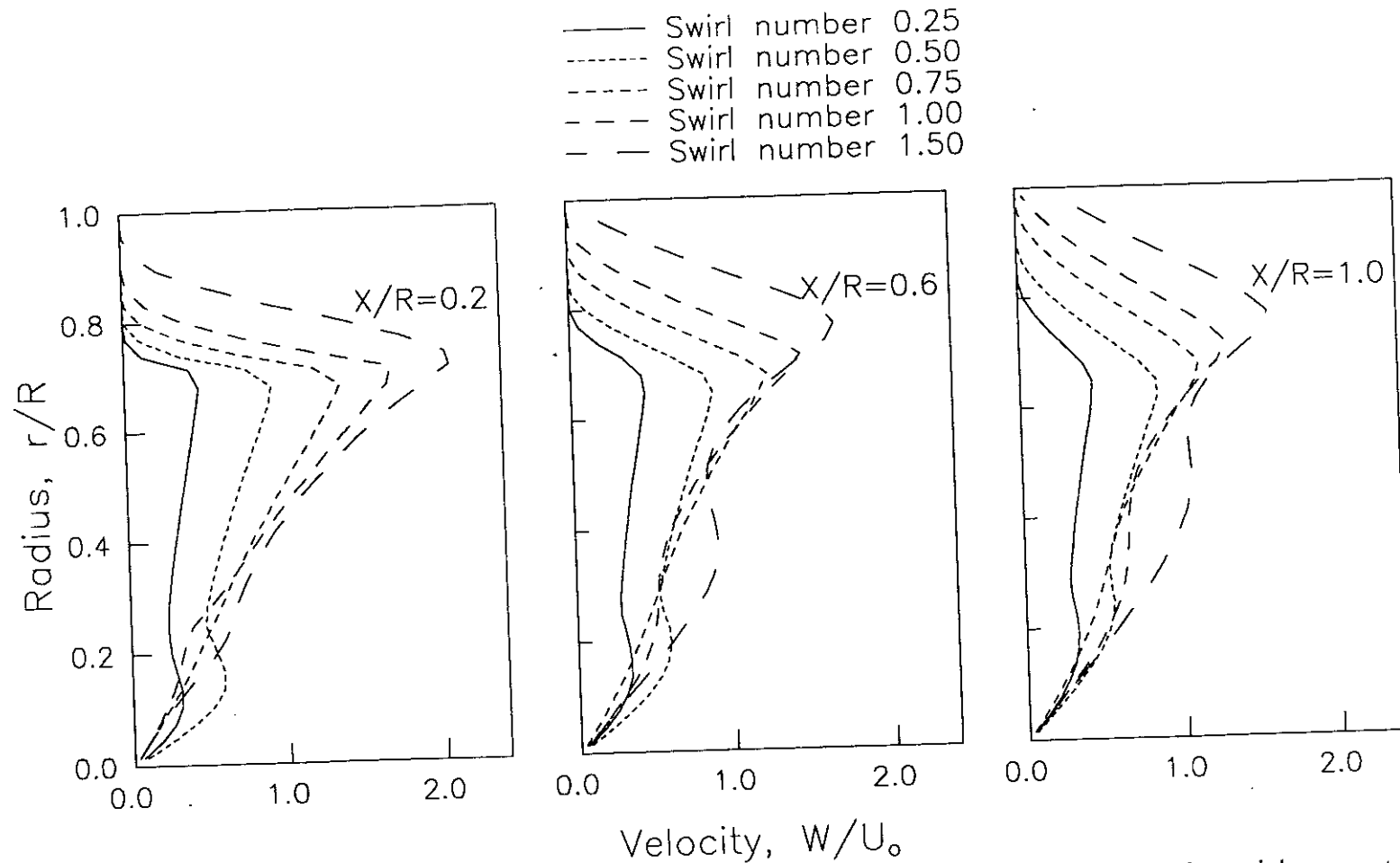


FIG.33a. Comparison of dimensionless mean tangential velocity profiles having solid body swirl generator at inlet for Case-II

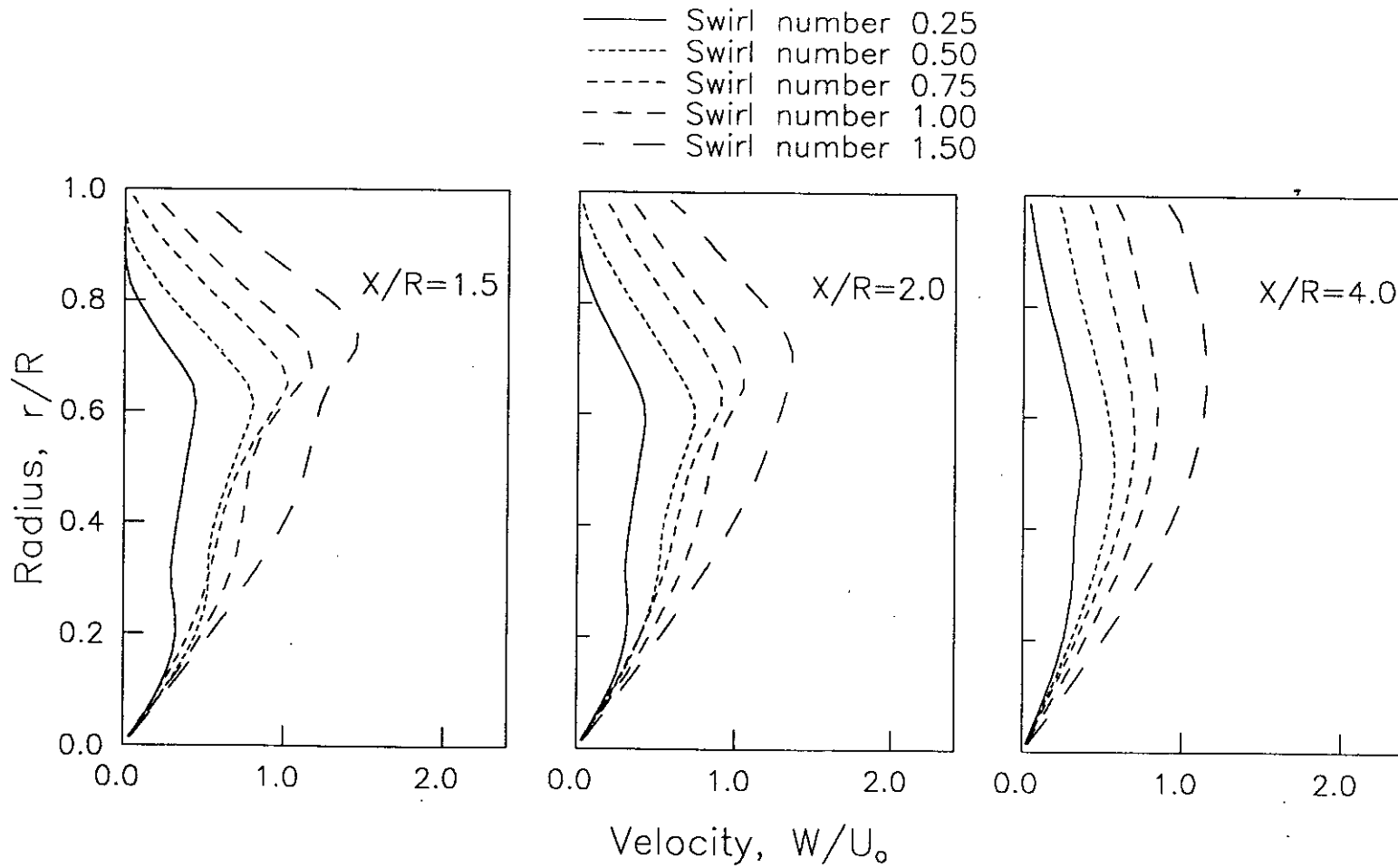


FIG.33b. Comparison of dimensionless mean tangential velocity profiles having solid body swirl generator at inlet for Case-II



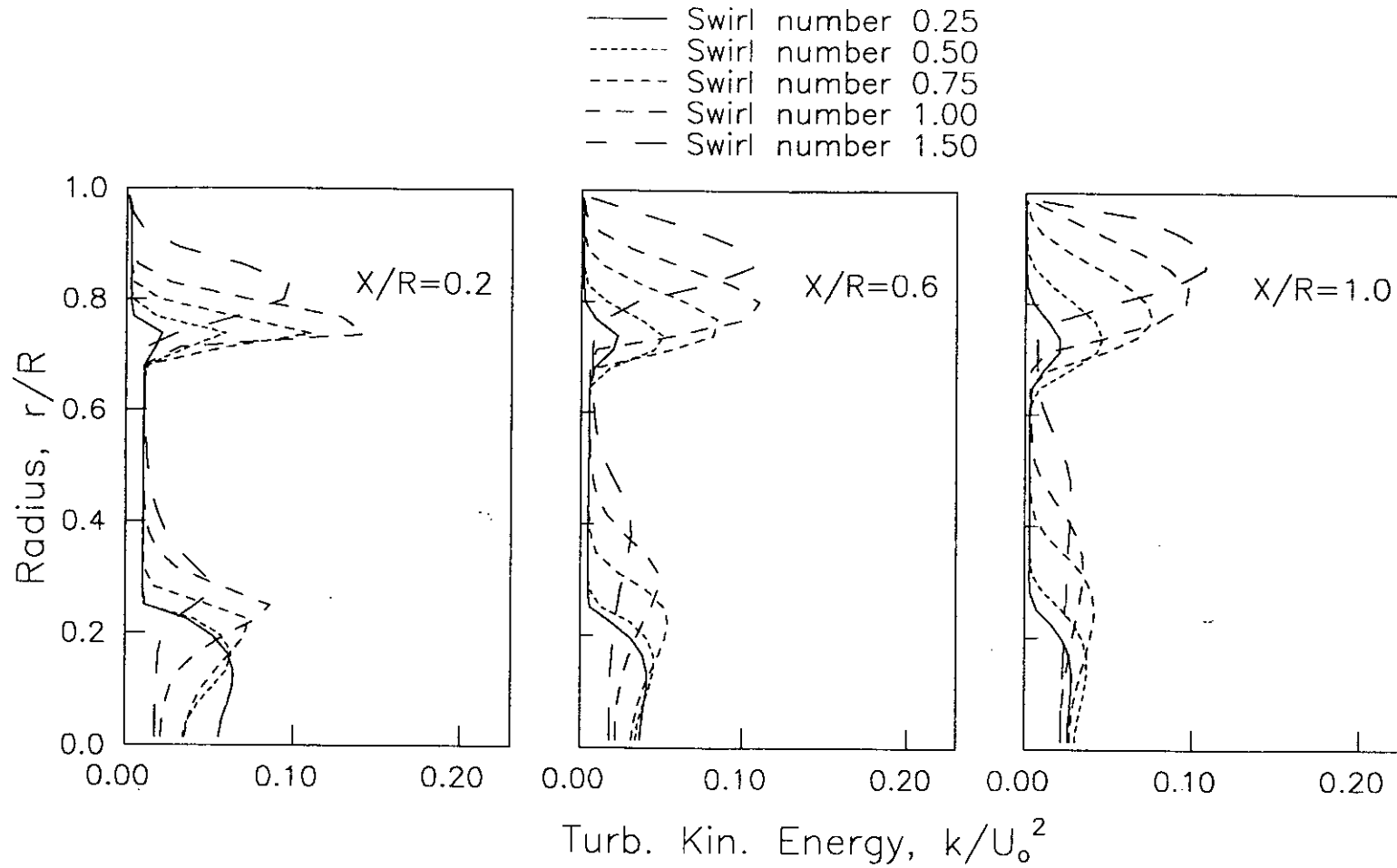


FIG.34a. Comparison of dimensionless turbulence kinetic energy profiles having solid body swirl generator at inlet For Case-II.

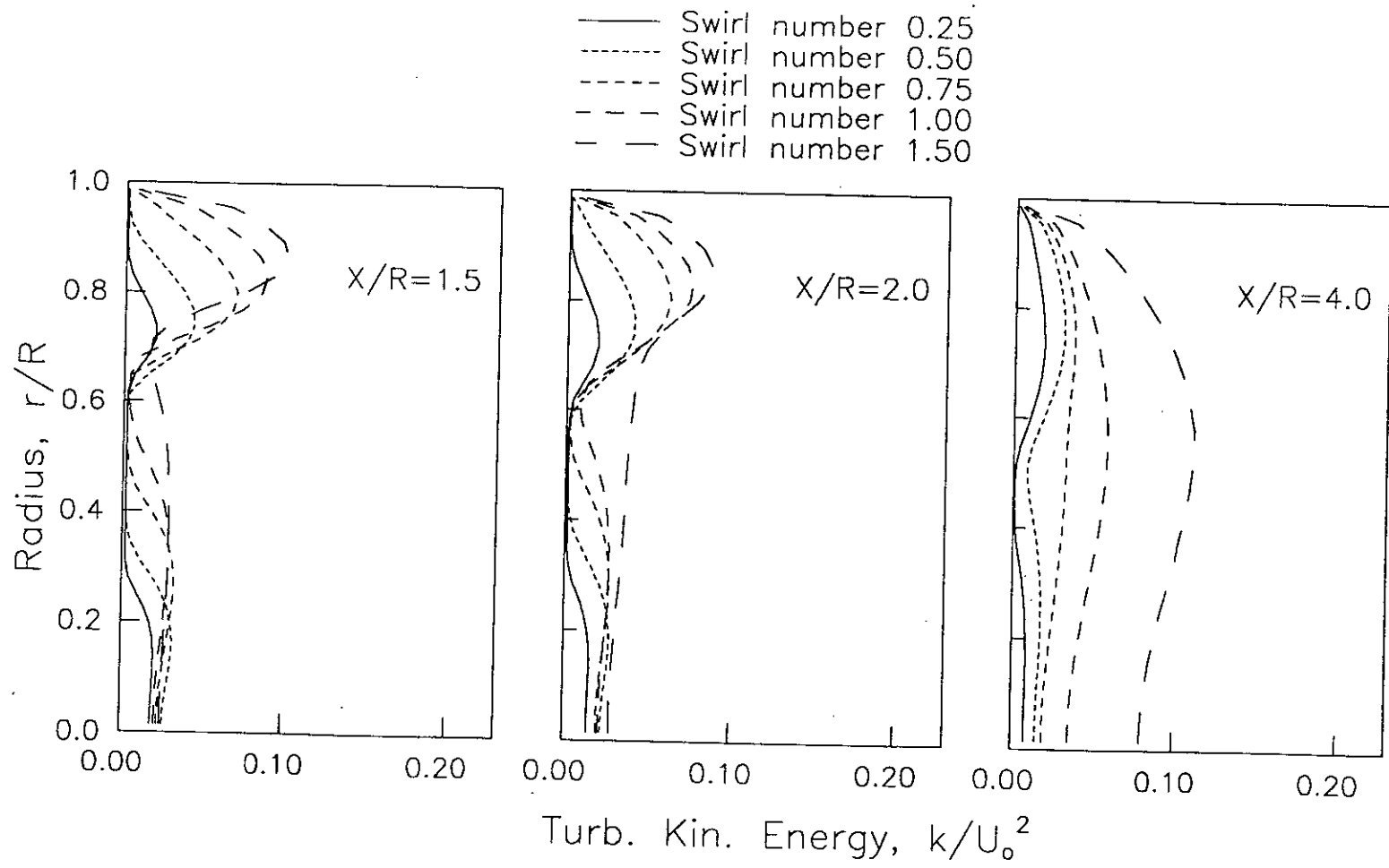


FIG.34b. Comparison of dimensionless turbulence kinetic energy profiles having solid body swirl generator at inlet For Case-II.

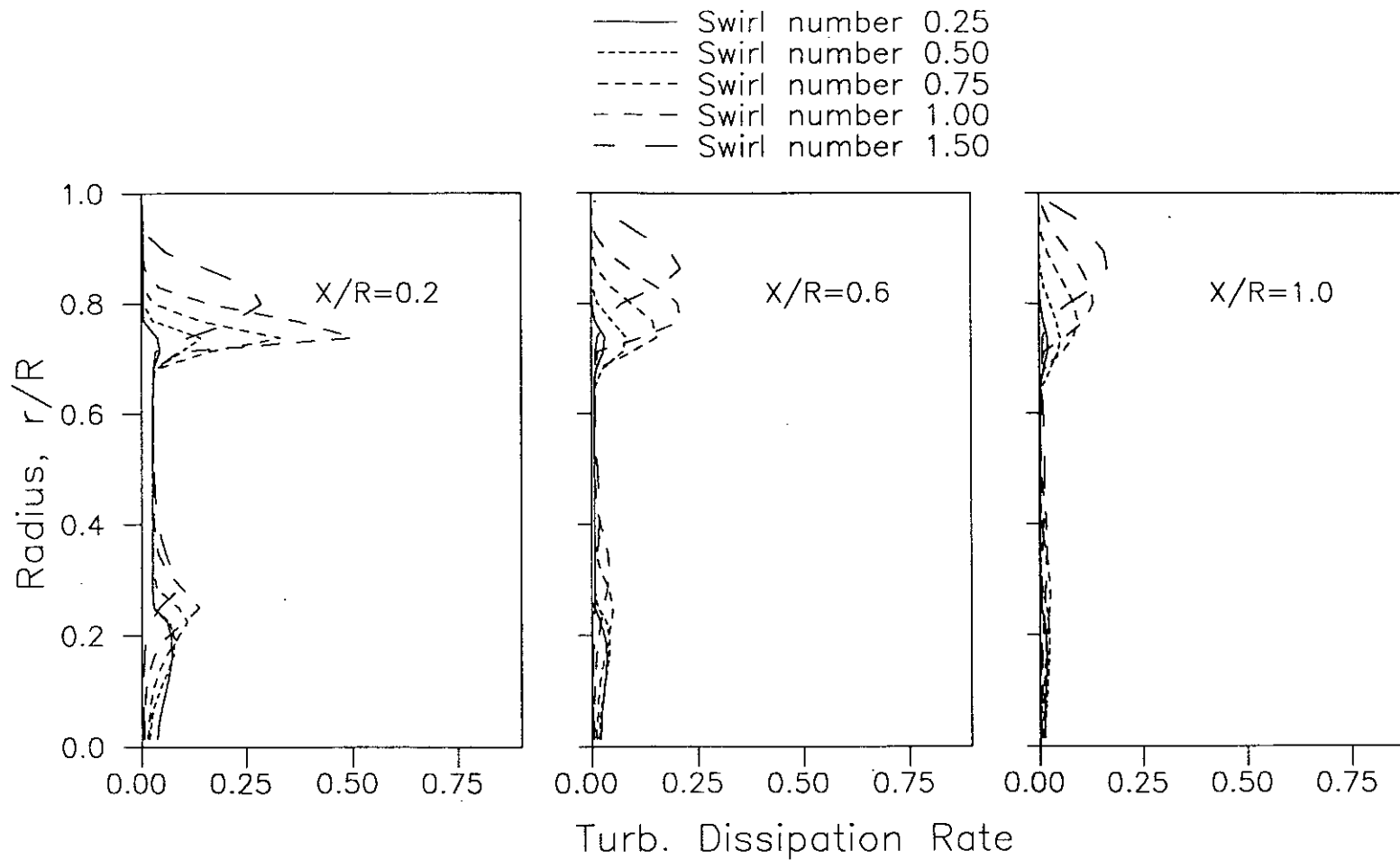


FIG.35a. Comparison of dimensionless turbulence dissipation rate profiles having solid body swirl generator at inlet For Case-II.

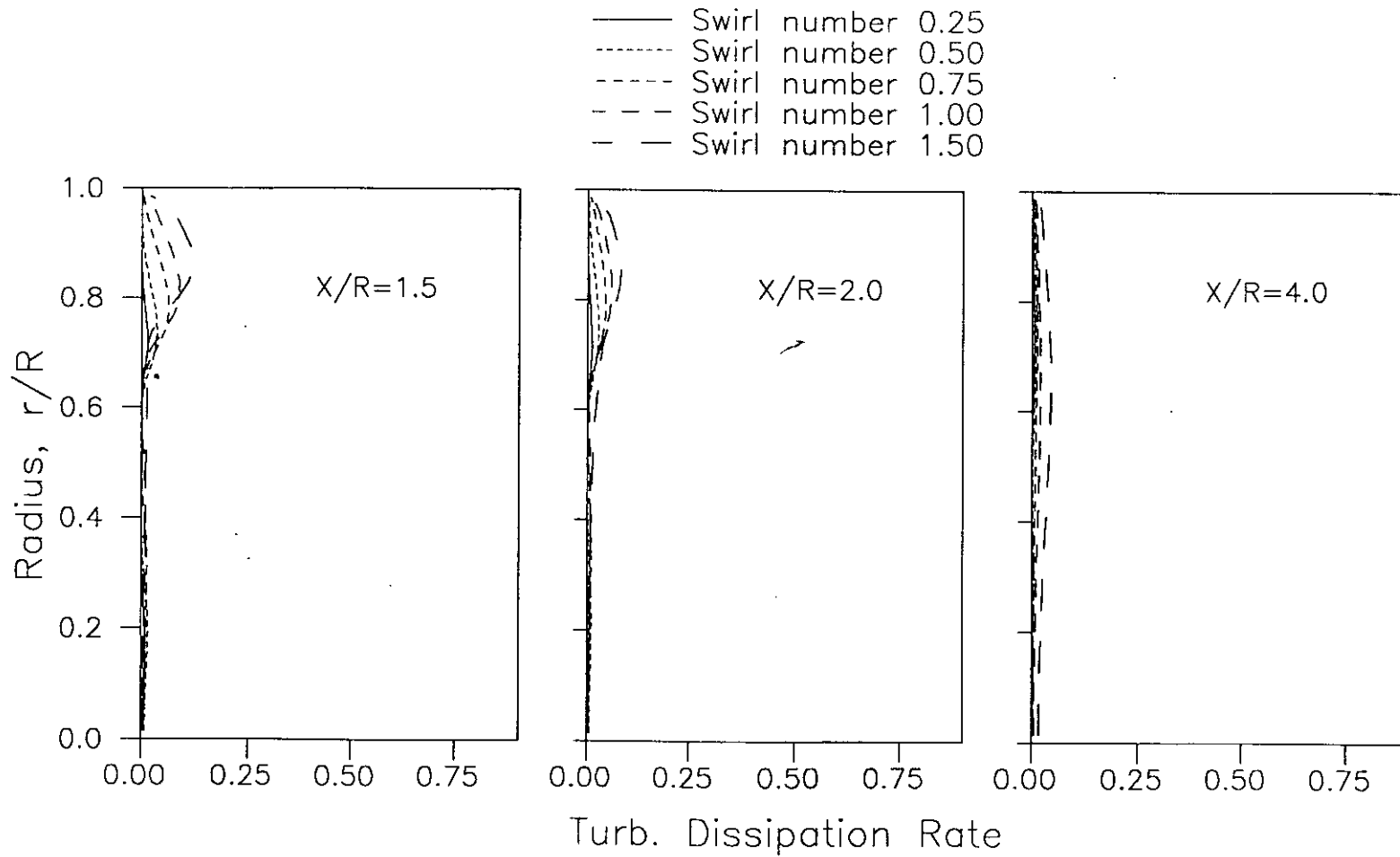
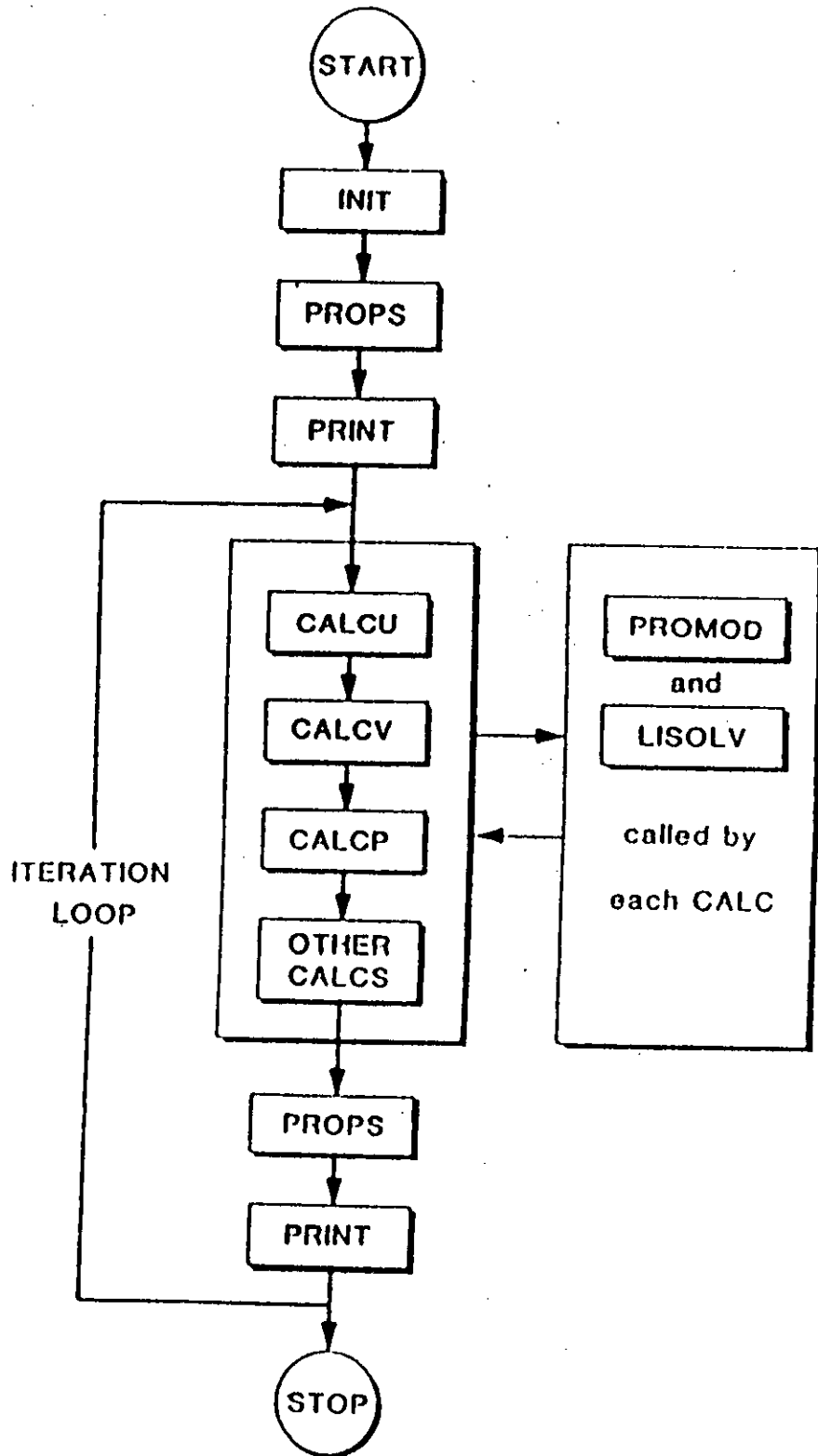


FIG.35b. Comparison of dimensionless turbulence dissipation rate profiles having solid body swirl generator at inlet For Case-II.

# APPENDIX

# COMPUTER PROGRAMME FLOW CHART



A flowchart of the computer program is shown above. Here, the MAIN program unit controls and monitors the entire sequence of calculations: initialization, the iteration loop with calls to update main variables, termination of iteration loop and final output. The INIT subroutine sets values to the numerous geometric quantities concerned with the grid structure. PROPS updates the fluid properties via calculation of turbulent viscosity. Subroutine PRINT prints out an entire variable field according to a standard format. Subroutine CALCU and CALCV calculate coupling coefficients of finite difference equations for axial and radial velocity, calls PROMOD for boundary modifications and LISOLV to update entire field of variables. Subroutine CALCP calculates the coupling coefficients for the pressure correction equation, calls PROMOD for boundary modifications and LISOLV to obtain pressure correction field, and finally corrects the pressure and the axial and radial velocities. The other CALC subroutine updates the variable through calls to PROMOD and LISOLV. Subroutine PROMOD modifies the values of the finite difference equation coefficients. LISOLV updates the entire field of a particular variable, by applying TDMA to all lines in the r- direction sequentially from left to right of the calculation domain.

